Nitrate based High Temperature Nano-Heat-Transfer-Fluids: Formulation & Characterisation

Mathieu Lasfargues

**Submitted in accordance with the requirements for the degree of
Doctor of Philosophy**

**The University of Leeds
Institute of Particle Science & Engineering (IPSE)
School of Process, Environmental and Materials Engineering (SPEME)**

July, 2014

The candidate confirms that the work submitted is his own and that appropriate credit has been given where reference has been made to the work of others.

This copy has been supplied on the understanding that it is copyright material and that no quotation from the thesis may be published without proper acknowledgement.

Acknowledgements

I would like to thank my supervisor, Professor Yulong Ding, for giving me the opportunity to work on such an interesting research project. His constructive criticisms, inputs, encouragement and supervision have guided me toward the production of this thesis.

I would also like to express my thanks to the Abengoa Solar New Technology team particularly Hipolito Lobato Sanchez, Alfonso Rodriguez & Cristina Prieto for their understanding and patience on this research project which has seen some highs and lows.

To Hui Cao, Qiao Geng, Christopher Hodges, Salama Omran, Yongliang Li and Dave Lawlor, thank you for making these four years so interesting. I will miss our discussions on history, politics and sometimes religion which have on some occasion turned into heated debates. In many ways, this has broaden my knowledge and pushed me to be more open-mind.

A big thank you is also in order to Professor Peter J Heggs, for always been helpful when I approach him.

Finally to my Father, Francis, thanks for teaching me the values of resilience and hard-work, to my Mother, Marie-Pierre, thanks for the kind words and encouragement that have carried me through good and bad times, and to my sister, Anne, thanks for putting up with me.

Abstract

This work relates to the development of high temperature heat-transfer-fluid with enhanced specific heat capacity using nano-particle additives. A eutectic mixture of nitrate (60 wt% $NaNO_3$ & 40 wt% KNO_3) was produced through ball-milling and characterised on DSC, TGA, Rheometer. The results obtained showed that the salt mixture melted at 221°C with a heat of fusion of 97 J/g. Onset of melting was seen at 215°C whilst crystallisation started at 219°C, reaching a solid state below 217°C with an enthalpy of 97 J/g. Displaying very little overcooling, the salt showed specific heat capacity of 1.41 J/[°C*g] at 260°C to 1.44 J/[°C*g] at 440°C with viscosity values changing from 4.8 cP at 250°C to 1.7 cP at 450°C for this Newtonian fluid. Thermal decomposition of the salt showed that it was stable up to 550°C. The addition of nano-particles displayed an overall positive effect toward the specific heat capacity enhancing the latter whilst reducing the onset of melting due to increased entropy. The addition of 0.1, 0,5 and 1.0 wt% copper oxide gave the best results with increase of 10.5%, 9,2% and 8,5% in specific heat capacity respectively. SEM analysis of the samples showed that the nano-particles clearly disrupted the crystallisation structure showing a rougher organisation. Rheological tests on 0.1 wt% CuO demonstrated a slight rise in viscosity due to the addition of nano-particles.

The stability of 0.1 wt% CuO was tested in large scale rigs (>1.0 kg) and demonstrated that sedimentation of nano-particles did occur. Different manner of dispersion were tested and revealed that they each affected the

specific heat capacity differently with some causing negative enhancements whilst others were positive.

The method of production did not affect the specific heat capacity values, and current theories point toward the formation of liquid nano-layers as a reason toward this increase.

Table of Contents

List of Tables

List of Figures

Abbreviations

Cp = Specific Heat Capacity

CSP = Concentrated Solar Power

DNI = Direct Normal Irradiance

DSC = Differential Scanning Calorimeter

DSG = Direct Steam Generation

HTF = Heat-Transfer-Fluid

KNO_3 = Potassium Nitrate

$NaNO_3$ = Sodium Nitrate

Solar Salt = Eutectic Binary Mix (60 wt% $NaNO_3$ & 40 wt% KNO_3)

SEGS = Solar Energy Generating Station

SEM = Scanning Electron Microscope/Microscopy

TES = Thermal Energy Storage

TGA = Thermo-gravimetric Analyser

Chapter 1 Introduction

1.1 Background

The increased world-wide demand for energy is promoting the research & development of alternative method of production using renewable sources (Hydropower, wind farms, photo-voltaics, tidal, CSP) rather than non-renewable ones (Oil, coal, gas or nuclear) [1-3]. The latter are been utilized at an increased rate due to the industrial emergence of certain countries (China, Brazil, India…..) as well as the global rise in population [4]. This is directly impacting the environment (acid precipitation, ozone depletion and greenhouse effect) and it is putting pressure on these finite resources which has led over the last few decades to an increase in fuel prices [5]. Out of all the renewable energies available, solar energy has the largest potential (Fig.1), equating about three orders of magnitude that of the world annual energy consumption [6, 7].

This clean and almost endless source of energy can be transformed into electricity via two different routes: photovoltaic & concentrated solar power (CSP). The former technology, which has been widely known and commercially available for many years, makes use of the short wave region of solar energy, whilst the latter only utilizes long wave region of the solar radiation energy.

The research and development of new and more efficient heat transfer fluid (HTF) is one of the areas which could greatly affect the operation of CSP

plants as the HTF serve a dual purpose of transferring and storing thermal energy thereby acting as a buffer for power generation [8-10].
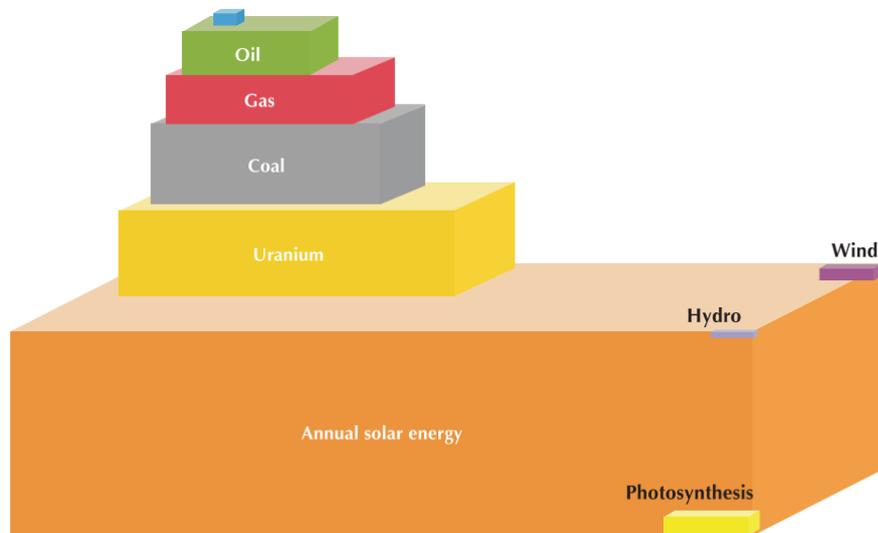
Source: National Petroleum Council, 2007, after Craig, Cunningham and Saigo (republished from IEA, 2008b).

Figure 1: World Energy Consumption per Year by human in blue compared with estimated renewable and non-renewable resources still available. It can be seen that solar energy outweigh all the other resources by a significant margin [11].

Currently employed synthetic oil (VP1-Therminol by Solutia Chemistry), is gradually been replaced with molten salt in CSP plants. Indeed the oil displays a maximum operating temperature of 400°C, high vapour pressure, very expensive production costs as well as been environmentally hazardous. Molten salts on the other hand are cheap, have high operating temperature, low vapour pressure and are far safer to operate.

However it displays high freezing point and low Cp. Whilst the former can be solved through heat tracing or altering the ratio and types of salts used, the latter is more challenging to resolve and will be the basis of this research [12]. Previous published literatures have shown that the specific heat capacity of salt mixtures can be altered through the addition of nano-particles [13-16]. This research will be focused on preparation and screening

of various concentration and types of nano-particles additives to see how they affect the thermo-physical properties of a binary nitrate mixture of salt (60 wt. % $NaNO_3$ / 40 wt. % KNO_3).

1.2 Aims and Objectives

This work aims to try and understand how the addition of nano-particles will affect the thermo-physical properties of a eutectic blend of nitrates. The specific objectives will be as followed:

i. To define the characteristics of a nitrate mixture with the following composition: 60 wt% $NaNO_3$ + 40 wt% KNO_3

ii. To screen a range of nano-particle additives, with concentration varying from 0.1 wt% to 1.5 wt%

iii. To test if any differences in Cp exist between physical mixing and dispersion in water followed by evaporation

iv. To characterise the rheology of the selected additive

v. To analyse how nano-particles interact on salt surface before & after melting of the sample

vi. To investigate how physical dispersion affect the thermal properties of the blend over time.

1.3 Layout of Thesis

This thesis is composed of 8 Chapters. Chapter 2 provides the reader with a summary of the relevant literatures regarding the development of renewable energy and how research within the area of specific heat capacity

enhancement could prove useful both for the renewable energy industries and for academic understanding.

Chapter 3 describes the materials and methods used in this research. This include: preliminary data obtained on the DSC, sample production process for nitrates & carbonates and theories/principles of how the equipments used function.

Chapter 4 provides details on the dimension of the rigs and how the tests were conducted.

Chapter 5 presents the results obtained for the analysis of salts without nano-particles additives.

Chapter 6 looks at the effect of nano-particle additives on the thermo-physical characteristics of solar salt. It also looks into theoretical aspects that might explain the underlying physics behind the experimental data gathered. This chapter will also discuss various variables which might alter the properties of the doped nano-particle salt blends.

Chapter 7 provides the results of the dispersion rig built to investigate the effects of physical dispersion on the Cp of salt mixture with and without additives over time.

Finally Chapter 8 gives a summary of the conclusions obtained in this study and recommendations of future work to be carried out.

Chapter 2 Literature Review

This chapter contains the relevant literature regarding CSP and its implementation into the renewable energy field. Sections 2.1-2.3 describe why solar energy could be a useful alternative to turn to for the production of electricity, what type of systems are available to achieve this and where can this technology be implemented around the world. Sections 2.4-2.7 introduce the reader to the reasons behind the implementation of energy storage systems, the ways in which thermal energy can be stored and the type of HTF commonly used. Sections 2.8 & 2.9 relate to non-ionic and ionic nano-fluid development, how this can be employed for CSP application and the impact it would have on the technology.

2.1 Introduction to the need for Concentrating Solar Power

Today's world is driven by energy which is a vital component of the fabric of our society. Without it, the majority of human activities would cease to function and the whole world would crumble into pieces, if it was to ever become unavailable. Given the fact that, the total annual amount of solar radiation is equal to 2600 times the world annual energy consumption [6], and that this source of energy is potentially endless, it is not complicated to see why solar thermal power stations are of great interest in the development of renewable energy. Furthermore this system of electricity production releases very little if any gases, fumes or dust in the atmosphere and would therefore have little or no environmental impact attached to its operation.

2.2 Concentrating Solar Power Plant

In essence, solar power plants work in the same manner as any conventional power station except that the input of energy is derived from the concentration of solar radiation onto a receiver. This usually occurs in the primary loop system which contains the HTF responsible to collect the thermal energy from the sun and transport it to the heat exchanger which interconnects with the secondary circuit. This thermal energy is then used to heat up water creating high-temperature steam which drives a turbine thereby producing electricity (Fig. 2).

There are currently four different types of CSP technology available: Parabolic Troughs, Linear Fresnel Reflectors, Parabolic Dishes and Solar Towers. The latter four can be sub-divided into either line focusing systems (Parabolic Trough & Linear Fresnel) or point focusing systems (Parabolic Dish & Solar Tower).
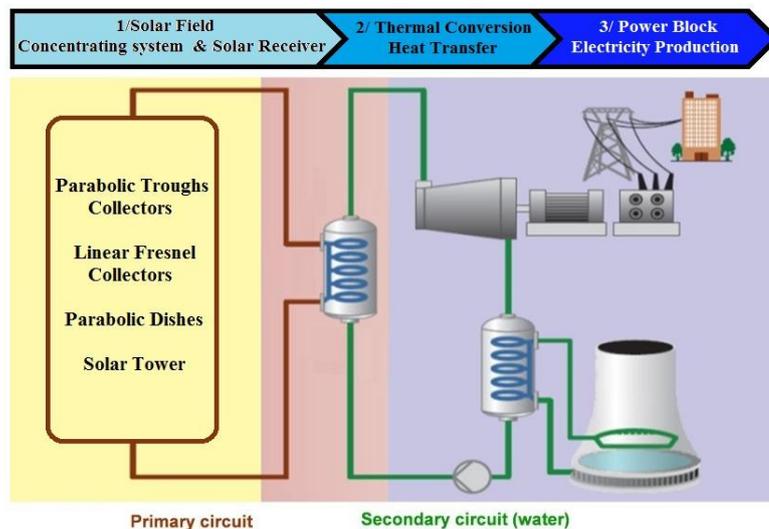
Figure 2: Schematic diagram of CSP [11].

2.2.1 Line Focusing System: Parabolic Trough & Fresnel Collector

Tracking the movement of the sun from East to West, Parabolic trough display arrays of parallel mirrors aligned on a North to South axis. Both the reflector and absorber tube move in tandem such that the incident radiation is always focused onto the linear receiver, maximizing the solar absorption during the day (Fig. 3-a). Following the same motion, Fresnel collectors differ in such a way that series of long, slightly curved or flat, ground-based mirrors pivot and focus the incident sunlight onto a fixed receiver which runs parallel to the reflector (Fig. 3-b).
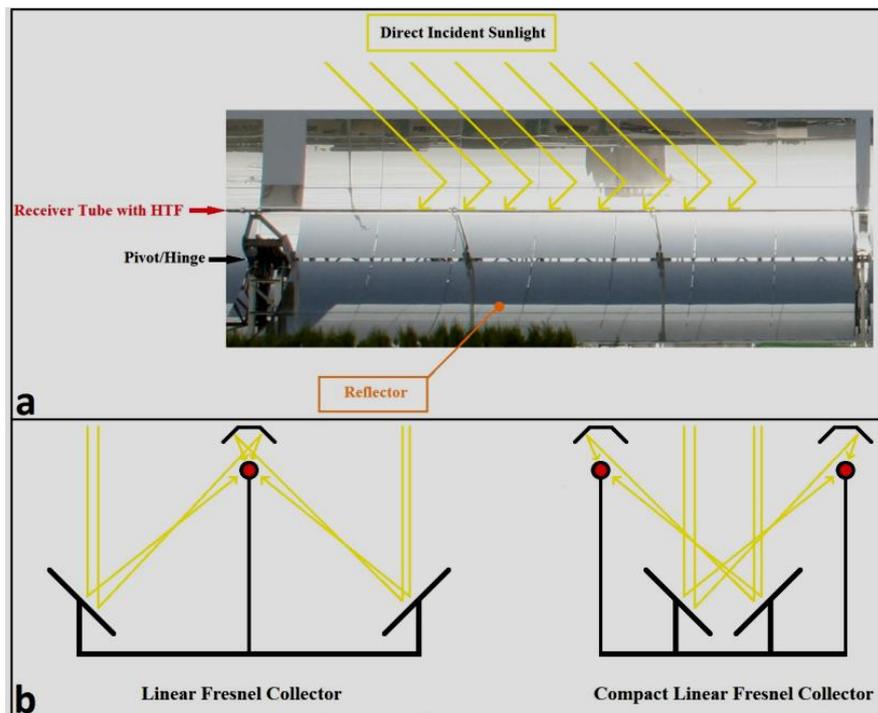
Figure 3: Schematic diagram of: a) Parabolic Trough Collector where the receiver tube and the mirrors move in tandem tracking the sun and b) Fresnel collector display a fixed elevated receiver with a fixed secondary mirror above it to correct the incident light distorted by astigmatism.

The absorber tube used in both technologies is a coated stainless steel cylinder enveloped by an evacuated glass shell, which absorbs the solar short wavelength well, but emits very little of the long-wave radiation, reducing heat loss (Fig. 4).

With the experience accumulated over the last 30 years from the Californian Trough plants (SEGS I-IX), this CSP technology utilizing synthetic oil as HTF is regarded as the most mature of all the current system available [17-19]. Furthermore the overall geometry of trough allows the collection of a larger proportion of solar radiation as Fresnel collector surfer from greater morning and afternoon cosine loss because of the fixed receiver which lower solar-to-electricity conversion efficiency.
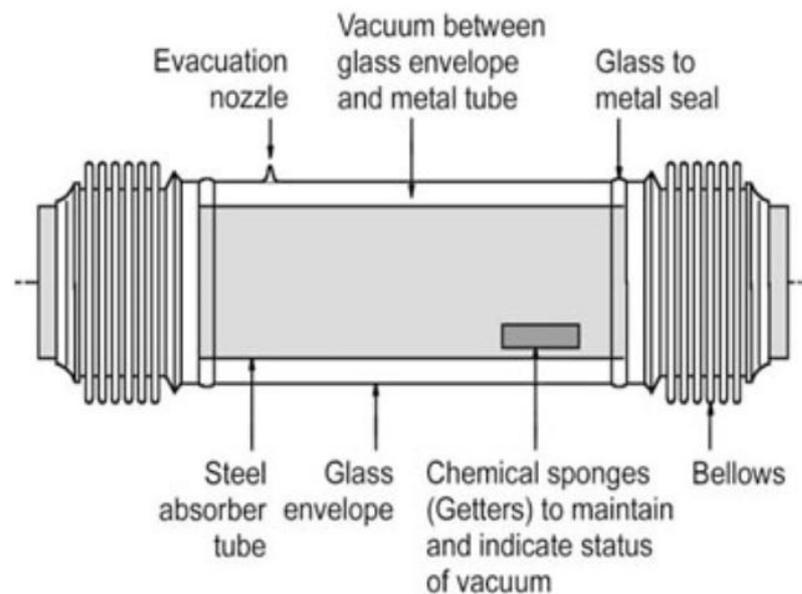
Figure 4: Schematic diagram of the absorber tube used in CSP applications. The HTF flows through steel absorber tube [20].

The development of compact Linear Fresnel Collector (Fig 3-b), where the compact arrangement of mirrors allows individual row to reflect light on two

different linear receivers, could maximise solar collection and minimize shading and blocking during the operation [21, 22]. Fresnel Collector development requires cheaper mirrors, less steel and concrete. Furthermore it displays smaller wind load, greater surface mirror per receptors and a simpler construction (avoiding the need for rotary joints). However, it still lacks the accumulated experience of operation and maintenance gathered by Trough collector over the past few decades. This is reflected by the sheer number of plants built with 83 world-wide projects, most of which are commercially producing electricity whilst Fresnel has only 10 working projects. Leaders in these technologies are Spain and USA.

2.2.2 Point Focusing System: Parabolic Dish & Solar Tower

Using a two axis tracking system (Elevation & Azimuth), this technology focuses the sun's radiation onto the receiver with maximal accuracy such that temperature up to 1000°C can be attained [23, 24]. In parabolic dish (Fig. 5-b), the sun's rays are concentrated toward the power conversion unit (Stirling, micro or Brayton turbine) located at the centre of the parabola. Built around a light structured frame, this system could potentially operate in remote location. With research focusing its effort on Stirling engine for power generation due to its higher solar-to-electricity conversion efficiency, this technology can offer long-term low maintenance operation [8, 17, 25, 26]. However more research is needed to cut the cost of operation and maintenance as well as ensure a high level of system reliability.

Solar tower (Fig. 5-a) uses hundreds if not thousands of reflectors called heliostats which are independently controlled to concentrate the sun's rays

onto the central receiver located at the top of the tower [27]. This system is highly flexible in term of design and a variety of heliostats, receivers and transfer fluids can be used [28]. Currently employed for commercial production of electricity, power plants are cost efficient and profitable if built to provide power above 50 MW [29]. Concept of multi-tower solar array are currently been tested in Australia (Lake Cargelligo) [30].
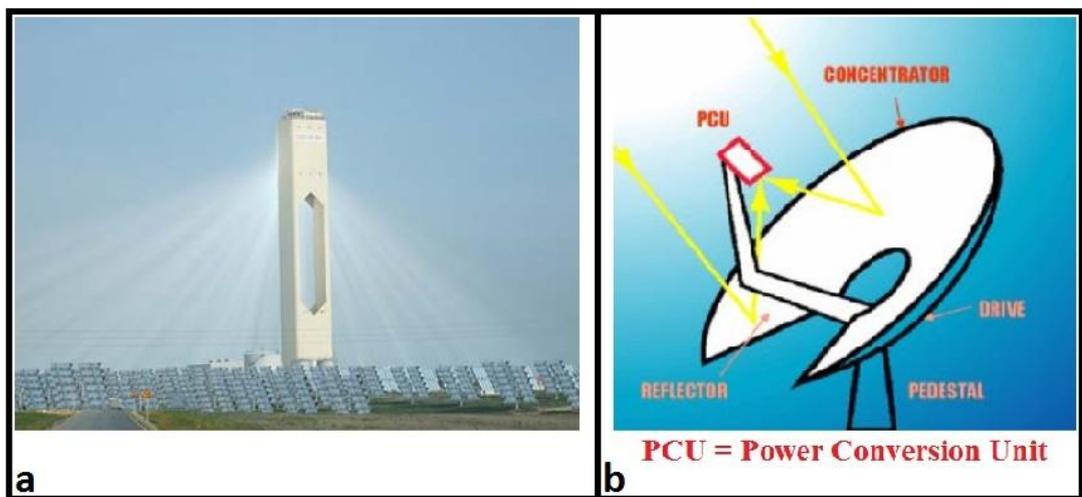
Figure 5: a) Picture of 11 MW PS10 solar tower located in Sanlucar la Mayor, Seville, Spain [18], b) Schematic diagram of Parabolic Dish [25].

2.3 Solar Resources: Direct Normal Irradiance

CSP technologies rely entirely on DNI which is the fuel of a CSP plant. The latter is the amount of solar radiation hitting a perpendicular surface tracking the sun's movement (pyrheliometer system) and is calculated in kilo-Watts hour per meter square per year ($kWh/m^2/year$). Thus the design of a CSP plant is primarily based on this component which can provide an approximation of the electrical output. It therefore comes as no surprise that a CSP plant need to be built in a location where the minimum DNI is around 1900 to 2100 $kWh/m^2/year$ as any values below that would result in no net production due constant heat loss through the solar field [8, 17, 18, 27]. Although it might, in the future, be plausible to build CSP plants in lower DNI, the current estimates (1900 to 2100 $kWh/m^2/year$) are used as standard throughout the literature. This implies that a cloudy or foggy day will result in a direct component of zero leading to no electricity production. Hence the area where a CSP is built is important.
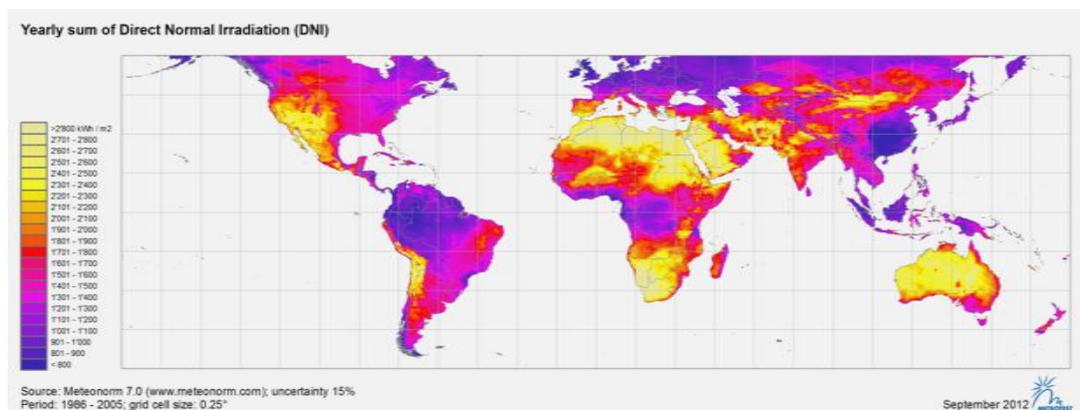
Figure 6: Direct Normal Irradiance of the World. The lighter shade of yellow indicates a higher yearly DNI.

The obtention of a good DNI and reliable clear sky throughout the year lay in regions between the 15° to 40° in latitude north and south of the equator where conditions are arid or semi-arid. Regions such as Northern & Southern Africa, Middle East, Western part of U.S.A, Australia and parts of South America (Chile, Peru, and Mexico) display the best solar resources for the installation of such technologies.

The definition of DNI can be based on satellite or ground data. Whilst model and commercial tools can calculate with good accuracy the solar fraction available at ground level taking into account atmospheric flux, ground base measurement provide more accurate data and does not rely on extrapolation. However, the gathering of such data relies on high quality measurement devices which most countries within the solar belt lack. Furthermore if industries or government do have available dataset on a particular region, they are generally unwilling to share this information with others [31, 32].

In most cases, the developments of CSP imply extended simulation of the performance of the plant over several years. In an ideal world, the developer would have access to dataset of the ground DNI spanning 5 to 10 years which would give a real estimate of the solar flux from one year to the next. This would allow to plan and fine tune the simulation accordingly. Furthermore the localization of the plants needs to be based around the end users, to meet local energy demands, and has to be optimized and scaled consequently. This implies developing thermal storage to cope with the intermittent nature of solar resources.

2.4 Thermal Energy Storage System & CSP Plants

CSP technologies display the advantages of using a form of energy, thermal, which can easily be coupled to a storage system. The latter is crucial to the future development and adoption of CSP plants as a general electricity provider, to solve the intermittency problems encountered by solar fluctuation. Indeed the DNI varies in intensity during the day and is inexistent at night.
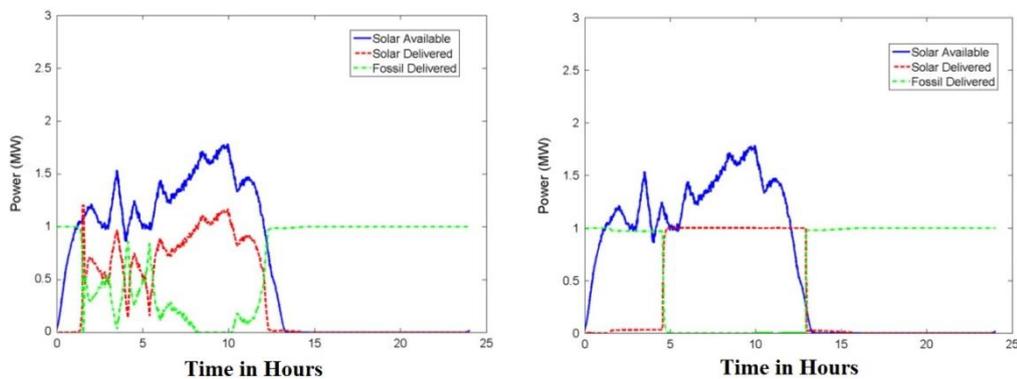
Figure 7: Left graph shows simulation without thermal storage during cloudy weather, causing fluctuation in solar output (Red) and the use of fossil fuel back-up system (Green) to buffer this. Right graph displays the simulation of the same CSP system but with TES system. No fluctuation in power output (Red) is seen which imply that the backup system not utilized (Green) [33].

This means that production of electricity is only possible during the days if no energy storage is available. Integrating thermal storage to CSP would allow the surplus of thermal energy produced to be stored and used during periods with little or no DNI to drive the generator thereby producing electricity. Such technology would display several advantageous roles:

- Buffering – Any drop in DNI due to transient weather encountered during the day could be buffered by the storage system. Furthermore the consumer might not necessarily use the energy when it is produced. This mismatch between production and utilization would be solved as the system would store excess energy produced and release it when needed.

- System Stability – Providing enough storage is added to the system, then the fluctuation in weather would have less impact on the turbine allowing it to run at a stable rate thereby increasing the overall system efficiency and probably lifetime of the plant [34].

- Increased Annual Capacity Factor – The addition of energy storage increase the daily usage of the plant as electricity production can be extended into the night, whereby the TES system takes charge of production. Therefore the annual capacity factor is increased.

2.5   Types of Thermal Energy Storage Systems

In essence TES systems are very basic and comprise of storage medium, insulated container and heat exchangers. The design and use of such technology is in part dictated by the type of material used as well as the way in which thermal storage is combined to the CSP plants.

Different storage systems will exploit different form of heat storage;

- Steam Accumulator (Sensible Heat)

Uses direct steam generation and stores excess production as liquid (4.21 J/[g*K]) at high pressure and temperature in an insulated stainless steel tanks. When energy is need, steam is released for electricity generation. This system is currently providing Planta Solar 10 with 1 hour of storage (50 bars & 285°C) for the 11 MW solar tower located in Seville, Spain. Alternative research into solving sliding pressure during discharge is been look at using latent or sensible heat storage material inserted inside the tank. However this technology is unlikely to be economically viable on large scale.
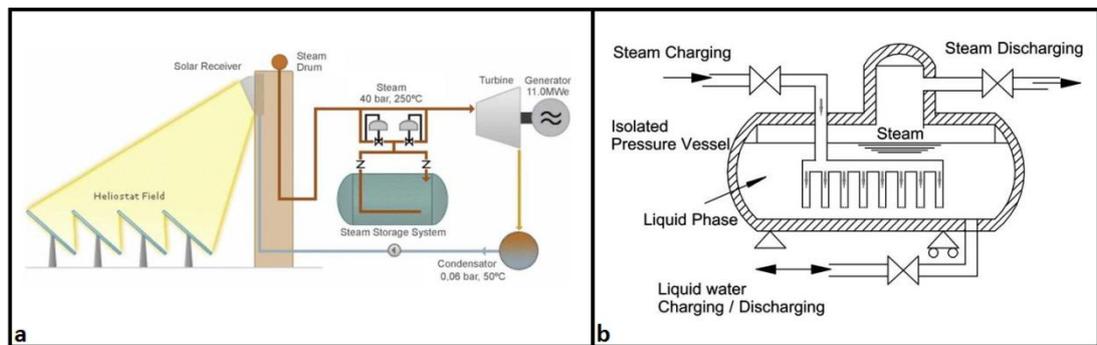
Figure 8: a) Schematic representation of the DSG system [35], b) TES integration in CSP system (Left) [34].

- Thermocline Systems (Sensible Heat)

The principle of this system lies in the creation of a thermal gradient on the vertical axis that separate the hot fluid located at the top from the cold fluid at the bottom. A filler material, which is usually low cost, is used to help maintain this gradient by reducing natural convection within the liquid and provides buoyancy as well. Charging occurs by withdrawing cold fluid from the bottom to be heated up through the heat exchanger and returned at the top of the tanks. The reverse process occurs for discharging [36].
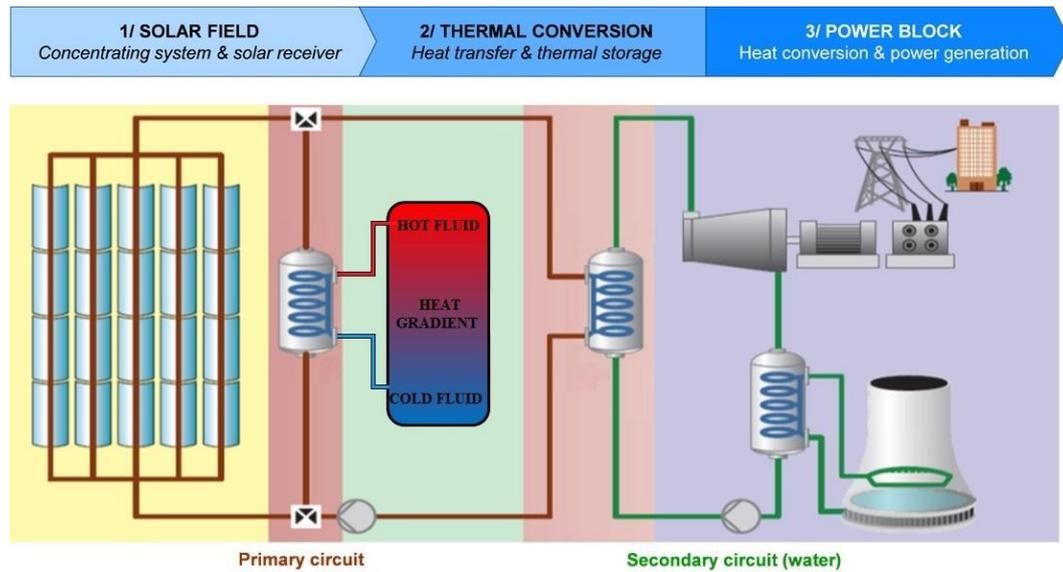
Figure 9: Schematic representation of a thermocline storage system integrated to a CSP Plant [11].

- Passive Systems (Sensible and/or Latent Heat)

In this design, the HTF flows through the storage medium charging the latter. Discharging of the system is achieved through the reversal of flow. Such designs rely heavily on a good thermal diffusivity to shorten the charging and discharging processes. With different existing systems of storage available, the design of the unit (shape and size) will dictate the flow of heat. Indeed the fluid can flow either around the storage system or directly through it. Encapsulation of PCM as well as castable ceramic and high temperature concrete are some of the few materials been looked into as mean of thermal storage [37-41]. The use of sensible heat would require large volume storage due to its low specific heat capacity, which is unlikely to be economically viable although some studies showed that the concept was feasible.
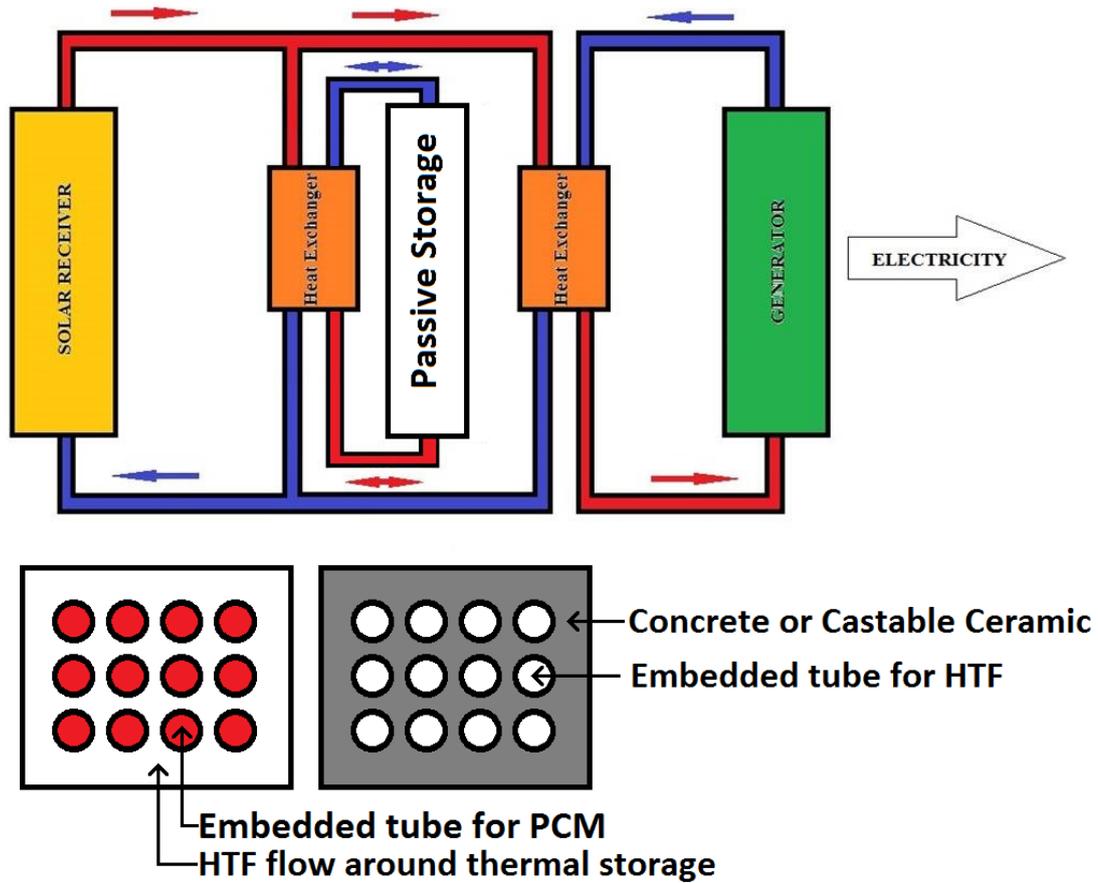
Figure 10: Top schematic shows the integration of passive storage to CSP system whilst bottom diagrams display the way in which the materials are put together to create the storage unit.

- Two Tanks Systems (Sensible Heat)

The addition of this system depend on the original design of the plant and can either be incorporated directly or indirectly:

➢ Direct TES implies that the material flowing and absorbing the solar radiation is the same as that used in the storage systems. Hence, the liquid used act as both HTF and TES through the circumvolution of pipes (Fig. 11).

> Indirect TES is where the HTF and TES fluids are different (Fig. 12). Thus the two loops are interconnected with an extra heat exchanger.
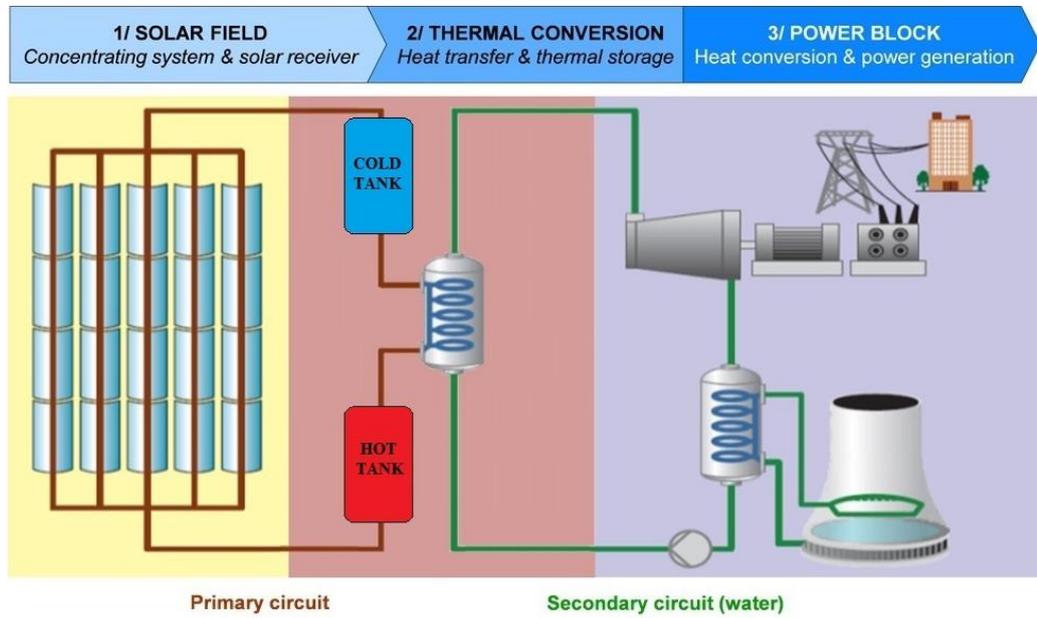
Figure 11: Direct thermal storage [11].
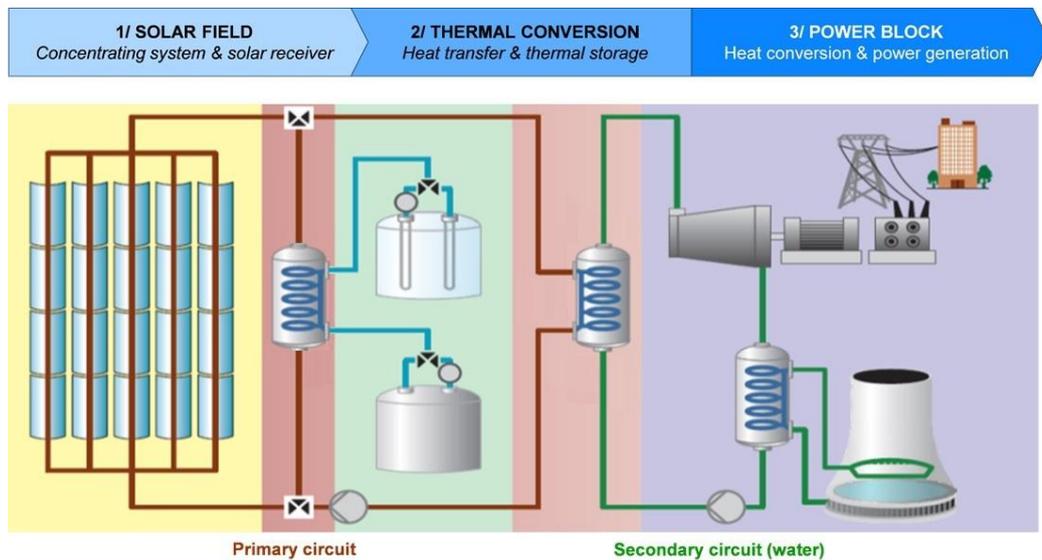
Figure 12: Schematic diagram of indirect TES [11].

This technology uses two well insulated tanks containing a liquid media whose purpose is to store sensible energy. These systems utilize a hot and cold tank with varied temperatures depending on the fluid used.

Large-scale commercial usage of this technology was introduced in SEGS I plant and provided 3 hours of storage via the use of Caloria oil [34, 42]. In this particular example, the 'hot' tank was used to store the synthetic oil at 307°C after it had been heated by the solar trough field. When energy was needed, the hot oil would be discharged to generate electricity and returned to the cold tank (240°C). Been a direct system, it had the advantage of using only one heat exchanger for power generation, reducing cost, compared to the two been used in indirect storage (one to link the storage system to the HTF and the other for power generation).

However the most utilize technology is the indirect storage system with a eutectic mixture of nitrate salts commonly referred to as Solar Salt (60 wt% $NaNO_3$ and 40 wt% KNO_3, Tm: ≈220°C). Using 28500 tonnes of salts for a total storage capacity of 1010 MWh (Tank size: 14 meters high and 36 meters diameter), this system provides 7.5 to 8 hours of thermal storage capacity.

As of today, this storage system is the most mature in the world with 18 parabolic trough CSP plants using this technology (Archimede [Italy], Andasol 1-2-3 [Spain], Arcosol 50 [Spain], Aste 1A-1B [Spain], Astexol II [Spain], Extresol 1-2-3 [Spain], La Africana [Spain], La Dehesa & La Florida [Spain], Manchasol-2 [Spain], Termesol 50 [Spain], Termesol 1 & 2 [Spain], SEGS 1 but damaged in 1999 and not replaced [USA]).

2.6   Form of Thermal Energy Storage

The design of TES is also dependent on the form of heat used to store energy which can be: Thermo-Chemical, Latent or Sensible.

Regardless of the form or type of storage employed in the process, there is a list of desired requirements which the medium should fulfil in order to be of use [42]:

- High Heat capacity (J/g) which is also referred to as energy density. The higher it is, the smaller the containment unit will be for a given amount of storage required.

- High Thermal conductivity (W/[m²*K]) is extremely important in the rate of charging and discharging of the unit. This is partly controlled through the design of the heat exchanger.

- Chemical stability implies that the material would not degrade or react over long period of time.

- Mechanical stability of the material refers to its ability to withstand stress as it is cycled through the heat exchanger at various pressures.

- Thermal stability is the operating range of the material. Using a higher working temperature would result in a higher efficiency.

- Compatibility with container material i.e. Corrosive nature of the medium.

- Low environmental impact.

- Low cost.

2.6.1 Thermo-Chemical Heat Storage

Based on a reversible reaction, heat is absorbed by an endothermic reaction leading to the splitting of a compound into separate substances. When heat needs to be produced, the separate compounds are recombined to give an exothermic reaction releasing heat.

Potentially, this type of system has the greatest energy density of all of them as well as the highest efficiency. Indeed breaking molecular bonds require a large amount of energy, and lead to the production of two separate substances which can be stored indefinitely and recombined whenever needed. However the chemical reaction needs to be well understood and controlled to prevent the creation of undesirable by-products which might damage the system. Furthermore, if the reaction leads to the production of gas, then storage become a problem because the units need to be reinforced and the gas would have to be pumped and therefore pressurized. This is the case of closed loop system using methane reforming or ammonia where the products need to be store separately and safely [43, 44].

Methane Reforming:

$$CH_4 + CO_2 + Heat\ (350°C - 1000°C)\ \rightarrow 2H_2 + 2CO$$

$$2H_2 + 2CO\ \rightarrow CH_4 + CO_2 + Heat$$

Ammonia:

$$2NH_3 + Heat\ (400°C - 500°C) \rightarrow\ N_2 + 3H_2$$

$$N_2 + 3H_2\ \rightarrow Heat + 2NH_3$$
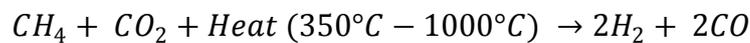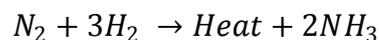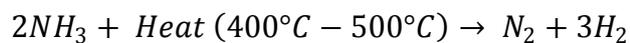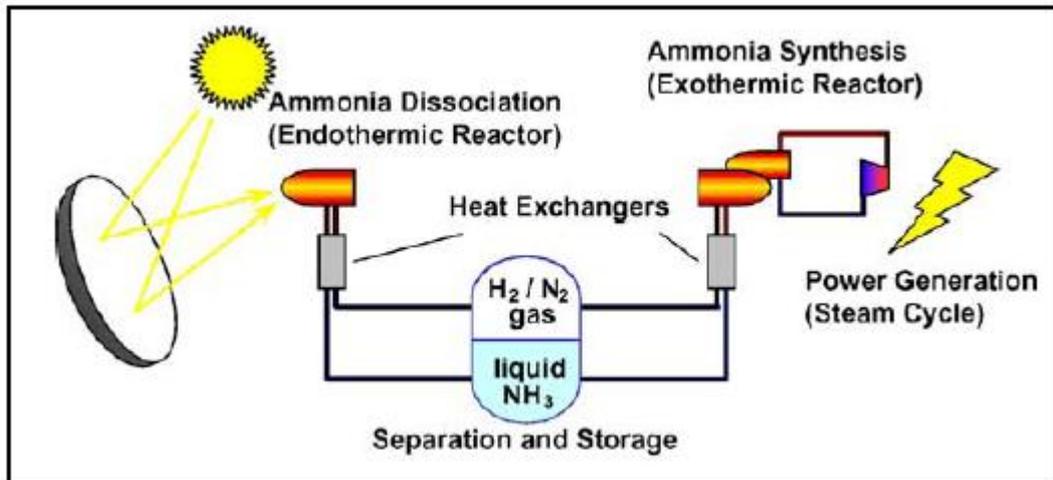
Figure 13: Ammonia dissociation used as energy storage[44].

The decomposition of metal oxide, hydroxides and carbonates are other examples which could also be used [45, 46].

$$MnO_2 \leftrightarrow 0.5\, Mn_2O_3 + \ 0.25\ O_2\ (530°C)$$

$$Ca(OH)_2 + \ Heat \leftrightarrow CaO + \ H_2O\ (505°C)$$

$$CaCO_3 \leftrightarrow CaO + CO_2(896°C)$$
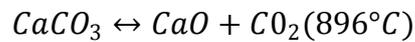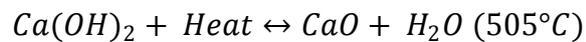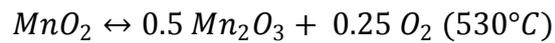
This type of energy storage technology is a potential candidate for TES but its implementation is still largely held back by pressurization problems if gases are used, which would be costly to put into place and maintain over-time. Furthermore the use of these endothermic reversible reactions needs to be suited to the system it is utilized on. Challenges are still encountered in the cycling stability and reversibility of the reaction as well as potential limitation in heat transfer which can be altered depending on the system design.

2.6.2 Latent Heat Storage

In latent heat storage, the absorption and release of heat allow the transition of a material from one phase to the other. The possible transitions are solid-solid, solid-liquid, solid-gas, liquid-gas and vice-versa. The solid-solid transition occurs through a structural change as the material accumulates energy, its molecular arrangement is altered (Amorphous to Crystalline or the opposite). However this sort of transition only requires a small amount of energy leading to a limited thermal storage capacity. Solid-gas and liquid-gas transitions occur with a large volume change and therefore containment issues often arise as a gas phase is involved, which needs to be pressurized. Solid-liquid transition is therefore the most favourable option as this does not suffer from large volume change upon transition and displays a good energy storage capacity.

Latent heat can be defined by the following equation:

$$Q = m \times L$$

Q = amount of energy released or absorbed in Joules

m = mass in kg

L = specific latent heat in kJ/kg

Also called phase change material (PCM) or referred to as 'Heat-of-Fusion storage' by A. Abhat 1983, the selection of phase change materials is based on desirable thermodynamic, kinetic and chemical properties such as [47];

- Appropriate phase-transition temperature, which varies with respect to the system that it is applied to

- High specific thermal capacity (kJ/[kg*K]), heat of fusion (J/g), and density (kg/m^3) to lower the size of the thermal unit

- High thermal conductivity (W/[m*K]) is important in charging and discharging phases

- Small volume changes upon phase transformation and low pressure would reduce containment problem of the PCM

- Congruent melting, so that phase separation does not take place

- Chemical stability of the melts over a long period of time, which implies reliable changes between solid and liquid form over many cycles

- Low or inexistent super-cooling which hinder the heat extraction

- Compatibility with the construction material i.e. not corrosive

- They should be resistant to oxidation

- Non-toxic

- Available and Cheap.

Any chosen PCMs need to fulfil as many of the above conditions as possible. Because every PCM will have some weaknesses, the development of a specific storage system will be required, to lower the impact of the latter, and increase the efficiency of the system [48]. Furthermore the release of thermal energy from a phase change material is usually an isothermal step which would offer better quality of heat providing it occurs at a temperature suited to the system. On CSP application this type of storage technology would provide a way of maintaining heat production during hours when no direct sunlight is available. This would allow electricity generation and would prevent freezing of the HTF within the pipes especially if molten salt are utilized. Of all the PCMs available, only molten salts seem to fit best toward

the development of such technology. Indeed the availability of a range of salt whether eutectic or not provides a broad temperature range for its implementation spanning from low temperature with HITEC (Tm: ≈142°C) (7 wt% $NaNO_3$ – 53 wt% KNO_3 – 40 wt% $NaNO_2$) to high temperature with single salt such as Barium Sulphate (Tm: ≈1680°C) [12]. Been relatively cheap to purchase and with a low impact on the environment, molten salts are the best candidates for latent thermal energy storage applications displaying high latent heat of fusion and relatively low toxicity. However their corrosive nature and low thermal conductivity need to be addressed through research. This has been looked at using methods such as encapsulation (Micro or Macro), impregnation and/or dispersion. Whilst the former method is more easily applicable to low temperature PCM (<100°C) [49-53], impregnation [54, 55] and dispersion [56, 57] can be applied to high temperature.

(a) Storage process

(b) restitution process
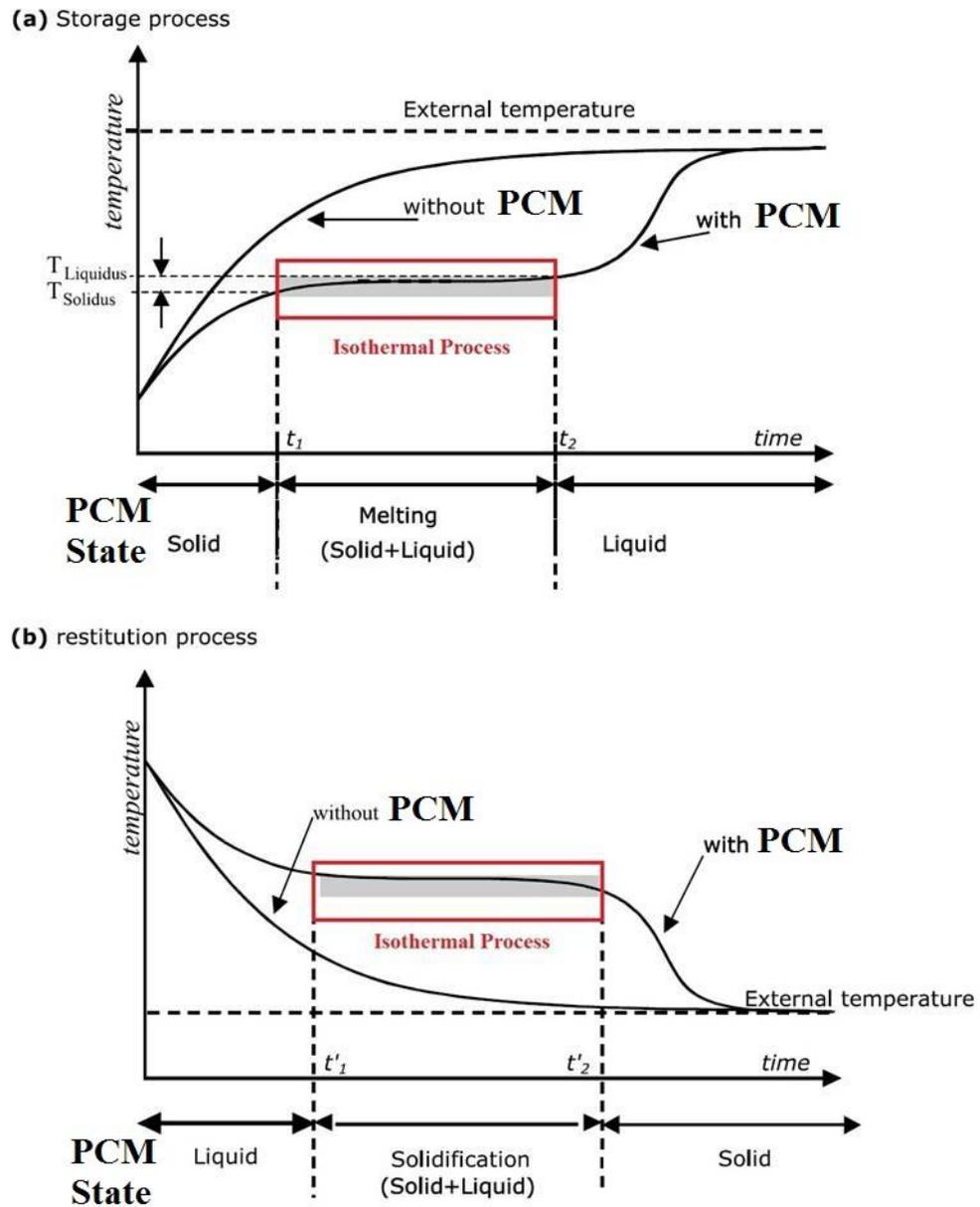
Figure 14: Schematic diagram representing the temperature variation occurring during the melting and crystallisation process. Diagram taken from [58] and edited on paint.

The use of this technology in CSP application has not yet seen the light of days, as more research into the storage of PCM and extraction of thermal energy might be needed. Furthermore development of composite system (Ceramic/Molten Salt) might provide a way of enhancing the thermal characteristics of molten salt.

2.6.3 Sensible Energy Storage

It is the ability of a solid, liquid or gas to store energy based on a temperature difference. The amount of heat stored is directly proportional to the density, specific heat capacity, and volume as well as temperature difference such that:

$$Q = \rho \times C_p \times V \times \Delta T$$

Q = Amount of energy (kJ)

ρ = Density (kg/m^3)

C_p = Specific heat capacity (kJ/[kg*K])

V = Volume in (m^3)

ΔT = Kelvin

This type storage is cheap and can include water, rock, ceramic bricks, sand, oil, air or any other materials. Each medium displays advantage and disadvantage such that water has a large thermal capacity, but a low density compared to rock or ceramic bricks. It is often used as a storage medium in domestic application such as space heating and to provide warm water at home or the office [59]. However its operating temperature (20-90°C) makes it unsuitable for other uses and usual substitutes would be oil or molten salt, which can function at temperature of up to 400°C for the former, and above 400°C for the latter making them appropriate for use at industrial level or for thermal solar power station [60, 61]. Both molten salts and oil are used as heat-transfer-fluids. However, due to their lower price and toxicity, as well as higher operating temperature, molten salts such as Solar Salts (60%NaNO$_3$-

40%KNO_3) are a good alternative. Still one of the disadvantage of using molten salts is their higher freezing point (≈222°C for Solar Salt) which imply that heat tracing need to be setup within CSP making use of this technology.

2.7 Heat Transfer Fluids and Thermal Storage Materials for CSP Applications

There are mainly two types of fluid which can be utilized in CSP applications; synthetic oil or molten salts. In term of synthetic oil, VP1 is currently the most utilize type of HTF but the latter displays some disadvantages which is pushing researchers and industrials to come up with a cheap alternative material. With an operating range varying between 12°C and 400°C, this synthetic oil starts to decompose above 400°C creating hydrogen and various other breakdown products. This is particularly dangerous to the plant as hydrogen can permeate the stainless steel causing cracks and therefore leaks to appear within the piping system. This oil is also dangerous to the environment and will easily pollute the soil which would have detrimental effect to the surrounding fauna and flora. Furthermore, its high vapour pressure means that the oil travels through the system as both liquid and gas phase in a pressurized environment of 25 bars or above. This also implies that the system has to be topped up with synthetic oil as the convolution of pipes is not totally hermetic and losses will occur. Finally the cost of using such material has risen over the years and is now reaching a significant percent of the total investment cost of the plant. One of the advantages of this oil is its high specific heat capacity at 400°C which is of 2.628 J/[g*K].

On the other hand, the Cp of molten salt is relatively low compared to VP1 with solar salt displaying a mean value of ≈1.55 J/[g*K]. Furthermore its high melting point entails heat tracing, such that the system is equipped with back up heaters to ensure the salt does not freeze within the pipes which would cause a blockage and would damage the system. However unlike VP1, it is not toxic and would not penetrate the soil if a leakage were to occur. Instead the salt would readily crystallize. Providing the system can be safely kept above crystallization, the maximum operating temperature of this salt is much greater than that of VP1 with Solar salt capable of handling up to 600°C. As efficiency of CSP plants increases with higher temperature, inorganic salt are a good alternative to propose. The low vapour pressure of solar salt also means that the travelling fluid will almost always be in the liquid phase allowing the system to run with low pressure. Another variable to take into account is the corrosion of inorganic salt which is highly dependent on the type of mixture used. Chloride salts are generally very corrosive whilst carbonate and nitrate salts have a lower corrosive nature which is why research is focused on the utilization of either nitrate or carbonate salt as HTF. On top of that, the purchasing price of salt is far lower than that of VP1 making it attractive to industries and particularly CSP applications.

However one of the key parameters in HTF is the specific heat capacity of the material. Indeed, this number relates to the amount of energy the fluid is capable of storing with an increase in temperature. This will directly affect the CSP plants providing a decrease in electricity prices as the energy density of the material is increased. Therefore research into the field of molten salt nano-fluid is a popular topic which is currently the focus of much

investigation and discussion. Nano-fluid has been a highly researched area in the last 20 years and discovery of its effects on thermal behaviour of low temperature fluid has been largely explored. This is not the case for high temperature materials.

2.8 Enhancing Thermal Properties of Non-Ionic Fluids with Nano-Particles

2.8.1 Heat Conductivity

Addition of nano-particles into a base liquid forms a two-phase mixture. Such a mixture (suspension) is termed nano-fluid.

Suspension of minute quantities of nano-particles in liquid solvents was first coined as 'nano-fluid' by Choi in 1995 [62]. With nominal size ranging from 1-100 nm, these nano-particles have been reported to display anomalous enhancement of the thermal characteristic of the fluid within which they are suspended. Lee et. Al (1999), reported that the addition of various fraction (0.1 vol.% to 0.5 vol.%) of Copper Oxide (CuO) and Aluminium oxide (Al_2O_3) of 20-40 nm, all increased the thermal conductivity of both ethylene glycol and water [63]. This was reaffirmed by Das et. Al (2003) who showed a maximum enhancement of 24.3% with 4.0 vol. % of Al_2O_3 and 36% with 4.0 vol. % CuO suspended in water [64]. Other base fluids such as pumped oil, glycerol and toluene have shown enhanced thermal conductivity with the minute addition (Maximum of 5.0 vol. %) of various nano-particles such as Al_2O_3, Au, TiO_2, Cu, CuO and Carbon Nano-tube (CNT) [65-72].

The complex nature of nano-fluids has made it difficult to model and reported data have showed that the size of the particle, concentration, particle surface properties, interaction between base liquid & particles, shape of the particles as well as the type of nano-particles utilized could affect the thermal characteristics in very different manners [64, 69, 73, 74]. The literature is full of papers proving and reporting these atypical improvements in the thermal conductivity [73], and recent theory & understanding of the gathered data point toward the effective medium theory by Maxwell as a good model for the prediction of thermal conductivity if aggregation of particles is taken into account [75, 76].

Furthermore the stability of a nano-fluid is also affected by the methodology used to stabilise them. The aim in suspending nano-particles in a fluid is to prevent their excessive aggregation and sedimentation over time. This can be achieved via a physical mean which makes use of an ultra-sonicator or via high-shear rate mixer with the aim of breaking potential agglomerate and homogenising the fluid [77]. Alternatively chemical stabilizers usually called dispersants surfactants are added to the mixture to enhance the stability of the fluid and prevent aggregation. The choice in the latter is highly dependent on the type of base fluid employed in the process [78]. Furthermore chemical alteration of surface properties of nano-particles (e.g. SiO_2) to enhance stability through the addition of chemically bonded side chain (e.g. Silane) has also been looked at by Yang et Al. (2010) [79] and probably others. Finally altering the pH of the solution is one of the ways to improve the stability of aqueous based nano-fluids [80, 81]. Whilst each of the method has an impact on the stability of nano-fluids [77, 78, 82], Xuan et

Al. (1999) recommended a combination of the technique previously mentioned to stabilize a suspensions [83].

2.8.2 Specific Heat Capacity

The storage of thermal energy is dependent on the degree of freedom of atoms within matter. Translational kinetic energy, rotational kinetic energy and potential energy in vibrational modes constitute the different form of energy into which heat transferred can be stored. The mode of storage is also dictated by the state of matter, as the atomic constraints will be different in gas compared to that of solid or liquid. A monatomic gas for example will transfer thermal energy only through translational motions, as rotational kinetic energy is dependent on the moment of inertia which is too small to be of any significance. The degree of freedom will change if the gas is composed of linear (CO_2) or non-linear (H_2O) molecules as all three modes of energy will be available in these compounds.

Table 1: Degrees of Freedom in Gas

	Monatomic	Linear molecules	Non-linear Molecules
Translational (x, y & z)	3	3	3
Rotational (x, y & z)	0	2	3
Vibration	0	3N-5	3N-6
Total	3	3N	3N

In solid, the atoms are packed in a regular or irregular lattice arrangement constraining the atoms to a specific location in space. This implies that translational & rotational kinetic energy cannot happen in this particular

state. Thus storage of thermal energy is only attainable through vibrational mode. The latter is due to connection between atoms which can be visualized as springs. The amount of oscillation of this lattice (thermal phonon) is dependent on the temperature and is well described by the Einstein or Debye theory of heat capacity.

Whilst there is a good theoretical understanding of heat capacity in both solid and gas, the same cannot be said of liquids. In this state, both translational and vibrational modes of energy storage take place. Devising a model for this type of system is difficult as the interactions taking place in this state are specific to the type of liquid employed. Yakov Frenkel in 1940s emitted the idea that above a certain frequency, molecule in a liquid could behave like a solid and therefore support phonon. Due to the increased mobility of atoms, only frequencies above the relaxation time of liquid allowed the shear wave to propagate. The model implemented by Bolmatov et. al 2012 predicted quite accurately the liquid Cp of 21 samples using Frenkel phonon theory [84].

With the literature agreeing on the positive effect of nano-particles on the rise of thermal conductivity in non-ionic base fluid, very little research was carried out on the Cp of such combination [85]. However, one could think of specific heat capacity as the direct opponent of thermal conductivity. Indeed measured in W/[m*K], thermal conductivity represents the transfer of energy whilst Cp (J/[g*K]) is define as storage capacity. If a HTF were to have a large thermal conductivity, one would think that its capacity to retain heat would be impaired as any heat stored would be readily given away. This is usually measured through thermal diffusivity (m^2/s) where:

$$\alpha = \frac{\kappa}{\rho C_p}$$

- κ is thermal conductivity (W/[m*K])

- ρ is density (kg/m^3)

- C_p is specific heat capacity (J/[kg*m])

And indeed this seems to be the case in non-ionic fluid where the specific heat capacity seems to decrease upon the addition of nano-particles and the increase in thermal conductivity. Measurements done by Zhou et al. 2008 showed that the suspension of Al_2O_3 nano-particles in water decreased its Cp with increased volume fraction [85]. This was also used to determine whether modelling of heat capacity using classical and statistical mechanism would agree with the obtained data, which it did, with the following equation [85];

$$C_{p,nf} = \frac{\emptyset(\rho C_p)_n + (1-\emptyset)(\rho C_p)_f}{\emptyset \rho_n + (1-\emptyset)\rho_f}$$

Where Cp, ∅, ρ, nf, n & f respectively represent specific heat capacity, volume fraction, density, nano-fluid, nano-particle and fluid. Furthermore tests carried by Pantzali's research team showed that the addition of CuO nano-particles to water also caused a decrease in Cp of 35.4% with the addition of 8% v/v fraction of nano-particles. Similarly to Zhou et al. 2008, a decrease in volume fraction of CuO nano-particles cause an increase in Cp such that 2% v/v of CuO only led to 11% loss in Cp [86]. Both papers [85, 86] argue that the equation from Pak & Cho 1998 [87] for the calculation of Cp over-estimated its value. This is sustained by Saeedinia et, al. 2012 who also demonstrated the decrease in Cp of oil when nano-particles of copper

oxide (0.2%, 0.5%, 1.0% & 2.0%) were added [88] and concurred that Pak & Cho 1998 Cp model over-estimated the results.

It seems that the publications agree on the fact that stable suspension of nano-particles within a non-ionic fluid leads to a loss of specific heat capacity which is dependent on the percent present. But report on enhancement of Cp was observed by Nelson (2007) where the addition of 0.6 weight % of exfoliated graphite to polyalphaolefin enhanced the specific heat capacity by 50% [89]. The obtention of those results are surprising but could be explained by the interaction of exfoliated graphite sheets with polyalphaolefin.

2.9   Enhancing Thermal Properties of Ionic Fluids Using Nano-Particles

The research into non-ionic nano-fluid has showed us that providing the nano-powders are well suspended and disperse, there is an increase in the thermal conductivity and a decrease in specific heat capacity of the fluids. However research carried out by Shin et al. (2011) on ionic fluid demonstrated that the addition of 1.0 wt% of silica nano-particles to a binary mixture of lithium carbonate & potassium carbonate (62:38 ratio) led to a Cp enhancement of 19-24% in liquid status (525°C - 555°C) compared to the base salt [90]. With that, it was showed that the size of the nano-particles (5, 10, 30 and 60 nm diameter) did not seem to affect the increase in Cp for SiO_2 [14]. These results are unusual as the specific heat capacity of oxide nano-particles ($\approx$1.0 J/[g*K]) is lower than that of salts. However experiments

have showed that nano-particles generally display a higher energy structure than coarse grain due to their high surface area to volume ratio leading a larger blue shift in infrared spectroscopy [91, 92]. Indeed due to their smaller size, nano-particles have a greater proportion of exposed atoms and thus an enhanced surface energy which cannot be neglected. Research by Tiznobaik et al. 2013 pointed out that the enhancement in Cp might be due to the formation of nano-structures which can be negated through the prevention of electrostatic interaction between nano-particles and ions [93]. Indeed the addition of 0.02 wt% of sodium hydroxide to a binary mixture of carbonates containing 1.0 wt% SiO_2 led to similar Cp to that of pure salts whilst its absence promoted a rise of ~26% [93]. This could imply that electrostatic forces within ionic fluid might play a role in specific heat capacity enhancement.

Recent theories points toward three possible mechanisms in the enhancement of specific heat capacity [94]:

- Mechanism 1 relates to the fact that the specific heat capacity of nano-particles is larger than its bulk value. If one imagine that a sphere is made up of thousand of atoms, and that the latter are constrained and held together by spring-like bonds. Then the atoms on the surface, which are exposed, will have a lower vibrational energy than those found on the inside of the sphere. Therefore if the surface area to volume ratio is increase, the amount of 'exposed' atoms will drastically rise leading to an increase in specific heat capacity which would be stored through an increased vibrational energy of the 'exposed' surface atoms of the sphere [91, 95].
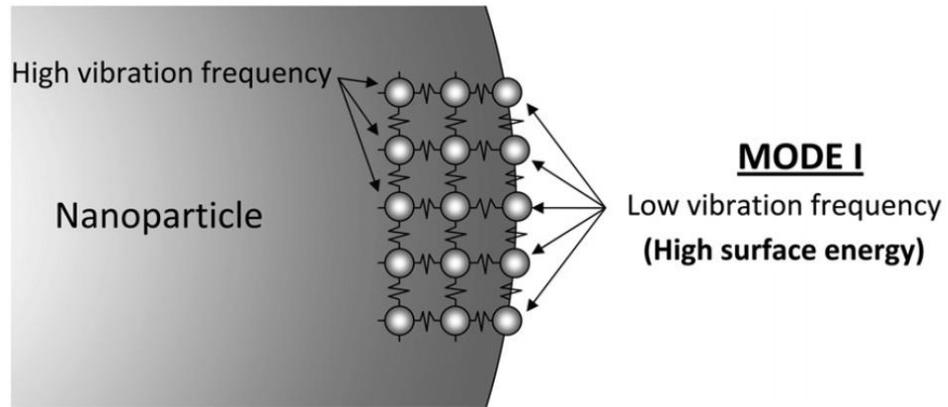
Figure 15: Schematic representation of the exposed atoms of a nano-particle which display high surface energy [94].

- Mechanism 2 relates the solid-fluid interaction energy, also called Kapitza resistance, which occurs during the transfer of heat between the fluid phase (base liquid) and the solid phase (nano-particles). This thermal resistance could be considered negligible on macro-scale, but nano-scale displays a large surface area to volume ratio increasing the effective specific heat capacity. This thermal resistance would act as a storage unit holding the energy within this boundary [96, 97].
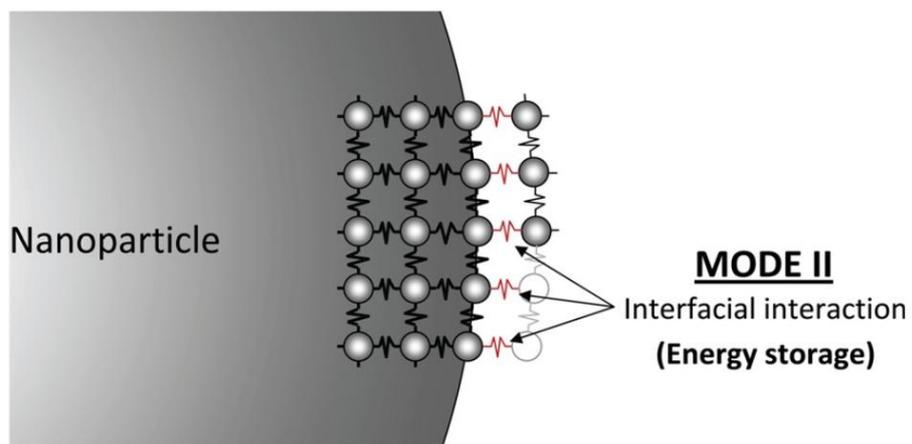
Figure 16: Depiction of the mode of storage in mechanism 2 where the thermal energy would be accumulated at the liquid/solid interface [94].

- Mechanism 3 is about the liquid/solid interaction whereby the liquid molecule would have to rearrange around the nano-particle forming a semi-solid layer or adhesion layer. The molecule within this layer would display a larger level of constraints contributing to higher thermal properties than bulk liquid promoting an increased specific heat capacity. This change in configuration was reported by Oh et Al. (2005) with the ordering of liquid aluminium using sapphire [98].
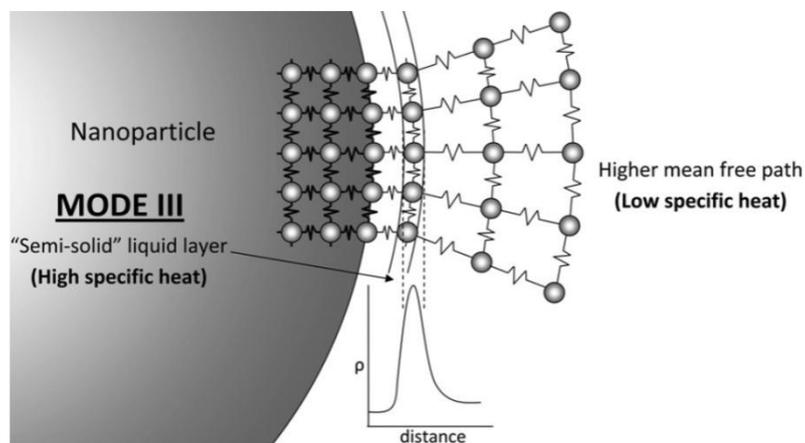
Figure 17: Graphical representation of liquid layering around nano-particles [94].

Whilst it is not clearly known which of these mechanisms is prominent (if any), it seems that the behaviour of nano-particles is different between ionic and non-ionic liquid.

2.10 Summary

This chapter's aim was to summarise the relevant literature surrounding renewable energy technologies, and how the research and development, within the area of specific heat capacity enhancement of HTF could positively affect the implementation of CSP around the world. However, a vast gap in the literature can be seen when it comes to specific heat capacity measurements, with most of the papers published concentrating on the use of carbonate salts. Very little has been done on nitrate salts.

Furthermore the basic characteristics of the salt mixtures are difficult to locate, and no study has concentrated its effort on defining these. Providing that any enhancements in a material is determined by its baseline, it is crucial to ensure the results of pure inorganic salt mixture are within an acceptable range before any other experiments are conducted.

This PhD thesis will therefore concentrate on defining the basic characteristic of solar salt and investigate the effect of various nano-particles on the thermo-physical characteristics of the salt with particular attention paid to specific heat capacity measurements.

Chapter 3 Materials & Methodologies

This chapter starts with a description of preliminary results attained which provided vital information for future design of the experiments. This is followed by a description of the materials used as well as the procedure employed to produce the samples. The chapter is terminated by a description of the equipments used for characterisation of the salts as well as an explanation of how they operated and the way in which they were calibrated for the purpose of the tests.

3.1   Preliminary Experimental Results

The initial first step taken in this research was to try and validate published data by mimicking the methodology of Banerjee's 2010 research which was concentrated on the enhancement of specific heat capacity in binary carbonate salt using 1.0 wt% silicon dioxide [13]. The reason behind the choice of this particular paper was the obviously large enhancement seen in the specific heat capacity which could then be tried on nitrate salts. If the methodology was successful, the aim was to test it on nitrate salt with a variety of different nano-particles. Following the paper's protocol (ratio), 4.59 grams of Li_2CO_3 and 5.26 grams of K_2CO_3 were dissolved in 1 litre of deionised water. Then 0.15 grams of silicon dioxide nano-particles were added and dispersed through sonication for a couple of hours until a transparent milky solution was obtained (Fig. 18). In the same manner, a control exempt of nanoparticles was produced (4.66 grams of Li_2CO_3 + 5.34 grams of K_2CO_3 in 1 litre). The dispersion of nano-particles seemed stable over the next few days with aggregation only starting to appear after a few weeks without sonication. The aggregates were then easily broken apart through another round of sonication and re-dispersion of the nano-particles was easily achieved. The following step was to evaporate (on a hot-plate at 60°C using Petri-dished) and fully dry the crystallised mixtures at temperature above 150°C to remove any water molecules bound to the salt forming hydrates. Ensuring that the salt was fully dried was extremely important so as to prevent the hermetically sealed capsule from blowing up due to the pressure build up from the vaporization of water molecules.

The crystallised salt obtained (Fig. 18) showed that the rate of evaporation of water was not homogenous and some areas displayed much finer grain size than others. The salt crystals were removed using a clean razor blade and both coarse and fine grains were mixed together and tested.

Whilst the methodology for producing the salt was similar to what was written in Banerjee's 2010 paper [13], the actual DSC equipment differed. Therefore the thermal cycle was altered. When using High Pressure Stainless Steel (HPSS) 30 µl pan, the following cycle was used:

- Isothermal ramp of 5 minutes at 530°C
- Dynamic ramp from 530°C to 560°C at 10°C/min
- Isothermal ramp of 5 minutes at 560°C

However when platinum pan (30 µl) were utilised a slightly different cycle was employed:

- Isothermal ramp of 5 minutes at 520°C
- Dynamic ramp from 520°C to 560°C at 10°C/min
- Isothermal ramp of 5 minutes at 560°C

There were no particular reasons behind this slight change of thermal cycle aside from the fact that more data could be gathered. The obtained results were very interesting as the variation was extremely different depending on the type of pans used when nano-particles were present. However little variation was seen when pure carbonate salt was tested.

Indeed when using HPSS pans (Fig. 19 red and green square), the data was similar to that of the paper [13] (Fig. 19 pink and black dotted line) as showed below with enhancement of around 100% seen when nano-particles

were added, although the standard deviation in data was relatively high with a maximum of ±6.7%.
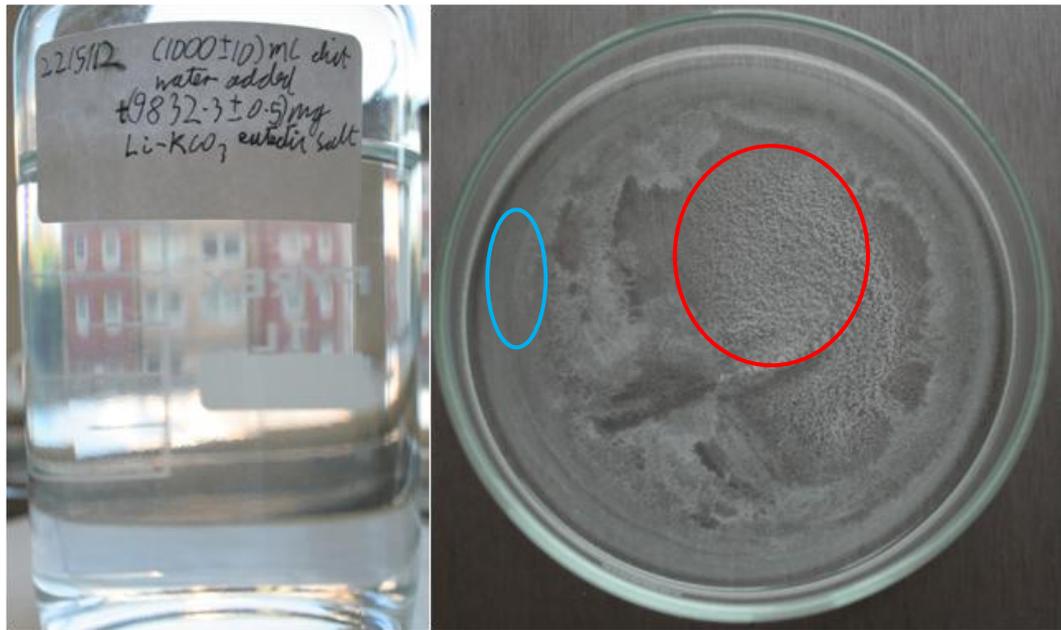
Figure 18: Left picture showed the nano-particle suspension of 1.0 wt % SiO$_2$ in 1 litre of deionised water with a eutectic mixture of carbonate salt (46.6 wt% Li$_2$CO$_3$ + 53.4 wt% K$_2$CO$_3$) dissolved in it. Right picture presented the crystallised carbonate salt where areas of the Petri-dish displayed coarse grain probably caused by faster evaporation rate (red circle) whilst the grain size on the periphery seemed smaller (blue circle).

Using platinum crucibles painted a totally different picture in term of the results gathered as a small decrease in Cp (≈ -1.77%) was seen when nano-particles were utilized. But the results for the pure carbonate salt were similar regardless of the type of pan used (Table. 2). This was not the case when nano-particles were involved as the difference between HPSS pan and Pt pans is around 100% which raised the question as to where did the difference came from?
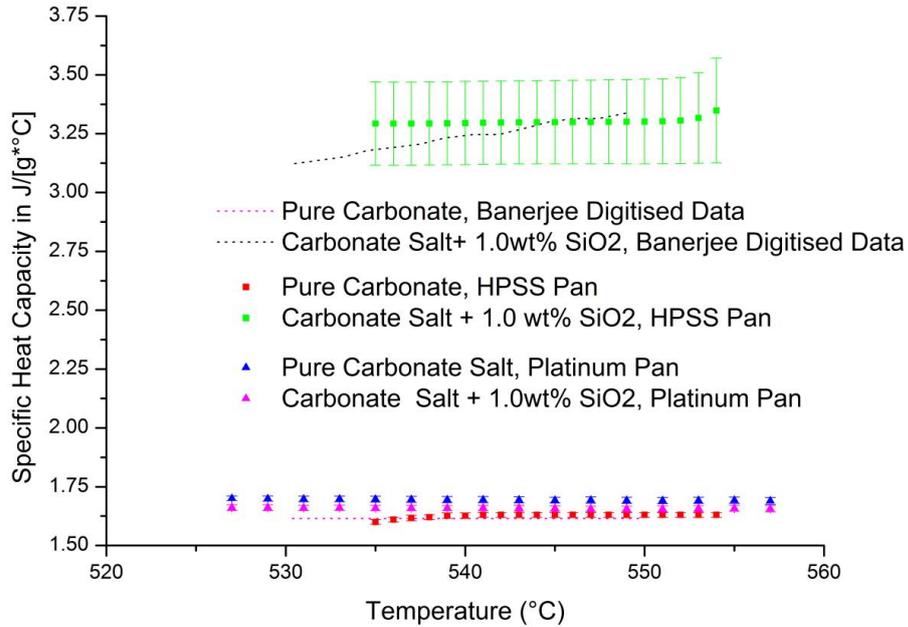
Figure 19: Graph displaying the Cp of a binary carbonate salt mixture (46.6 wt% Li$_2$CO$_3$ + 53.4 wt% K$_2$CO$_3$) with and without 1.0 wt% silicone dioxide nano-particles. The black and pink dotted line represent the digitised data from the following paper [13], whilst the red and green squares are results obtained using HPSS pans. The blue and pink triangles were made using of platinum crucibles.

Table 2: Percentage difference in Cp between published data compared to HPSS and Pt pans for inorganic carbonate salt mixture without any nano-particles present.

	Platinum Pan (Pt)	High Pressure Stainless Steel (HPSS)	Banerjee 2010 Digitised Data
Overall average in Cp in J/[g*°C]	1.69	1.63	1.61
Percentage Difference with Published Data	4.99	1.24	0.00

With the same method used to produce the samples and the major differences only showing up when nano-particles were employed, it was concluded that pressure build up inside the capsule could affect the nano-particles in such a way that the enhancement in Cp seen is an artefact.

These tests revealed the challenging nature of measuring specific heat capacity particularly with corrosive material such as inorganic salts. Furthermore it also questioned the published data and the actual procedure used to produce the salt mixture. With this in mind, the processes of salt production, characterisation and testing were re-design to encompass all the challenges previously encountered when working with carbonate salts.

3.2   Materials: Inorganic Salt & Nano-Particles

The main components used in the development of eutectic salts were either nitrate or carbonate based compound. Purchased in anhydrous forms with varying grains size and shape depending on the manufacturer, the powders were generally grinded using different processes which will be described later on.

Regarding, the carbonate mixture mentioned above, the following salts and ratio were used: anhydrous lithium carbonate (99.0 % Pure) (46.6 wt.%) (MERCK) and potassium carbonate (99.0 % Pure) (53.4 wt.%) (FISHER BIOREAGENT).

The binary nitrate mixture was composed of anhydrous sodium nitrate (FISHER) (98% Pure) (60 wt. %) and potassium nitrate (SIGMA-ALDRICH) (98% Pure) (40 wt. %), this ratio of salt was the basis for all the subsequent tests carried out.

The other components present in some of the mixtures were nano-particles with percentage weight ratio varying from 0.1 to 1.5. The specifications of the nano-particles were taken from the manufacturer sites:

Copper Oxide (CuO):

Producer: Nanophase Technologies Corporation

- Purity: 99.0+%
- APS: 29 nm (determined from SSA)
- SSA: 32 m^2/g (BET)
- Appearance: Black powder
- True Density: 6.5 g/cc
- Morphology: Equi-axed and nearly spherical
- Crystal Phase: Monoclinic

Titanium Oxide (TiO):

Producer: NanophaseNanoTek

- Purity: 99.5+%
- APS: 34 nm (determined from SSA)
- SSA: 45 m^2/g (BET)
- Bulk density: 0.25 g/cc
- True density: 3.95 g/cc
- Morphology is nearly spherical
- Crystal phase: 80% anatase and 20% rutile

Zinc Oxide (ZnO):

Producer: Nano-structured and Amorphous materials

- Purity: >99%
- Bulk Density: 0.30-0.45 g/cm3
- APS: 40 nm
- SSA: 50-70 m^2/g

Silicon Dioxide (SiO$_2$):

Producer: Sigma Aldrich

- Assay: 99.5% trace metals basis
- Form: Spherical, porous
- Particle size: 5-15 nm (TEM)
- Surface area: 590-690 m^2/g (TEM)
- Bp: 2230 °C (lit.)
- Mp: >1600 °C (lit.)
- Density: 2.2-2.6 g/ml at 25 °C
- Bulk density: 0.068 g/ml

Copper (Cu):

Producer: US Research Nanomaterials

- Cu purity: >99%
- Form: Spherical
- APS: 70 nm
- SSA: 6-8 m^2/g

3.3   Sample Production

The production of eutectic salt can be done either by physically mixing the different powders together with the aim of attaining a homogenous mixture or by taking advantage of the solubility of salts into water.

3.3.1 Powder Mixing

The inorganic salts were weighed and mixed together following the ratios mentioned above (Section 3.2). Then the powdered mixtures were inserted into clean glassware. The latter had been sonicated with purified water and

surfactant as well as dried in an oven at 80°C before been used. Stainless steel (3 or 9 mm diameters) or ceramic (27 mm diameter) ball bearings were added inside glass or ceramic jar and the latter was placed onto a mill to physically crush and mix the samples (Fig. 20). The ball bearings were sonicated in purified water as well as acetone before been dried in the oven at 80°C prior to their utilization. This step was to ensure the cleanliness of the bearings and remove any rust particles on their surface to lower contamination of the salt. The type of bearing or container used depended entirely on the amount that needed to be produced. Low quantities could be created using a pestle and mortar whilst larger amounts will have required the use of vessel with the correct proportion.

The milling process (80-100 rpm) was checked every half-hour to monitor the consistency of the powders and ensure that it was not sticking to the side of the wall. Once flour like consistency was attained which roughly equated to a grain size ranging from 1 μm to 100 μm, the process was stopped. This took around 2 to 3 hours.

After obtaining a homogenous binary mixture, different types of nano-particles were introduced in the eutectic salt with the following ratio: 0.1 wt%, 0.5 wt%, 1.0 wt% and 1.5 wt%. This was followed by ball-milling for 30 to 60 minutes to try and ensure that the nano-particles had been well dispersed within the salt. The mixtures were then sieved to remove the few large aggregate remaining and kept in labelled jars ready for testing (Fig.21).

Figure 20: Top Picture: Different size containers used to produce various amount of salt mixture ranging from a few milligrams to a few kilograms. Bottom-left Picture: Bearing used in the milling process (3 and 9 mm stainless steel, 27 mm ceramic). Bottom-right picture: Milling unit.

Figure 21: Example of binary nitrate salt doped with copper oxide nano-particles samples produced using the milling process (0.1 wt. % CuO, 0.5 wt. % CuO, 1.0 wt. % CuO and 1.5 wt. % from left to right respectively). In this particular case, a glass jar was used to mix a total amount of 50 grams per batch. 600 grams of 9 mm stainless steel balls were added to grind the powder.

The main advantage of this method was its scalability which could allow tonnes of materials to be mixed in that way. However its effectiveness in dispersing nano-particles would be difficult to determine.

3.3.2 Liquid Process

This method of production involved the dissolution of salts in deionised water, with nano-particles added to the mix and sonicated for a few hours to disperse the latter. This was followed by the transfer of this solution into Petri-dishes for evaporation with further drying to ensure that all the hydrates were removed. The process which was utilized for the production of carbonate salt (Section 3.1) was tested with nitrate salt to observe if there were differences in specific heat capacity between the solid and liquid method of production. One of the main advantage of this technique was its ability to allow good dispersion of the nano-particles to be carried out. However, up-scaling this particular type of production would not be feasible due to the large expenditure of water and the cost associated to this process.

3.4 Experimental Procedures

Using differential scanning calorimeter (DSC) (Mettler Toledo, DSC1/700), thermo-gravimetric analyser (TGA) (Mettler Toledo, LF/1100), scanning electron microscopy (SEM) (Gemini / Zeiss Leo 1530) and rheometer (Anton-Paar), various thermo-physical properties of the salts will be tested.

3.4.1 Differential Scanning Calorimeter: Principles & Methodology

3.4.1.1 Introduction to DSC

This particular apparatus allows the user to analyse the physical or chemical response taking place within a sample by monitoring the energy changes occurring throughout heating, cooling or isothermal cycles. It basically tracks the heat flow into or out of the sample (calorimeter) against that of a reference (differential) during a constant or dynamic thermal cycle (scanning) hence the name differential scanning calorimeter (DSC).

Also referred to as enthalpy, these energy changes can be quantitatively measured and the equipment allows to pin-point at what temperature these events will occur. The user is therefore able to characterise a range of chemical or physical changes taking place within the analysed substances (melting, crystallisation, glass transition, solid-solid transition, enthalpy of fusion or crystallisation, reaction enthalpy, polymerisation and pyrolysis). Most of these transitions will either be exothermic or endothermic.

- Exothermic: Heat is released from the sample.
- Endothermic: Heat is taken into the sample.

The ease of production of sample and the small amount of substances required makes the use of this equipment a versatile technique which provides a rapid and efficient way of analysing/characterising any materials.

3.4.1.2 Heat Flow & Enthalpy Measurement

The main function of this equipment is to detect the differential variation in heat flow (y-axis in mW) against that of time/temperature (x-axis in seconds, minutes or °C) (Fig. 22). The latter will vary depending on the material been tested and the thermal cycle utilized. This variation in energy (1 milli-Watts = 1 milli-Joules per seconds) is only useful providing the instrument is well calibrated and dependent entirely on the effect of the reference. Indeed the measurements are not absolute as the instrument determines the difference in heat flow between the sample and the reference (empty) which should both be carried out in the same crucibles.

Depending on the equipment used, the endothermal reaction can either be set up in the upward or downward (Fig.22) position. Whilst this is generally dependent on the manufacturer, the general rules are that endothermic reaction are down in heat flux DSC and up in power compensated DSC as the latter 'compensates' for any physical or chemical change by inputting more power to keep an isothermal temperature. Heat Flux is down for endothermal because the heat is absorbed by the sample during enthalpy change. The latter is dependent on the stability of the weight (no gain or loss) and calculated through the integration of the area under the curve.

Total area under the curve: 185.533 mJ (Yellow Crossed Area)

Sample weight: 6.518 milli-grams

Enthalpy of Change: 185.533 / 6.518 = 28.465 J/g
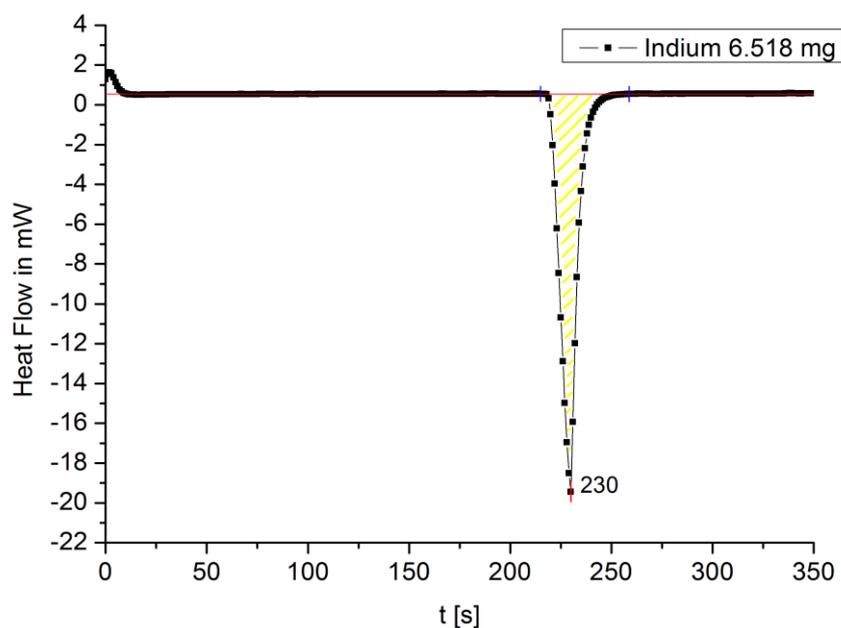
Figure 22: Graph displaying Heat Flow (mW) against Time (s) for the melting of Indium

3.4.1.3   Specific Heat Capacity Measurements

The specific heat capacity is referred to as the amount of energy required to raise the temperature of 1 gram of a substance by 1°C or 1K with units quoted as J/(g*°C) or J/(g*K). Also designated as Cp, as it is obtained at constant pressure, the specific heat capacity can be quantitatively measured using a DSC. The manner in which to achieve that is by measuring the heat flow of a blank curve, a sapphire standard and a sample on the same thermal cycles consisting of a dynamic ramp sandwiched between two isothermal steps (Fig. 23). The blank curve is then manually subtracted from both the sapphire and the sample (Fig. 24).
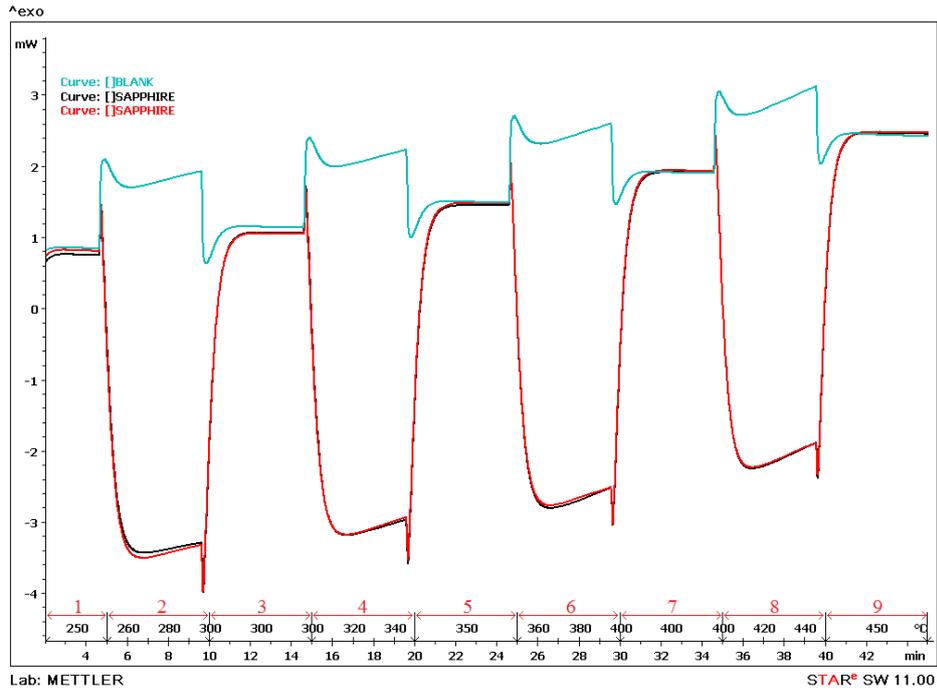
Figure 23: Graph displaying the Blank run in <u>Blue</u>, the Sapphire curve in <u>Red</u> (27.737 mg) and the Sample been tested in <u>Black</u> which is also sapphire (27.737). 5 minutes isothermal are used with heating rate of 10°C/min.
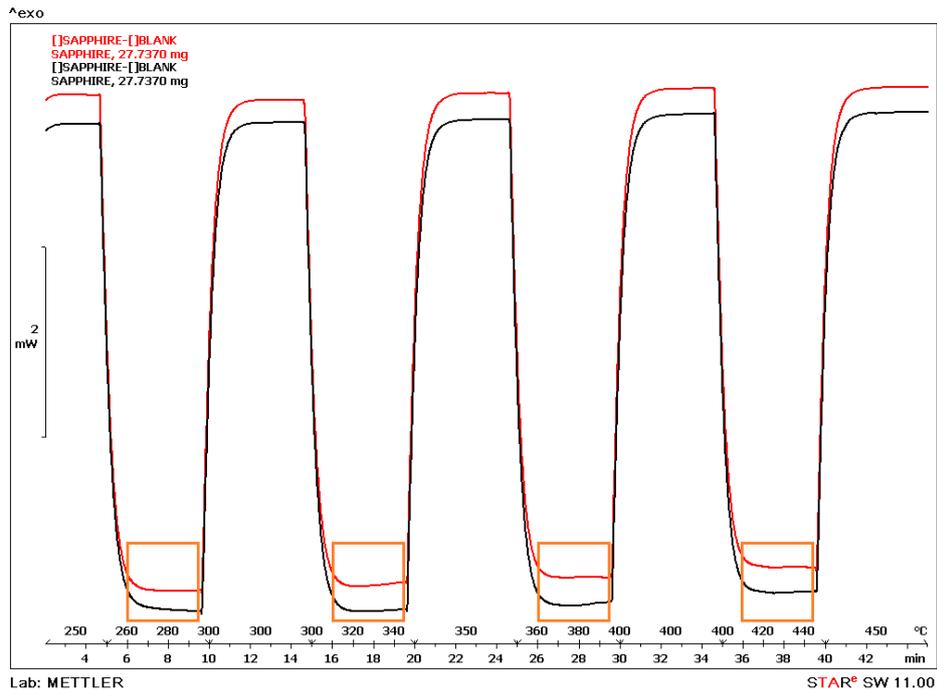
Figure 24: Manually subtracted blank from both sapphires (<u>Black & Red</u>). The orange box represents the dynamic part of the thermal cycle which is used by the software package for specific heat capacity measurements.

The Mettler Toledo software package allows the user to highlight and calculate the Cp from the dynamic part of the cycle by boxing and selecting 'subtracted sample-blank curve' and 'sapphire-blank curve' (Fig. 24).

The software then displays the obtained calculation as specific heat capacity ($J.°C^{-1}.g^{-1}$) versus temperature (Fig. 25). The results are usually exported to excel or origin for further analysis. It is to be noted that the results are taken a few degrees Celsius after and before the start and end of the dynamic segment as only the linear part of the curve (Fig. 24: Orange Box) is useful in the analysis of the data as the equipment needs a bit of time to settle in this dynamic equilibrium.
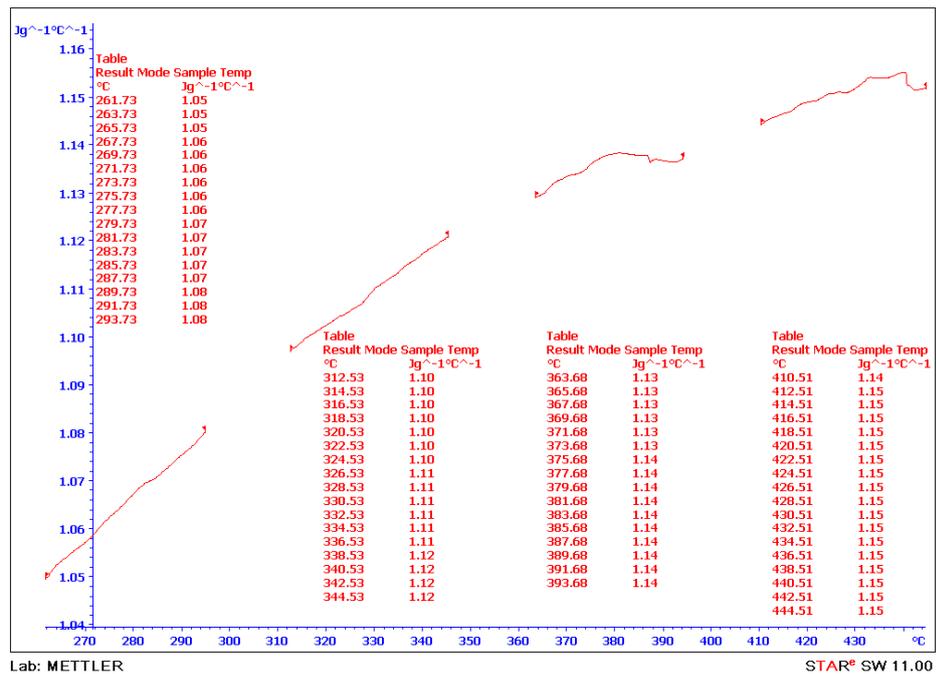
Figure 25: Calculated Cp of Sapphire from 261°C to 444°C.

The current setup used to measure Cp follows the ASTM E-1269-05 standard whereby the known value of the sapphire's Cp standard is used to calculate the value of measured sample following the equation below:

$$C_{Sample} = Cp_{Sapphire\ Reference} * \frac{HF_{Sample}}{HF_{Sapphire\ Reference}} * \frac{W_{Sapphire\ Reference}}{W_{Sample}}$$

C $_{Sample}$ = Cp of Sample in J/(g*K)

Cp $_{Sapphire\ Reference}$ = Cp of Sapphire in J/(g*K) at a define temperature

HF $_{Sample}$ = Heat Flow Sample in mW

HF $_{Sapphire\ Reference}$ = Heat Flow Sapphire in mW

W $_{Sapphire\ Reference}$ = Weight in mg of Sapphire

W $_{Sample}$ = Weight in mg of Sample
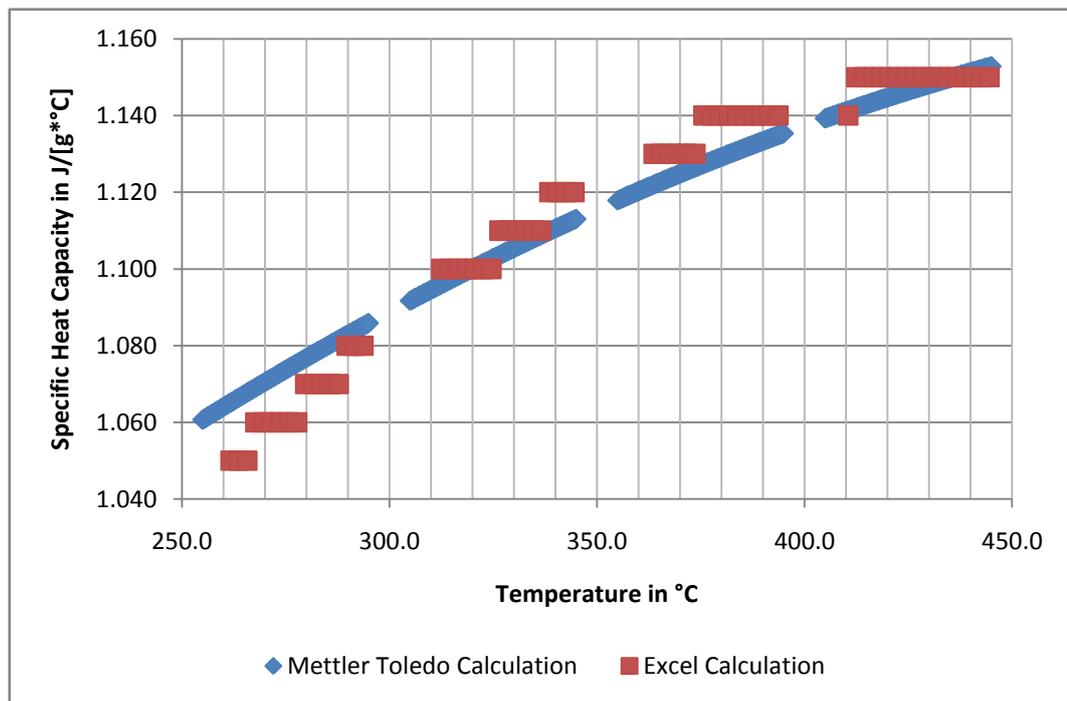
Figure 26: Graph showing the Cp measured using Mettler Toledo Software compared to the calculated values using the raw data.

The difference in calculated data is minimal and shows that this equipment operates and calculates Cp following standard criteria.

Most DSC equipments will come with a software package designed for that purpose (Cp measurements) where the subtraction can be automated or not

depending on what the user wants to achieve. Providing that the instrument is stable and well calibrated, a single blank and sapphire is required to calculate the Cp of many samples if and only if the same thermal cycle and reference are utilized. The thermal cycles used also has its importance as any thermal drift needs to be avoided. This can be achieved by using shorter dynamic range between isothermal or increasing the rate of scanning. Common guideline advises the user not to employ a dynamic range above 100°C or greater than 5 minutes to obtain precise and reliable results. Furthermore isothermal steps of minimum 5 minutes (Fig. 23) are needed to compensate for any thermal drift occurring after a dynamic ramp. Regarding the scanning rate for heat capacity measurement, 10°C/min is the commonly used rate of heating employed in such tests.

3.4.1.4 Calibration of DSC

Before making any measurements with any instruments, it is important to know whether the latter is calibrated or not. Indeed heat flow and temperature need to be measured very accurately as they will be utilized in the production of measurements and in most cases it is important to calibrate with element which span the entire range of the tests been carried out so that interpolation is carried out rather than extrapolation which would be less accurate.

In most cases Indium (In) and Zinc (Zn) are employed to calibrate this apparatus as the latter have very well defined heat flow and melting points as showed below:

Table 3: Reference materials used by Mettler Toledo for DSC Calibration

Substance	Temperature of Fusion	Enthalpy of Fusion	Order Number
Indium	156.6°C	28.5 J/g	ME 00119442
Zinc	419.6°C	107.5 J/g	ME 00119441

The software used has built-in ready to use checks for both Indium and Zinc to verify whether the apparatus is calibrated within the set limits which are:

For Indium; 27.85 to 29.05 J/g for the latent heat and 156.3°C to 156.6°C for the melting point of this metal

For Zinc; 103.7 to 111.3 J/g for the latent heat and 418.9°C to 420.3°C for the melting point of this material.
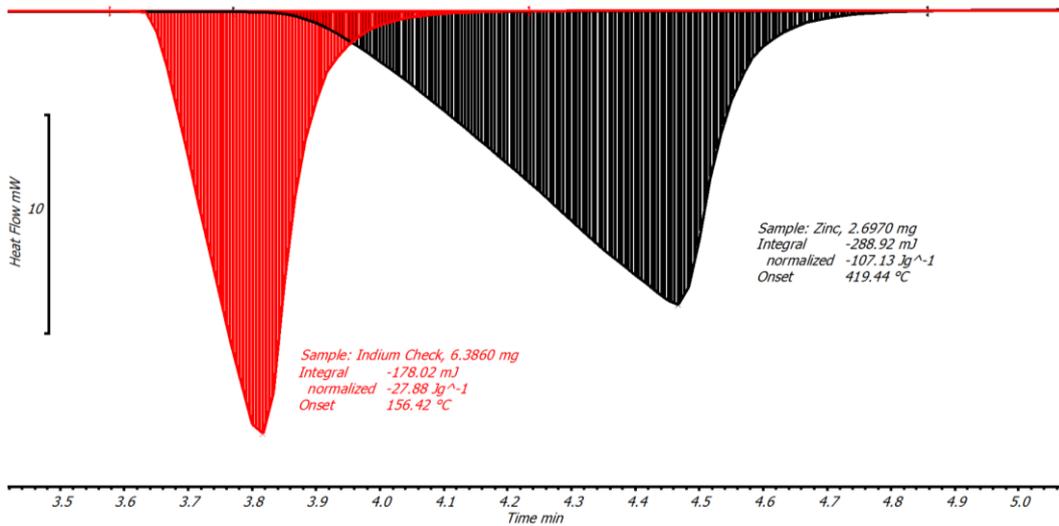
Figure 27: Indium and Zinc checks confirmed that the instrument was correctly calibrated (In – Hf = -27.88 J/g, Onset = 156.42°C _ Zn – Hf = -107.13 J/g, Onset = 419.44°C).

3.4.1.5 Heat-Flux DSC

This system is composed of a single furnace containing the sensor upon which, both the sample and reference are placed and heated up according to the thermal cycle pre-programmed. A gas inlet allows of constant flow (usually 50 ml/min) of nitrogen to carry away any volatiles produced during the experiment.
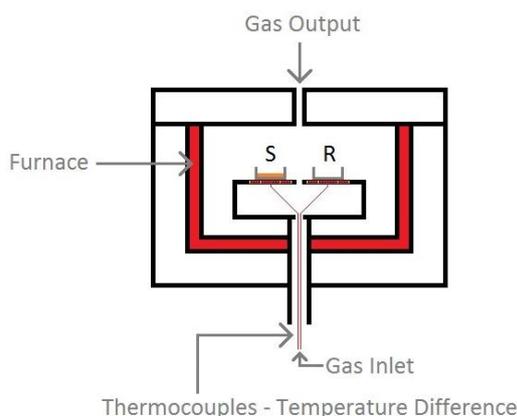
Figure 28: Schematic diagram of the Mettler Toledo Furnace where S represents the sample and R the reference.

The sensor in this heat flux DSC is composed of two areas (S & R) where the sample and reference are placed. Containing a total of 56 thermocouples (28 on sample side and 28 on reference side), the latter are evenly spread in a star shape pattern within the inter-space between the green and black concentric circles such that 14 evenly spread thermocouples measure the sample (green boundary) whilst the other 14 measure furnace temperature (Black boundary) (Fig. 29).
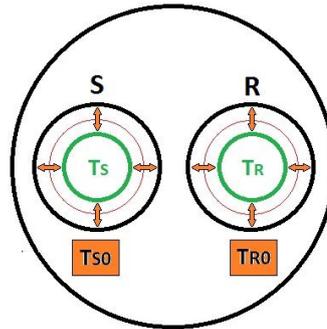
Figure 29: Schematic of DSC sensor. Labelled in green (T_S& T_R) are the areas where the crucibles come into contact with the sensor. The area labelled with the orange arrows is exposed to the chamber.

Based on Georg Ohm law ($I = \Delta V/R_e$) which is analogous to Fourier's law of heat conduction, the following equation is utilized:

$$q = \frac{\Delta T}{R}$$

Where q is the heat transferred in watts, ΔT is the temperature difference in Kelvin or °C whilst R is the resistance K or °C/W. In this system, the heat flow is impeded by the sample pan, the sample if present and the ceramic layer covering the thermocouple. Thus R is defined as:

$$R = \frac{l}{kA}$$

Where l is the length in m, k is the thermal conductivity in W/(m*K or °C) and A is the area in m^2.

In this equipment, the thermocouples average the different in temperature between the sample and the reference following the equation below:

$$\frac{dq}{dt} = \frac{1}{R}\left(\sum_{i=1}^{N}(\Delta T_{S0})_i - \sum_{i=1}^{N}(\Delta T_{R0})_i\right)$$

Where N is the number of thermocouple, ΔT_{S0} equates to difference between the sample and the furnace temperature whilst ΔT_{R0} is the difference in temperature between that of the reference and the furnace.

3.4.1.6 Sample Preparation

Any samples analyzed in a DSC need to be carefully prepared so as to avoid damaging the sensor. Because of the utilization of inorganic salt as a testing material, it was important to ensure the cleanliness of the preparation surface so as to prevent any salt crystals sticking to the bottom of the crucible. The latter would melt between the bottom of the pan and the sensor causing irreversible damage to the latter eventually leading to an 'ERROR 46' message displayed. This would indicate that the sensor was broken and needed to be replaced as showed below:

Figure 30: Damaged sensor due to the contamination of the bottom of the crucible. The red circles represent the areas where the salt has corroded the ceramic surface eventually reaching and damaging the thermocouples embedded below.

3.4.1.7 Crucible Type: Aluminium

To carry out the tests, different types of metallic crucible were trialled. The first ones were aluminium pans which displayed a maximum temperature of 600°C. Above this limit, the aluminium can start to alloy with other materials present in the sample. Furthermore it is always wise to test beforehand

whether any reactions between the samples and the aluminium might occur at high temperature to prevent damaging the sensor.

A few samples were prepared in standard 40 µl aluminium pan with their corresponding top which were pierced with a needle and crimped. This was done to protect the sensor and prevent any pressure build up which might have led to the capsules exploding within the furnace.

Figure 31: Composite picture of sample production.

The tests were carried out with 22.000-24.000 mg of samples which were inserted in the container unless a blank or reference was produced in which case the crucibles were left empty. Following this the lid was crimped using Mettler Toledo crimping tool which does not remove any metal in the process such that the weight of the pan does not vary.

However repeated heating and cooling cycles of the aluminium pan as well as the force applied on the edge of the crucible by the robotic hand gradually

led to its deformation. This meant that the bottom of the crucibles were not flat and could, in some cases, not be picked-up by the robot. This has also led to crucible been picked up and dropped from the robotic hand.

Figure 32: Round crimped aluminium crucible on the left prior to tests been carried out whilst on the right is the effect of repeated testing on the shape of the crucible which is distorted (edge is bent). The weight of these aluminium pans is generally located between 49.000 mg to 50.000 mg.

The later are not re-usable and have to be thrown away.

3.4.1.8 Crucible Type: Stainless Steel

A minority of samples (only preliminary tests) were also trialled in 30 µl high pressure (150 bars) stainless steel crucible with gold plate copper seals. The latter uses an hexagonal crimping tool screwing the top plate to the bottom one. The filling process of the crucible was similar to that of aluminium with 10.000 - 15.000 mg of carbonate salt added, except that the crimping tool was specific to this type of pans.
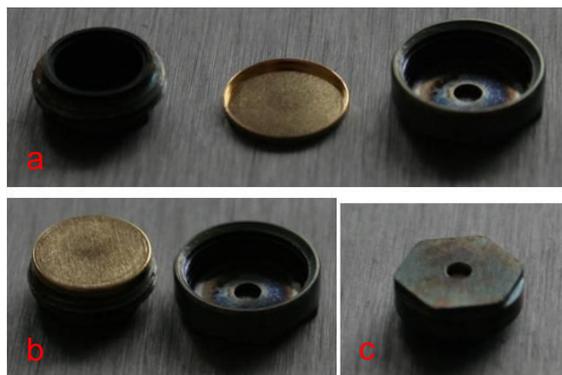
Figure 33: 30 µl stainless steel high pressure capsule showing the various parts and how they are assembled (a - c).

The production of those samples was closely monitored to prevent the explosion of the capsule due to a build up in pressure. The latter would have had a catastrophic effect on the DSC sensor. As salt can absorb moisture from the air over time and because of the high vapour pressure of water, it was crucial to melt the samples before sealing them to minimize the entrapment of water moisture. This type of crucible could only be re-used for a couple of tests and problem with leaking of sealed capsules was the major concern when using the latter.

3.4.1.9 Crucible Type: Platinum

The majority of tests were carried out with platinum pans. They display very high melting point, are resistant to corrosion, do not suffer from distortion upon repeated heating & cooling and were not affect by the robotic hand always keeping the same shape.

Figure 34: Platinum 30 µl pan used for most of the DSC tests.

Furthermore this type of pan can be cleaned and re-used endlessly as the salt does not affect the metal. The cleaning procedure entailed sonication of the crucibles in deionised water for 30 minutes before been transfer to a beaker containing 5M hydrochloric acid which was sonicated for a further 30 minutes. The pans were then clean in water to remove the acid, and dried in oven at 80°C.

No loss in mass was observed after hundreds of tests. Just like the aluminium, the same procedure is utilised to fill up the crucibles with around 35.000 to 40.000 mg except that no crimping was required. In fact the pans were left open for all the tests. After producing the samples, the latter were melted on a hot-plate at 250°C - 280°C for 30 minutes. The reason behind the use of so much sample weight was to ensure that molten salt covered the whole bottom of the platinum pan.

After been left to cool, the outside of the crucibles were cleaned with damp paper to dissolve any salt that might have coated it. These particular types of pans were the most reliable in term of results and stability of the heat flow.

3.4.1.10 Sample Placement & Contact

The measurement of heat flow on the DSC is directly correlated to its placement on the sensor's surface. The impact of such slight change in placement might not affect direct measurement much. However Cp is derived from three heat flow curves, all of which are measured separately. If placement of one pan is incorrect, it will affect the overall calculated result (Fig. 35).

Correct Placement   Incorrect Placement
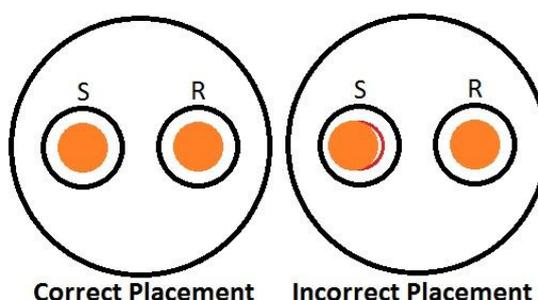
Figure 35: Schematic diagram of pan placement on DSC sensor. The picture on the left portray the perfect positioning of the DSC crucible (orange circle), whereby the flow of heat passes through the pan evenly. The right hand-side picture shows an imperfect placement leading to exposure of some of the sensor (red line) which causes an uneven flow of heat requiring the system to compensate for the irregular thermal flow.

Furthermore the contact between the two surfaces need to be optimized such that the bottom of the crucible is always flat and not curved as this would alter the flow of heat during the tests leading to errors in the measurements (Fig. 36).
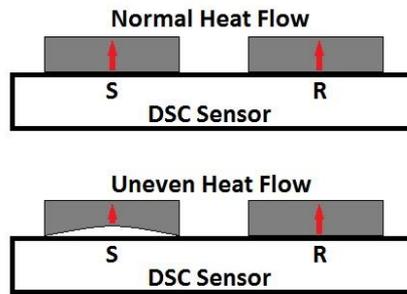
Figure 36: Contact area between the bottom of the crucibles and the DSC sensor.

Ensuring all of these precautions are met would prevent the user from damaging the equipment and would provide some assurances toward the quality of the data. As seen below (Fig. 37 & 38) variation in placement & contact can lead to massive difference in heat flow which would render Cp measurements almost impossible to achieve.
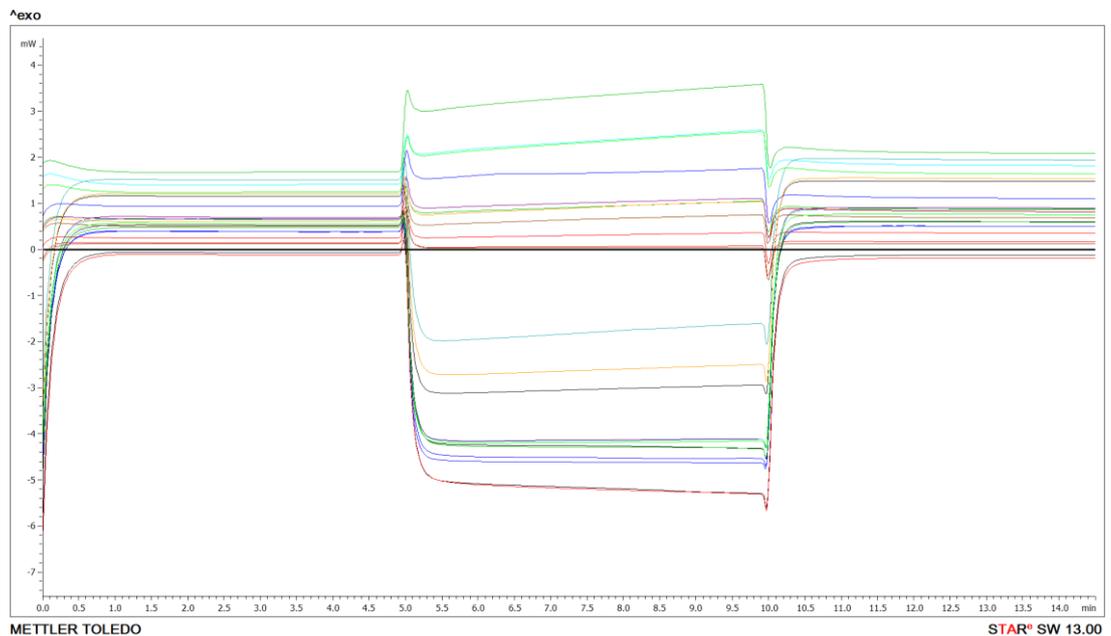
Figure 37: Effect of sample placement on heat flow curves for aluminium crucible (Positive curves – Blank, Negative Curves – Sapphire).
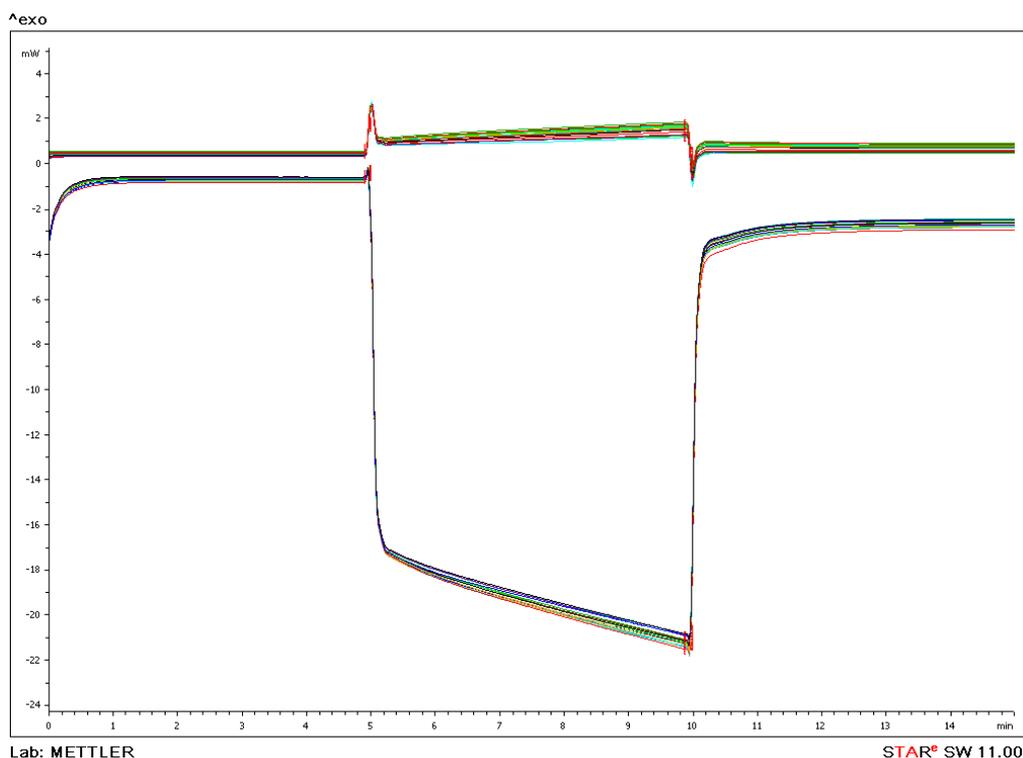
Figure 38: Effect of sample placement on heat flow curves for platinum crucible (Positive curves – Blank, Negative Curves – Sapphire).

The use of aluminium crucible was not recommended for these tests as the latter were easily deformed leading to uneven placement and/or contact with the sensor causing large variation in heat flow for blank crucible and sapphire curves. This was not the case when platinum pans were employed.

3.4.1.11 Sample Weighing

As it has been previously discussed, the Cp (J/[g*°C]) and enthalpy of change (J/g) are both directly dependent on the weight of the sample. The calculation for Cp also include the weight of the crucible as the latter might vary from one pan to the next and therefore needed to be taken into account. To obtain a high level of accuracy in the weighting process, an ultra-micro-balance from Mettler Toledo (UMX-2) was used. The latter

displayed an accuracy of 1.0 µg. Both samples and pans weight were recorded and used in the characterisation of the salts.

Figure 39: Ultra-micro-balance set on a granite block and encased in a plastic box to reduce the vibrations coming from the surrounding.

3.4.1.12 Thermal Cycles for DSC

The creation of a thermal cycle needs to be suited to what the user wants to achieve. In this research, the main point of interest was Cp but characteristics such as enthalpy and temperature at which transition from liquid to solid occurred were also analysed.

The value of Cp was tested between 250°C to 450°C with two different cycles where thermal cycle 1 was set with a heating rate of 10°C/min whilst thermal cycle 2 was programmed with a ramp of 40°C/min. Both used 5 minutes isothermal to surround each ramp.
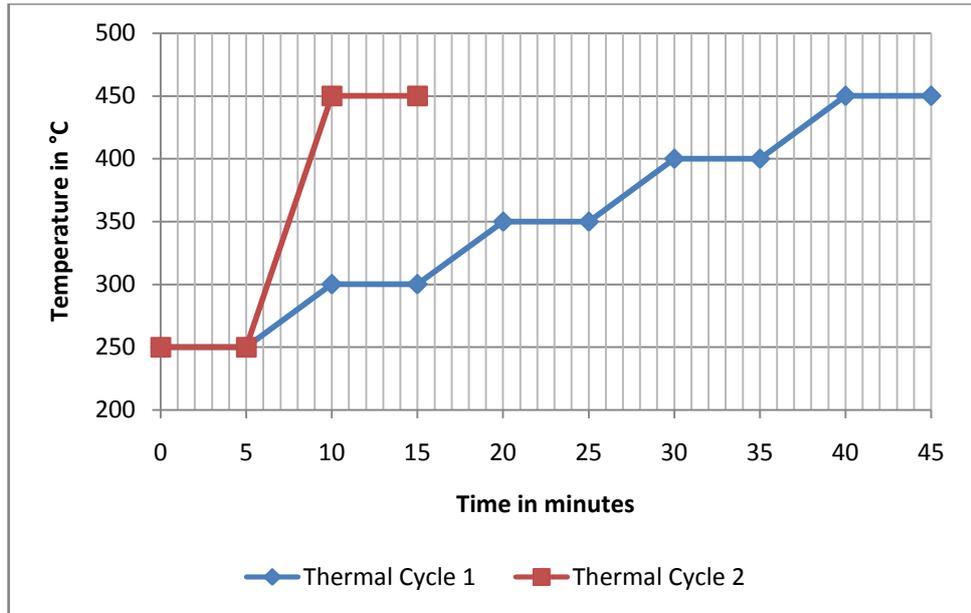
Figure 40: Thermal cycles used for Cp measurements.

Tests carried out on both cycles revealed that thermal cycle 2 was the best method to obtain reliable repeatable values. Whilst common guideline advised for heating rate of 10°C/min, it was revealed that the faster heating rate did provide accurate and reproducible data.

The measurement of melting/crystallisation and enthalpy of change of nitrate salt was analysed using the following cycle (Fig. 41).
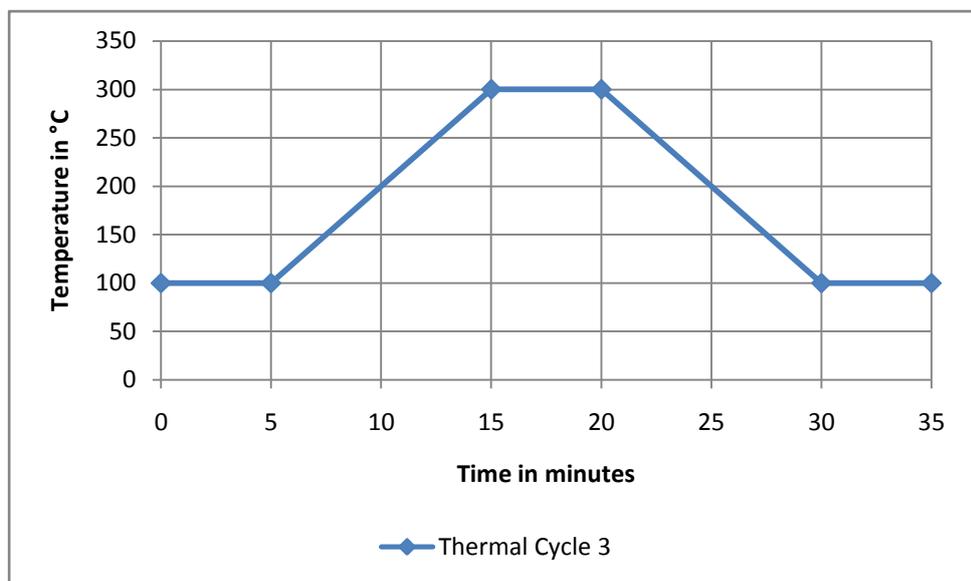
Figure 41: Thermal cycle for enthalpy (J/g) and transition (°C) tests.

3.4.2 Thermo-gravimetric Analyser: Principles & Methodology

3.4.2.1 Introduction to TGA

The primary function of this apparatus is to measure change in mass as a function of either temperature (with constant heating rate usually 10°C/minute) or time (constant temperature) in a controlled atmosphere. Many changes whether physical or chemical such as sublimation, evaporation, absorption, adsorption, oxidation or reduction will affect the weight of a sample either positively or negatively.
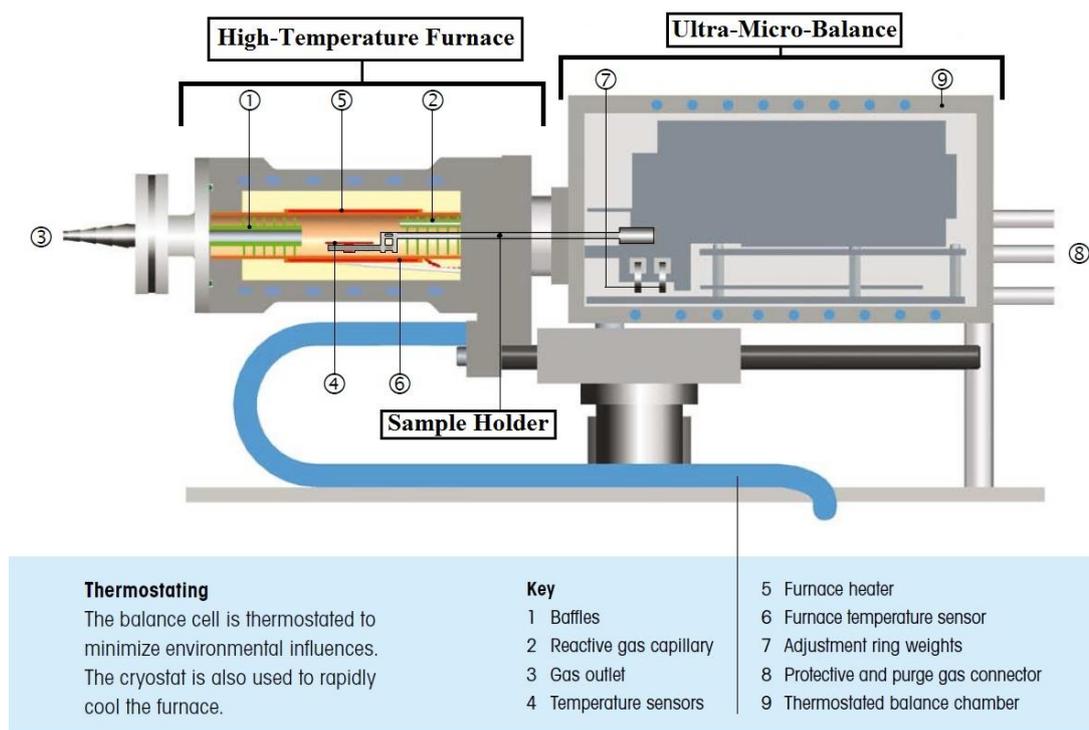
Figure 42: Schematic diagram of the TGA from Mettler Toledo.

Operating at temperature ranging from 25°C to 1100°C, the furnace is opened, exposing the sample holder where the crucible is placed onto. Prior to sample insertion, the pans and sample weights are recorded on the Ultra-

micro-balance to verify that there are no discrepancies in weight between the two equipments (Resolution of 1.0 μg). The advantage of such system lays in the fact that measurement can be done up to 1100°C which is not the case of a normal DSC system as it is restricted to 700°C. However the precision obtained with a single DSC system surpass that of a combined DSC/TGA.

3.4.2.2   Balance and Heat Flow Calibration

The instrument's ultra-micro-balance contains two internal weights which automatically calibrates the system when it is turned on. External calibration can also be done with standard weight obtained from Mettler Toledo but this step was not carried out as both ultra-micro-balances gave similar weight reading when weighting the samples.

Heat flow calibration is done through a similar inbuilt system to that of the DSC. However the calibration of this system requires the testing of 4 metals (Indium, Zinc, Aluminium and Gold) that span the entire range of the equipment.

Table 4: TGA/DSC Calibration Metals

Material	**Melting Range**	*Melting Temperature*	**Heat of Fusion Range**	*Heat of Fusion*
	°C	*°C*	**J/g**	*J/g*
Indium	**155.1 - 158.1 (156.6°C)**	*157.13*	**24.225 - 32.775 (28.5 J/g)**	*30.04*
Zinc	**417.5 - 421.5 (419.5°C)**	*420.03*	**91.375 - 123.625 (107.5 J/g)**	*113.53*
Aluminium	**657.8 - 662.8 (660.3°C)**	*660.53*	**317.6 - 476.4 (397.0 J/g)**	*386.11*
Gold	**1061.2 - 1067.2 (1064.2°C)**	*1065.06*	**50.96 - 76.44 (63.7 J/g)**	*67.79*

3.4.2.3 Crucible Type and Sample Preparation

The choice of crucible needed to be appropriate to the experiment been conducted with the TGA. In most cases, alumina samples would be used as this material can easily withstand the maximum temperature (1100°C). However, it was discovered that the porosity of the alumina crucible led to the infiltration of salt through to the sample holder's surface. This led to the inability to remove the pan due to crystallisation occurring between the two surfaces. To dislodge the crucible, the whole sample holder plus the crucible were removed and placed in deionised water to dissolve the salt. To prevent this, platinum crucibles were used as they can withstand high temperature (>1100°C) and are very resistant to corrosion. Furthermore they are not porous.

Thermal stability tests of the salt were conducted by using 10.000 to 15.000 mg of sample loaded inside the platinum pans. The crucible were placed onto the carousel and the experiment were programmed. The thermal cycle used was as followed:

- Isothermal at 50°C for 20 minutes
- Dynamic from 50°C to 1000°C at 10°C/min

3.4.3 Scanning Electron Microscopy

This system (LEO 1530) was used to analyse the crystallised molten salt surface and investigate whether or not nano-particles were present to see how the latter adhered to the crystal's surface. Using an electron beam, SEM analysis allows the user to reach resolution within the nano-meters range. Samples tested on the DSC using aluminium pans were cut open and stuck onto an SEM stub. The latter was usually coated with a platinum layer of 5 nm before analysis was to start. Due to the inability to control size and shape of the sample, most analyses were carried out on uneven surface.
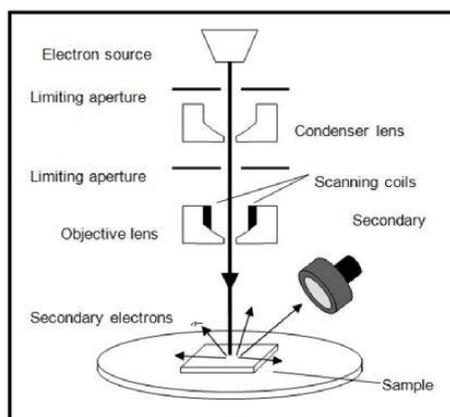
Figure 43: Schematic Diagram of SEM

3.4.4 Rheometer

3.4.4.1 Introduction

This piece of equipment measures the viscosity of fluid and how stress and strain affect the material been tested. Coined 'rheology' in the 1920s, this term which was inspired by a Greek quotation 'panta rhei' meaning everything flow, define the study of the flow of matter. The easiest way to describe rheological properties is through the parallel plate model [99], where the liquid can be pictured as an infinitesimal amount of layers stacked on top of one another, analogous to that of a stacked deck of cards. In a rheometer, the force is rotationally (Fig. 44 – b & c) applied rather than axially (Fig. 44 – a). Still, the same rules govern rotational forces as it will also shear the liquid in a laminar fashion as exemplified below:
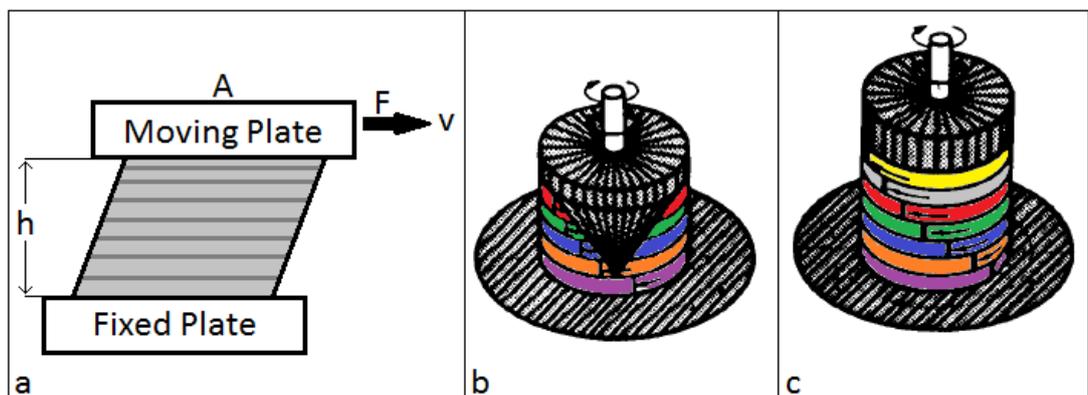
Figure 44: a) Represents Parallel Plate Model – b & c) Laminar flow of sheared liquid represented by different coloured bands [100]. Two different setups are pictured, cone on plate (b) and plate on plate (c).

The measurement of viscosity is based upon the shear rate and shear stress such that:

- Shear rate is defined as the velocity of rotation divided by the gap size and is measured in s^{-1}.

$$Υ(s^{-1}) = v\ (m.s^{-1})\ /\ h\ (m)$$

- Shear stress is the force required by the instrument to keep a define shear rate. The latter depend on the area of contact with the fluid and it is measured in Pa or N/m^2.

$$τ(Pa) = F\ (N)\ /\ A\ (m^2)$$

- Viscosity relates to the ability of a liquid to resist a gradual deformation due to the application of stress on its surface. The greater the viscosity is, the larger the resistance to stress becomes. Measured in Pa.s, it is obtained through the following equation:

$$η\ (Pa.s) = τ(Pa)\ /\ Υ(s^{-1})$$
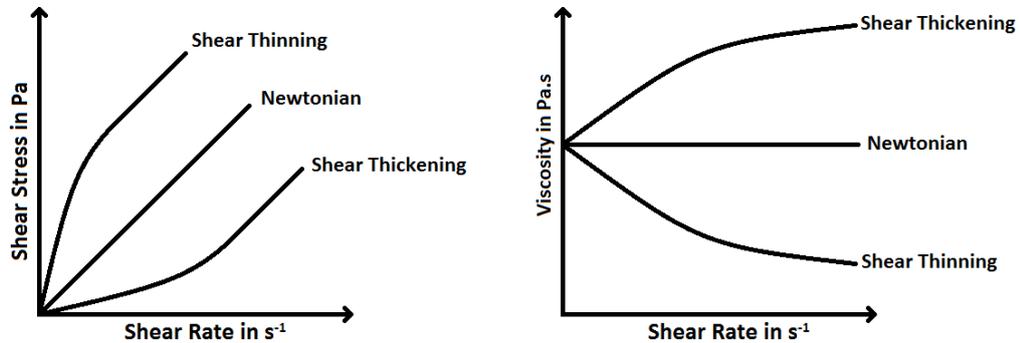
Figure 45: Graph showing how the shear rate affects the Newtonian and Non-Newtonian behaviour of fluids in relation to both shear stress and viscosity.

Fluids are generally classified into two categories: Newtonian or Non-Newtonian fluid. The former is usually defined by a single coefficient of viscosity at a set temperature remaining constant with increasing shear rate. The latter is affected by shear rate at a set temperature such that viscosity

will either increase or decrease causing either shear-thinning or shear-thickening of the material in question.

3.4.4.2 Cone or Flat Plate Setup

The geometry of the setup will affect the measurement as the shear stress is related to the area of contact. In a plate-plate system, the shear rate is not constant across the radius such that the edge of the plate experiences maximum velocity whilst the centre displays a velocity of zero. Furthermore the gap can be altered and depends on the material been tested. In a cone-plate, the shear rate is uniform across the radius and the gap is pre-set to a certain standard which depend on the manufacturer. Both system use small volume and are easy to clean, but the fact that it was not known how shear rate would affect the material favoured the cone and plate model. Calibration test with plate-plate setup were not convincing and determining a gap size which provided accurate data was difficult to achieve hence this type of setup was discarded.

3.4.4.3 Setup

Viscosity measurements were carried out with an Anton Paar 'Physica MCR 301 TruGap Ready' fitted with a furnace and a 'TC30' temperature controller unit (Accurate to 0.1°C). The nature of the sample tested required high temperature to melt the sample into its liquid form before testing could begin. However prior to any measurements been made, the rheometer had to be tested with standard both at low and high temperature to ensure that both

the instrument and this particular setup utilized were calibrated and providing the correct results.

Figure 46: Rheometer setup used to measure viscosity of molten salt. The left picture shows the open two halves of the furnace, with in the middle, either a 65 or 50 mm stainless steel plate onto which the sample is placed with an over-hanging stainless steel cone of 50 mm diameter and 1° angle. The right picture is the setup of the equipment once the furnace is closed.

Using water, standard oil and published viscosity data from KNO_3, the rheometer was checked to ensure that it was calibrated before any of the tests were started. As a cone and plate setup was utilized, the gap between the plate and the flat tip of the cone was pre-set at 0.098 mm. In order to achieve the test, it is crucial to have the correct amount of liquid in the gap such that the whole area of the cone (just the underside) is used, however, too much or too little liquid would lead to a greater or smaller area of contact, increasing or decreasing the value of viscosity providing misleading information.
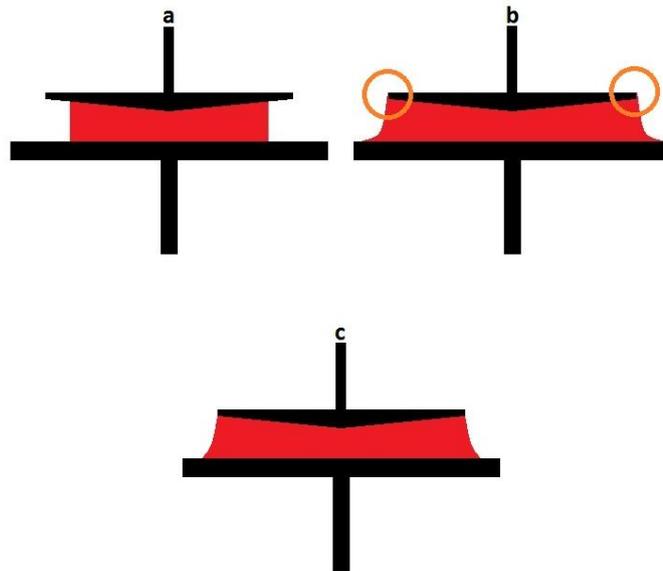
Figure 47: Schematic diagram of the area of contact between the liquid and the cone & plate setup. Diagram a) has too little fluid between the plate & cone, whilst b) has too much such that the edge of the cone is taken into account (orange circles). Only c) would provide the correct value as only the underside of the cone is utilized for the measurements.

The preset volume required is 0.57 ml which is the equivalent of 0.57 cm^3 providing the density is 1.00 g/cm^3. Therefore, if the density of the liquid is known, it is possible to back-calculate the amount needed. The calibration with the mentioned above substances will provide the user with the assurance that the correct volume/amount is used.

3.4.4.4 Calibration Tests : Deionised Water

The calibration with water was done at four different temperatures (20, 30, 50 & 70°C) and each temperature was tested at least 3 times to obtain an average value using the following setting:

- − Pre-shearing at shear-rate 200 s^{-1} during 1 minute to homogenise and control temperature of the sample

- − Shear-rate from 200 to 1000 s^{-1}

- − Sweep mode line

- − 50 points

- − 5 seconds duration point
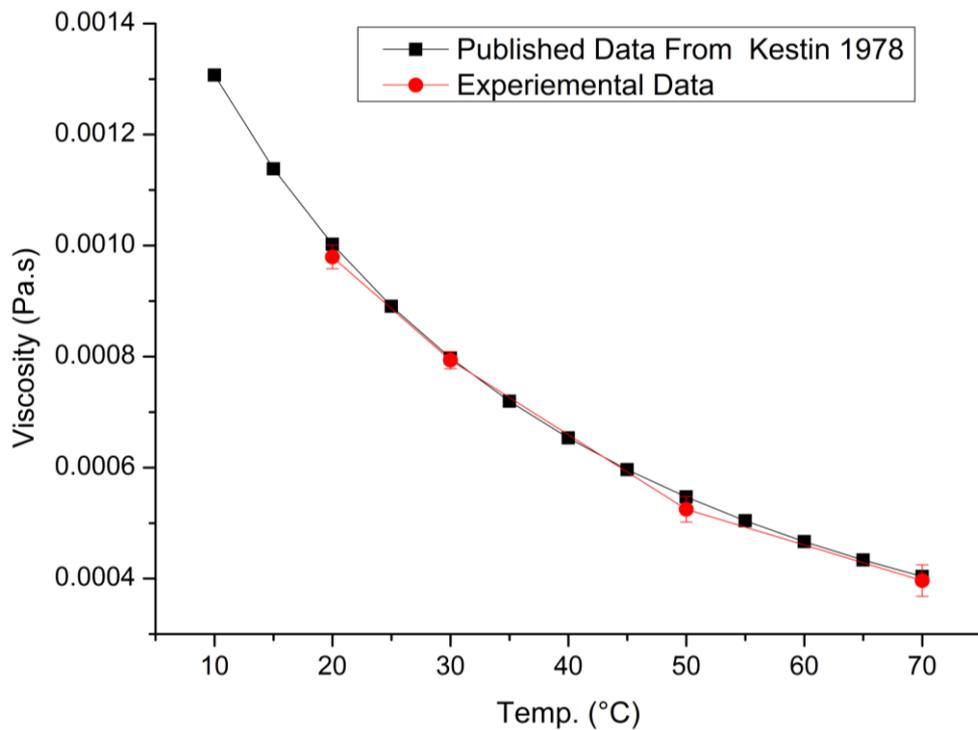
Figure 48: Calibration of Rheometer using 0.57 ml of deionised water [101]. The obtained values are significantly accurate (≤ 3.0%)
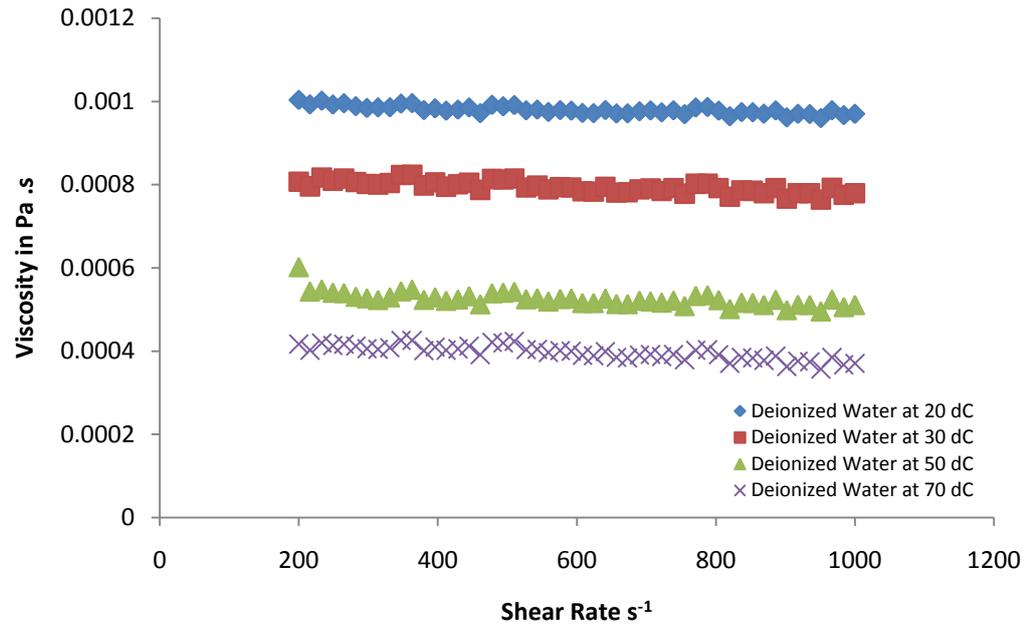
Figure 49: Viscosity against shear rate shows that, as expected deionised water behave like a Newtonian liquid [101].

3.4.4.5   Calibration Tests: Calibration Oil

The calibration with Rheotek oil was done using the following setting:

−   Shear-rate from 10 to 1000 s^{-1}

−   Exponential increase in shear rate

−   10 point per decades

−   21 points

−   20 seconds duration point
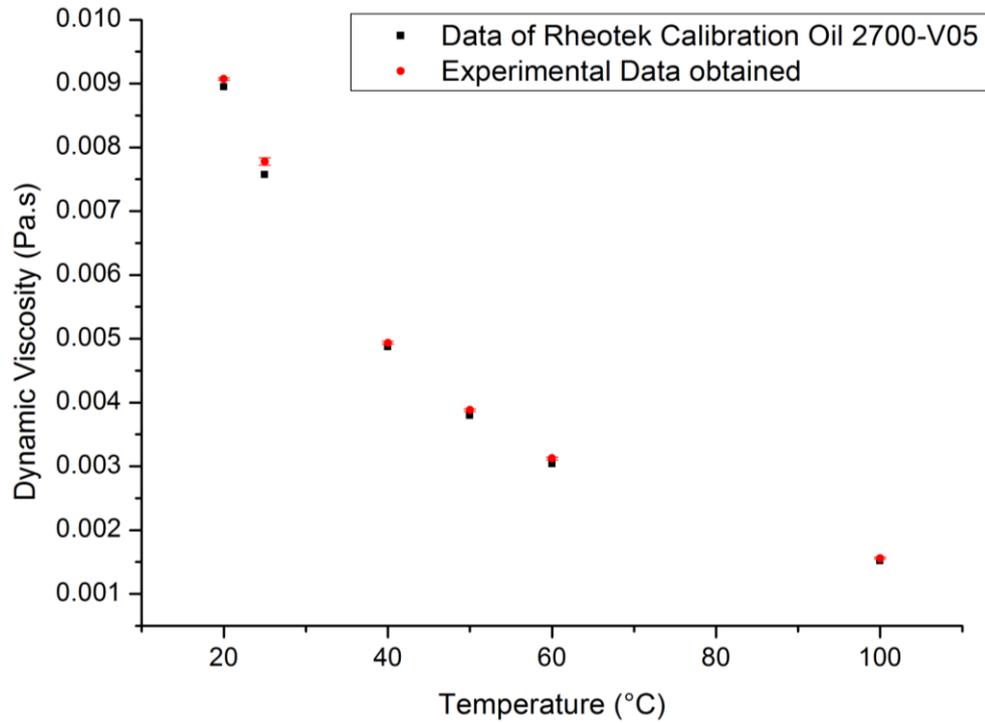
Figure 50: Calibration of Rheometer using Rheotek Calibration Oil 2700-V05 [102]. The obtained values are within 3%.
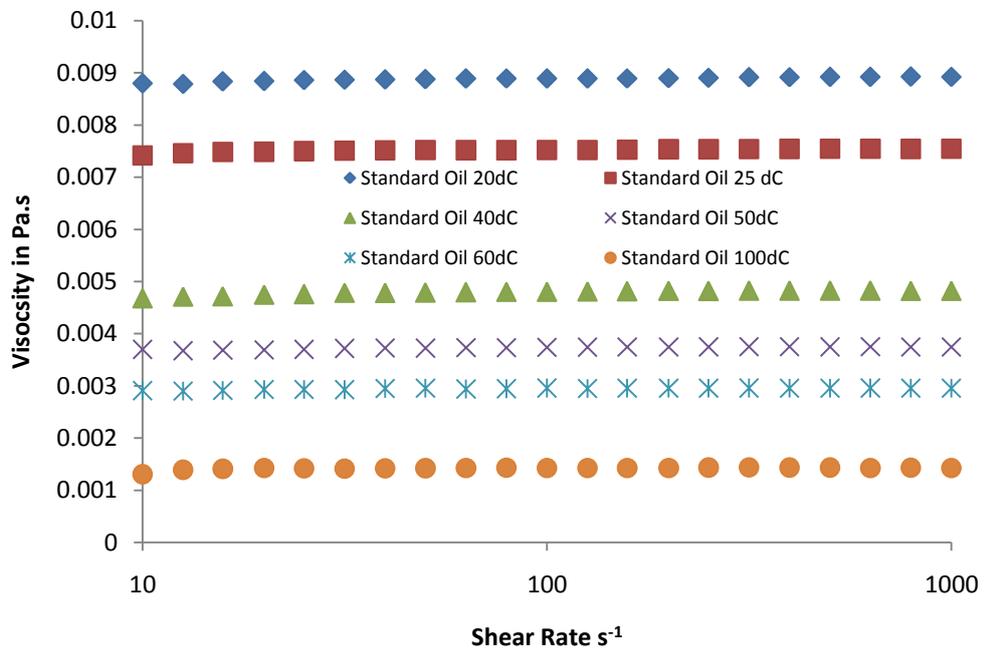
Figure 51: Viscosity versus shear rate demonstrate the Newtonian character of the calibration fluid used.

3.4.4.6 Calibration Tests: Potassium Nitrate

Finally calibration at high temperature was carried out to ensure that the method utilize was functioning at high temperature. As the density of potassium nitrate is 2.11 g/cm^3, the amount of solid used was around 1.20 grams.
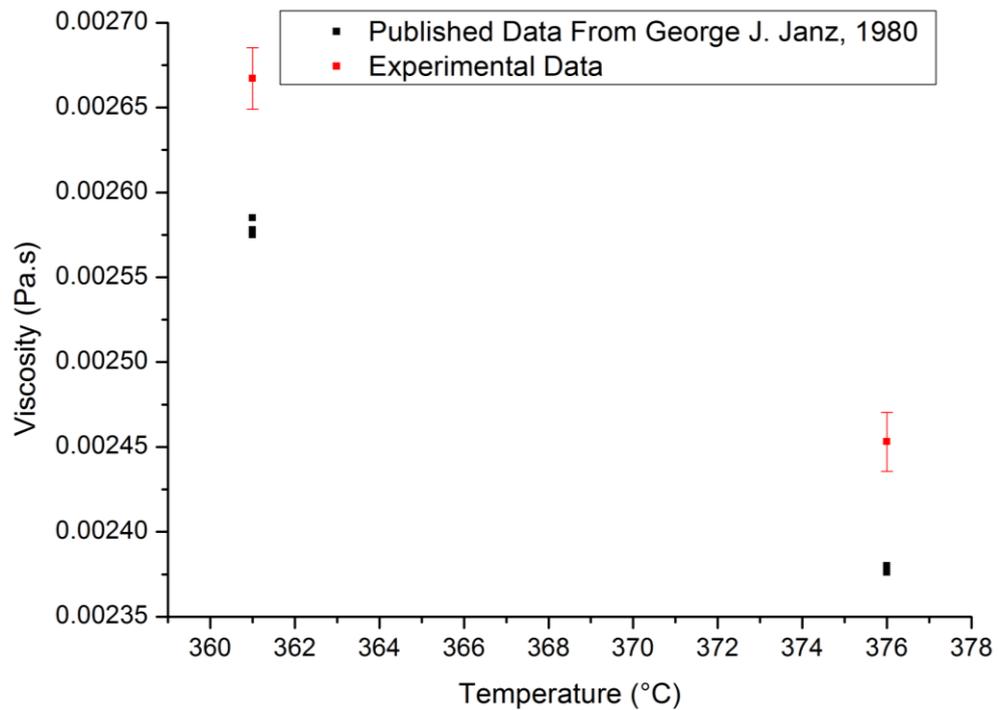
Figure 52: Calibration of Rheometer using KNO$_3$ data from George J. Janz, 1980 published data which shows that the experimental results are within 4.0% of the published data [103]. The following tests were carried out at a constant shear rate of 200 rpm.

3.4.4.7. Sample Preparation for Rheological Tests

1.07 grams of powdered salt (density of $NaNO_3/KNO_3$ - 60/40, $\approx$1.89 g/cm^3) was placed onto the plate. The furnace was closed, brought to 250°C, the cone was lowered to measuring height (0.98 mm) and the tests were started.

The following setting were used for the tests:

- − Shear-rate cycle from 100 to 1000 s^{-1} – 1000 to 100 s^{-1}

- − Cycle Repeated 10 times.

- − Exponential increase & decrease in shear rate

- − 10 point per decades

- − 11 points

- − 20 seconds duration point

The whole rheometer was programmed to carry a number of tests at set temperature ranging from 250°C to 450°C.

Chapter 4 Design and Production of Stability Rigs

This chapter describes how and why the stability rigs were created.

4.1   Stability Rigs

In order to study the effect of physical dispersion of nano-particles in liquid salt, it was necessary to maintain a constant temperature above that of the melting point. To achieve this, a system which could hold a relatively large amount of salt was designed and built, such that different type of physical dispersion could be tested. Samples were collected at different period of time to try and understand if and how Cp varied, and whether or not sedimentation affected the salt.

Two basic containers were designed out of stainless steel 316 which could hold 1.6 and 1.1 kilograms of molten salt given that at 300°C, Solar Salt (60 wt. % $NaNO_3$ – 40 wt. % KNO_3) displays a density of 1.899 g/cm^3. All the systems would be held at 300°C for at least 744 hours which equates to a month of operation. Samples would be taken regularly and tested to define how Cp was varying against time. Made of three basic parts soldered together, the production of these tanks were outsourced to an engineering company.

4.2 Schematic Design of the 1.6 kg container:
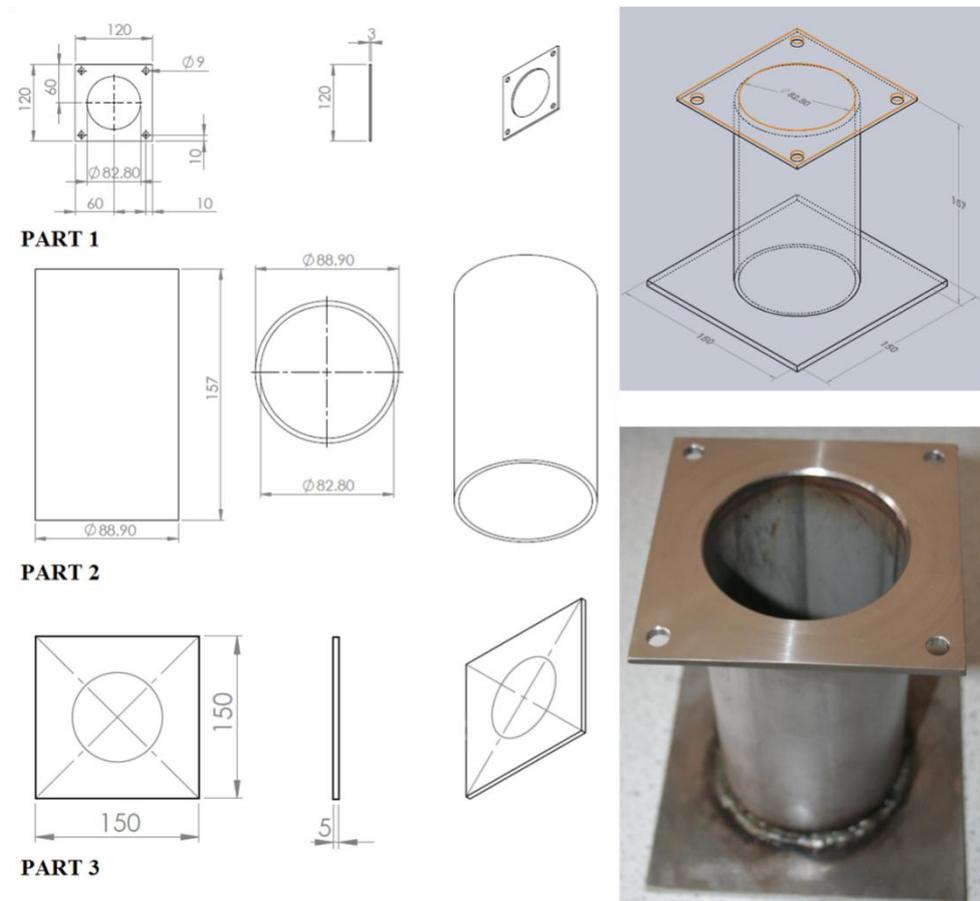
Figure 53: The left-hand side represents the dimensions of each of the parts required to produce the tank shown as a 3D sketch on the top-right hand side with the fully build version seen below it.

Four rigs were built using this particular design:

- Static Rig with Pure Salt (100% Solar Salt) (Negative control)

- Static Rig with Mixture (Positive control)

- Stirring Rig

- Bubbling Rig

The top plate for each rig was altered to accommodate the different method of dispersion utilized.
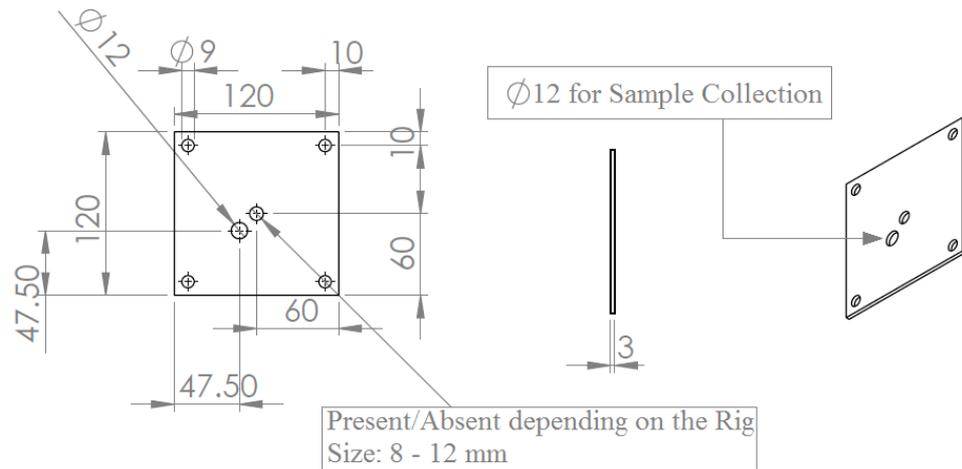
Figure 54: Schematic diagram of the top-plate.

In both static rigs, the centre hole was removed as no dispersion of any kind was done. Both of these rigs provided the user with a positive and negative control to compare the other results to.

For the stirring rig, an overhead low shear rate mixer was used with a shaft and an axial top-to-bottom impeller blade to provide turbulences (Dimension of the blade are quotes on Figure 55). The centre hole had to be enlarged to ensure that the shaft did not come into contact with the top plate so as to prevent any damage over time.

The bubbling rig had Swagelok fitting to hold a 3.00 mm outer diameter tube. The centre hole was threaded to fix the whole system in place. Unlike the photo showed (Fig. 56), the tube was not straight but coiled in shape to allow the gas to warm up as it descended into the bottom piece where the bubbles were expelled.
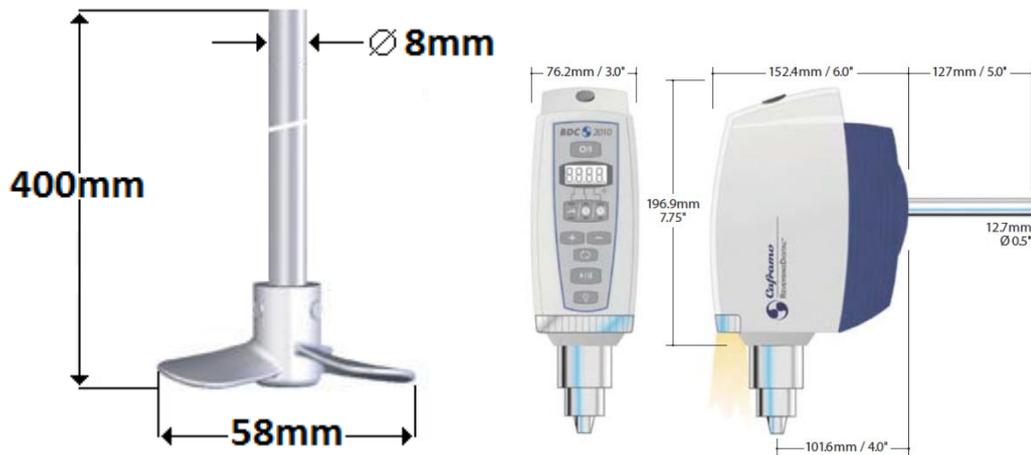
Figure 55: Left: Dimension of the impeller blade used. Right: Overhead Stirrer BDC2010 from Caframo utilized in the stirring rig.
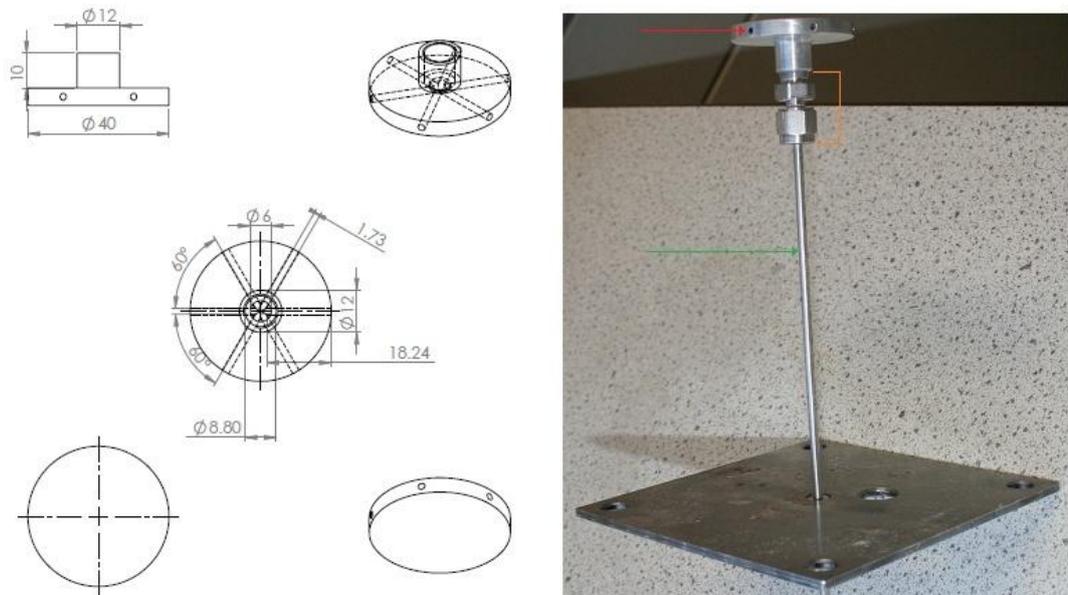
Figure 56: Left: Diagram of the bubbling piece which is centred at the bottom of the tank. Right: Bubbling piece (Red Arrow) connected to 3.0 mm outer diameter tube (Green Arrow) through Swagelok fitting (Orange Line).

4.3   Schematic Diagram for 1.1 kg container:

This system was designed to produce turbulence in the fluid by forcing it to go through holes located in the centrepiece of the moving cylinder.
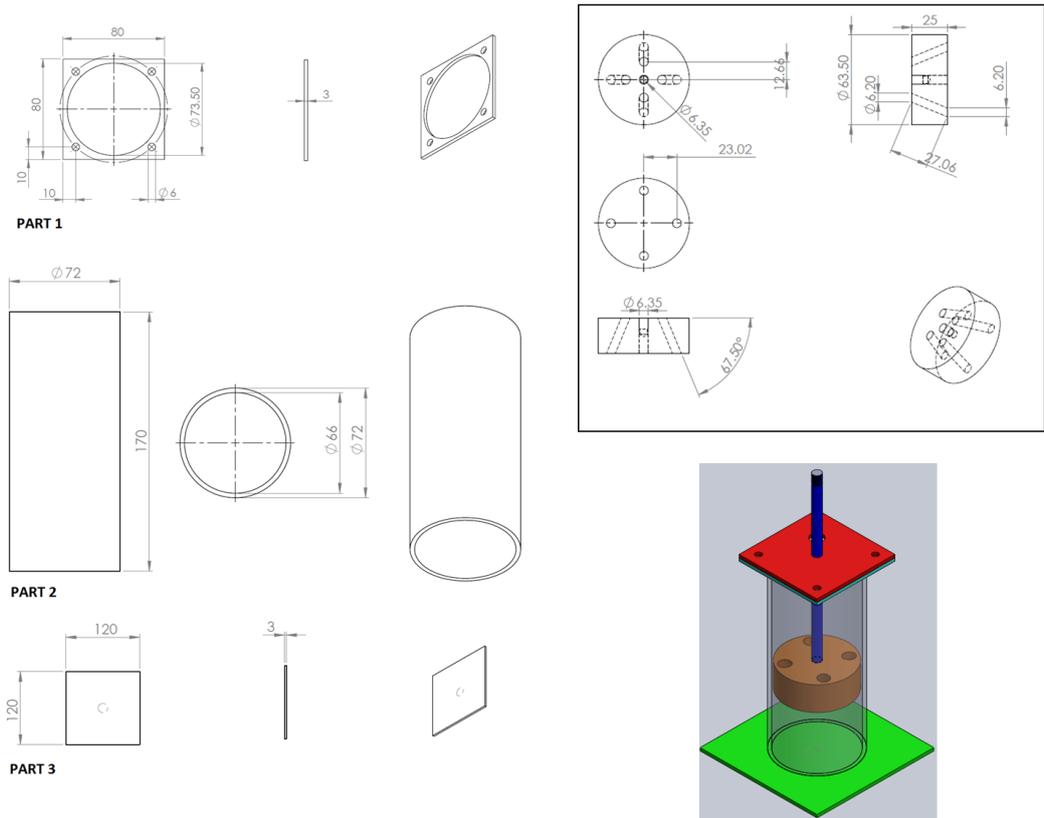
Figure 57: Left: Dimension of each of the three parts soldered together. Top-Right: Dimension of the moving centre-piece providing turbulence in the molten fluid. Bottom-Right: Moving centre-piece in orange is connected to a shaft (blue) which is itself linked to a pneumatic piston providing an up and down motion.

4.4   Building, Challenges and Alteration

After receiving the soldered rigs, two thermocouples were attached on opposite side of the stainless steel containers. Located at the bottom of the crucible, these thermocouples measured the temperature of outside wall with one of them feeding information to the temperature controller unit whilst the other was in charge of limit so as to ensure that the system would automatically shut down above a defined threshold.

The reason for not measuring the temperature directly in the molten salt was that their corrosive nature would have damaged the sensor over time causing the experiment to stop as any loss in sensor led to an automatic shut down of the system.
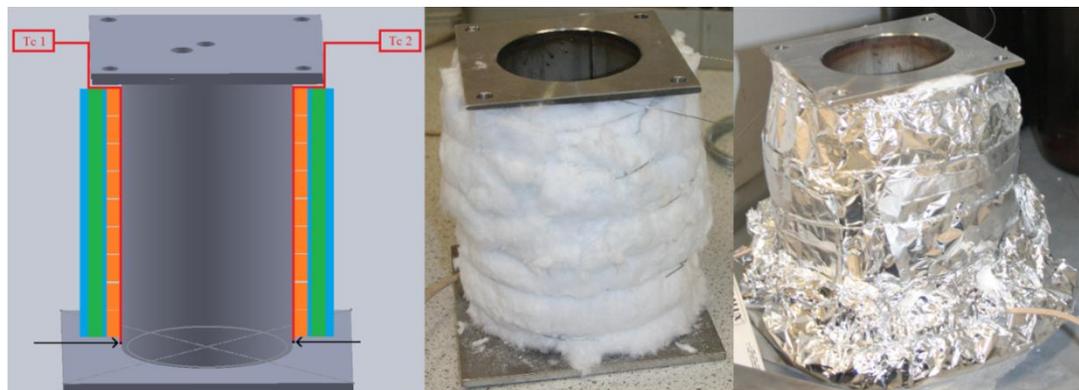
Figure 58: Thermocouples 1 & 2 (Tc 1 & 2 Red box) are attached to wall's surface of the rig and measure the temperature of the container wall at the bottom (Black Arrow). The orange layer represents the flexible heater band which is in direct contact with the stainless steel wall whilst the blue and green bands are the aluminium foil and the insulating wool respectively.

Once the thermocouples were in place, a flexible heater band from Omega was coiled around the whole surface of the tube. After fixing the heater

band, aluminium foil was wrapped on top of the heater band so as to allow heat to escape to prevent the formation of hotspots which would damage the heater. Finally, insulating wool was used to reduce heat loss followed by another layer of aluminium foil as seen on Figure 58.

Upon completion of the build, the rig was connected to power unit which was itself controlled by a lab-view program. In these tests the aim was to roughly stabilise the temperature at 300°C. Because each rigs was build manually, the amount of insulation and the placement of the thermocouple were slightly different which led to different power output been needed to maintain a constant temperature. This was achieved by manually controlling the power output of each rig. Once set to a certain power, it was left as such during the entire length of the tests.

Preliminary empty tests lasting at least 48 hours were carried out to ensure that the heater could maintain that temperature without failing. On a couple of occasions, hotspot formation led to the dismantling and re-building of the rigs. Following on, 600 grams of salt were inserted inside the rigs and brought up to temperature. After leaving the rigs for a couple of hours, loss in power was noticed. This was caused by badly soldered joins leading to salt leaking from the bottom of the rig, and destroying to heater band causing it to short-circuit. Thus the rigs were sent back.
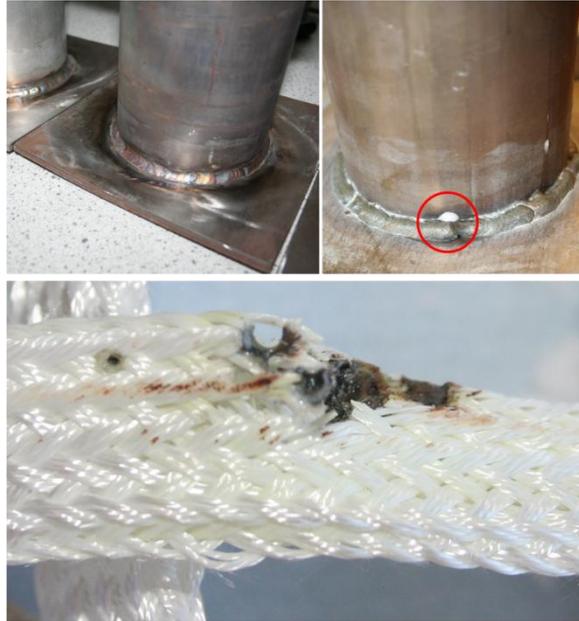
Figure 59: Bottom Picture: Heater band damaged through contact with molten salt. Top-left: Newly soldered container. Top-Right: Badly soldered rig with salt leaking through.

After receiving back the container which had been re-soldered, water was used to test the sealing over a couple of days. Following on, the salt was added to each rig and the tests were started.

4.5   Sample Collection

The collection of samples had to be done during the liquid phase and was achieved by rapidly dipping a cold metal bar inside the hot fluid allowing it to crystallize on the surface. Leaving the bar too long would cause it to warm up above the melting point of the liquid which then made the task impossible. The collected sample was then left at room temperature to cool down before a photography of the obtained crystallised salt was taken.
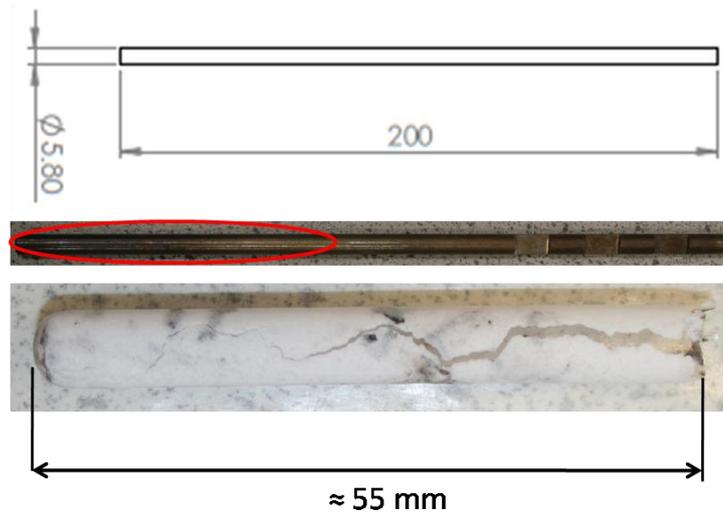
Figure 60: Top drawing shows the schematic diagram of the rod which is 200 mm long and 5.8 mm in diameter. The bottom picture displays a collected sample which is roughly 55 mm in length and obtained by dipping the metal rod (red circle) in the container until it touch the bottom.

Collecting sample in this way was quick, efficient and safe allowing the procedure to be repeated many times.

Chapter 5 Results & Discussion: Salt Characterisation without Additives

This chapter provides the user with the data obtained on the characterization of both single salts sodium & potassium nitrate as well as its eutectic mixture (60 wt% $NaNO_3$ + 40 wt% KNO_3).

5.1 Nitrate Salt Characterisation:

DSC tests carried out on sodium and potassium nitrate displayed melting point of 308.0°C and 336°C respectively with heat of fusion of 172.84 J/g for sodium nitrate and 95.55 J/g for potassium nitrate [104-106]. Both salts showed very little overcooling during crystallisation phase and the curves obtained over many heating/cooling cycles were sharp, accurate and overlapping. This validated the purity of both compound used.

Table 5: Melting and enthalpy of both salts used in the production of the eutectic mixture

	$NaNO_3$			
	Melting Point	Enthalpy of Melting	Crystallisation Point	Enthalpy of Crystallisation
	°C	J/g	°C	J/g
Mean	308.01	172.84	303.66	171.11
St.dev	0.99	2.10	0.24	0.30
	KNO_3			
	Melting Point	Enthalpy of Melting	Crystallisation Point	Enthalpy of Crystallisation
	°C	J/g	°C	J/g
Mean	336.03	95.55	332.08	96.29
St.dev	0.76	0.58	0.29	0.53

The specific heat capacities of each salt were then measured individually and results obtained revealed similar measurement for the potassium nitrate (1.34 J/[g*°C] at 386°C) with Carling 1982 (1.38 J/[g*°C] at 386°C) and Takahashi 1988 (1.39 J/[g*°C] at 386°C) [106, 107]. However the results differ substantially when it came to the sodium nitrate with variation of around 10.0 % between experimental and literature data.
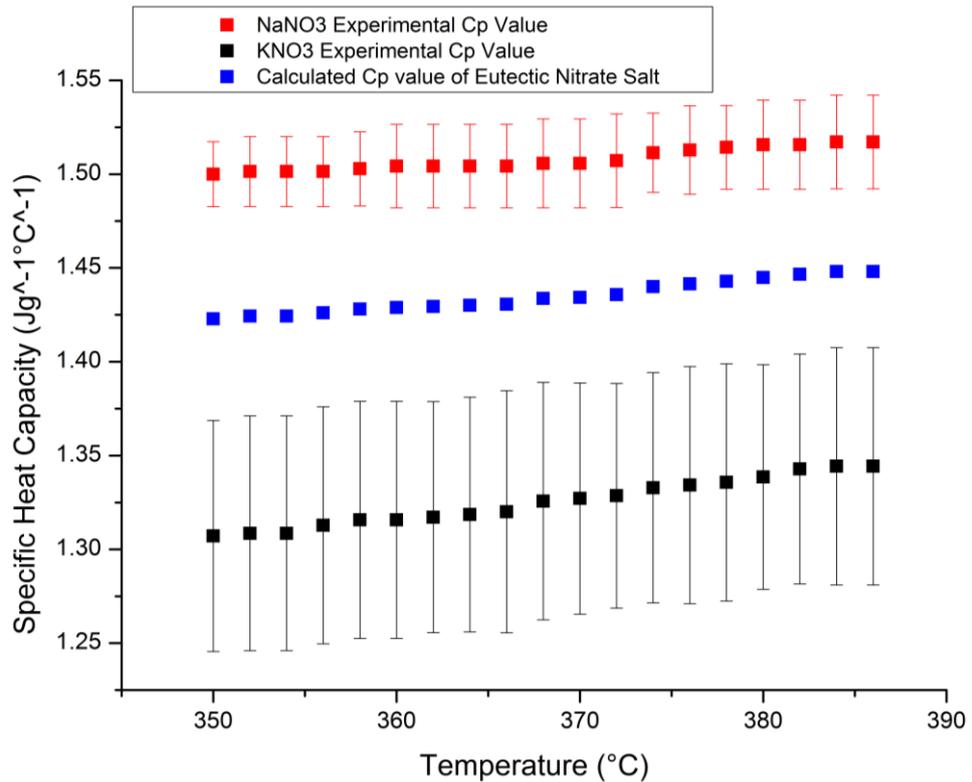
Figure 61: Specific heat capacity of each single salt value for both sodium (Red) and potassium (Black) nitrate were measured whilst the theoretical value of the binary mixture (60 wt. % NaNO$_3$& 40 wt. % KNO$_3$) was calculated (Blue).

With standard deviation below 2.0% for NaNO$_3$, and specific heat capacity of sapphire been within appropriate limit (Fig.78), this relatively large deviation (7 - 10%) in results was difficult to comprehend but difference in experimental setup could partly explain this disparity, and whilst analytical techniques have greatly evolved since the publication of both of these paper (Carling, 1982 & Takahashi 1988), there are still existing variations in the specific heat capacity of solar salt as mentioned by Bauer, 2013 [108].

5.2   Specific Heat Capacity of Binary Nitrate Salt

The specific heat capacity of nitrate salt mixtures (60 wt. % $NaNO_3$ & 40 wt. % KNO_3) is still subjected to major differences in term of the results obtained as showed by Figure 62 & 63. The data gathered from the DSC showed value varying from 1.40 J/ [g*°C] at 260°C to around 1.44 J/ [g*°C] at 440°C with standard deviation obtained below 2% for 11 different samples tested at least 4 times each (46 Tests in total). The closest results obtained from recent literature are those of Dubba, 2013 which were almost similar at 260°C but varied by 5.5 % at 440°C [15]. However results from Lu, 2013 were completely different with increase in Cp varying from 10.0 % to 13.0 % [16]. With varied reported numbers (Figure 62 & 63), it is difficult judge the precision of the data gathered as there are no validated results within the scientific community for this type of compound. However, the precision of the sapphire results indicated that the method of measurement and the calibration of the equipment were correctly done. Indeed the measured (7 samples each tested 3 times) specific heat capacity of the sapphire was within ±0.3% of the actual reference data (Figure 64). As the latter is directly related to the measurement of Cp, it implied that the calculations of the samples' Cp were done appropriately. This was further back-up by the close proximity between the calculated data obtained from the single nitrate salt Cp's measurement to that of the gathered data displayed in figure 65.

It was crucial to ensure the reliability of this data as it laid down the foundation of this thesis which was to evaluate whether or not the addition of nano-particles would enhance this thermal characteristic. Other characterisation works were carried out to set baseline against which nitrate

mixtures with additives would be compared to and to try to fully understand

the basic behaviour of this binary salt blend.
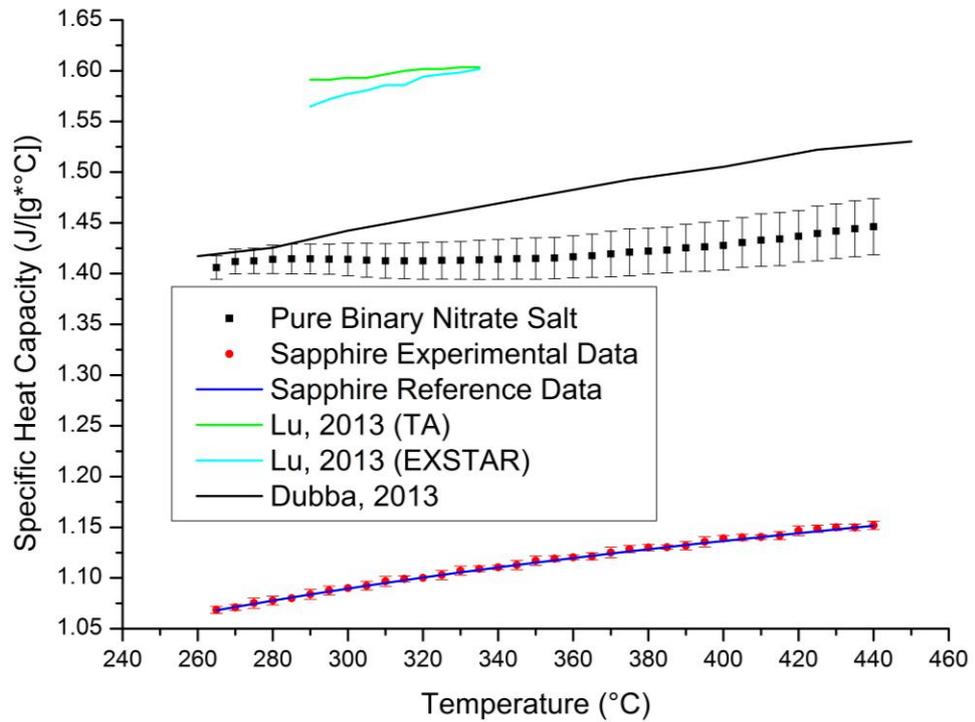
Figure 62: Specific Heat Capacity of binary combination of nitrate salts (60 wt. % NaNO$_3$ & 40 wt. % KNO$_3$) (Black Square) against results gather from recent literature data [15, 16]. The average specific heat capacity of sapphire (Red Circle) against that of literature value is also showed [109].
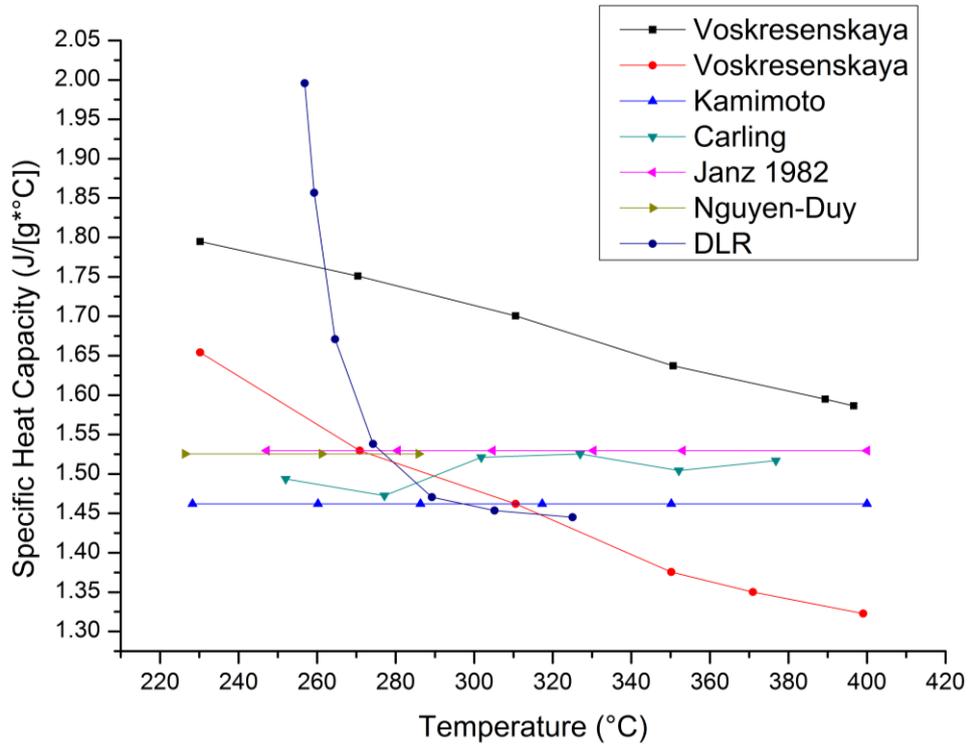
Figure 63: Variation of the specific heat capacity of binary nitrate salt (60 wt. % NaNO$_3$ & 40 wt. % KNO$_3$) found in the literature [110].
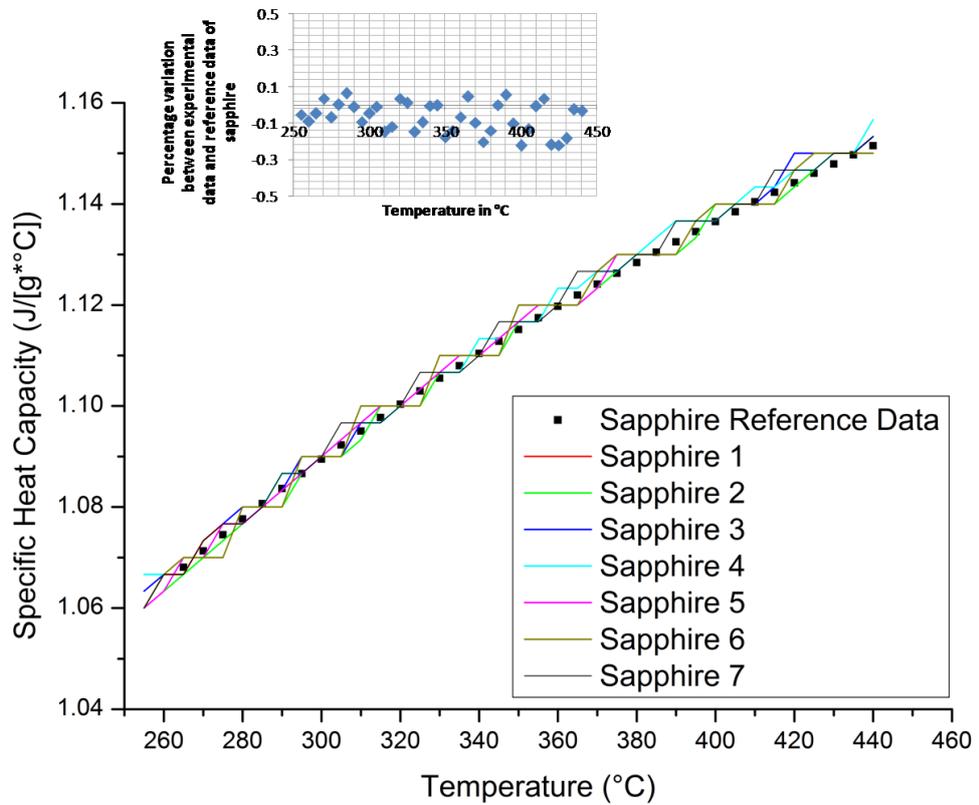
Figure 64: Composite diagram showing the specific heat capacity of sapphire reference against measured data with top left drawing displaying the percentage difference between the two [109].
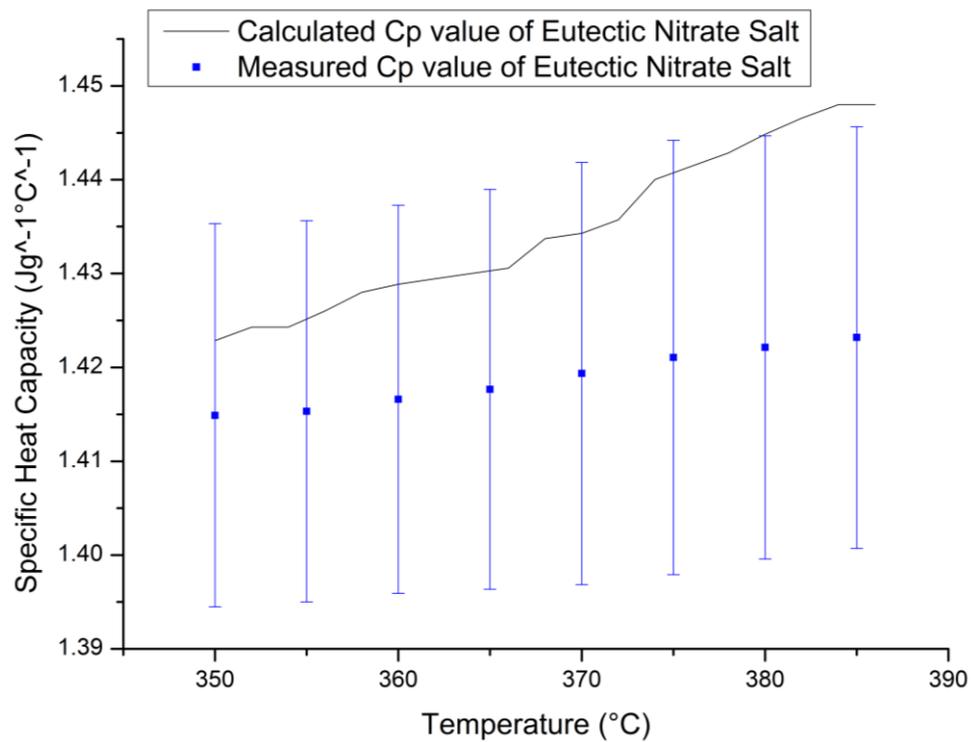
Figure 65: Calculated vs. Measured Specific Heat Capacity

5.3   Enthalpy of Change of Binary Nitrate Salt

The results obtained agree with previous literatures placing the enthalpy of change around 100 J/g and the melting point at ≈222°C [12, 111-113]. With only vague mention of the basic thermal characteristics of the salt mixture, no recent papers were found investigating in detail the properties of this binary mixture. The analysis of this salt mixture demonstrated a certain stability in its ability to melt and crystallise repeatedly with similar enthalpy of changes measured (97.06 J/g & 96.76 J/g, Fig. 66) and very little over-cooling taking place (4.48°C between melting and crystallisation). The spread of data (<2.0%) and its agreement with literature further reinforced the validity of these results which were both precise and accurate.
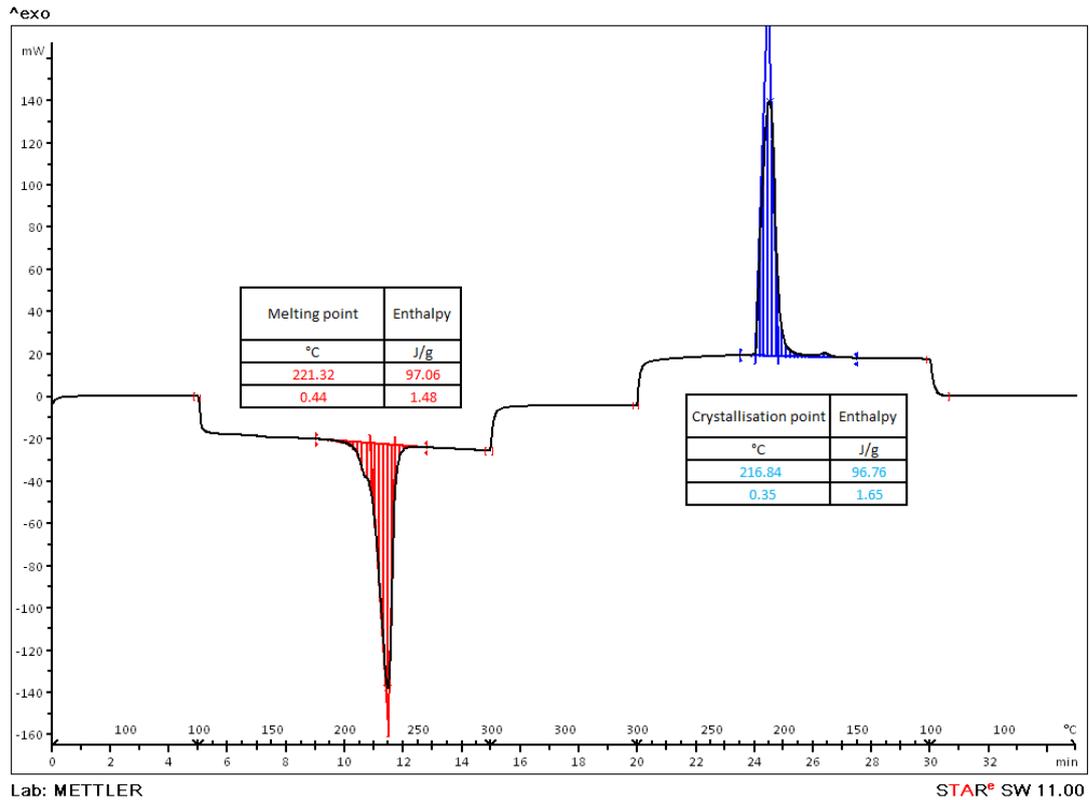
Figure 66: Melting and crystallisation of binary nitrate salts (60 wt. % NaNO$_3$ & 40 wt. % KNO$_3$). Table within the graph shows the mean value of the 18 tests carried out.

5.4 Thermo-Gravimetric Analysis of Binary Nitrate Salt

The decomposition of this nitrate salt mixture showed that it was stable up to 550°C. Above that point, there was rapid degradation (75% mass loss, Fig. 67) of the salt, with most of the mass, lost between 550°C and 800°C. Gradual settling of the weight occurred above 800°C implying that a solid stable compound was produced. With a nitrogen atmosphere used to prevent oxidation, most of the mass loss will have been through the release of nitrogen and oxygen gas. The solid mass left in the crucible will probably be a blend of potassium and sodium oxide.

The chemical transitions occurring during the decomposition of this salt will be the following [114]:

- $NaNO_3$ $_{(l)}$ $\leftrightarrow$ $NaNO_2$ $_{(l)}$ + $_{1/2}O_2$ $_{(g)}$ This pseudo-equilibrium occurred above 550°C

- $2NaNO_2$ $_{(l)}$ $\rightarrow$ $Na_2O_{(s)}$ + N_2 $_{(g)}$ + $_{3/2}O_{2(g)}$ As temperature rose, the nitrite further decomposed producing nitrogen gas and sodium oxide.

- In a similar manner to $NaNO_3$, $KNO_{3(l)}$ $\leftrightarrow$ KNO_2 $_{(l)}$ + $_{1/2}O_2$ $_{(g)}$ goes into a pseudo-equilibrium above 550°C

- $2KNO_2$ $_{(l)}$ $\rightarrow$ K_2O + N_2 + $_{3/2}O_2$ $_{(g)}$ Decomposition led to the production of oxides which explained why the mass settled at 25%, as a blend of both potassium and sodium oxide were produced.

The flow of nitrogen through the furnace would have pushed the equilibrium toward the production of nitrite by removing any gas created.
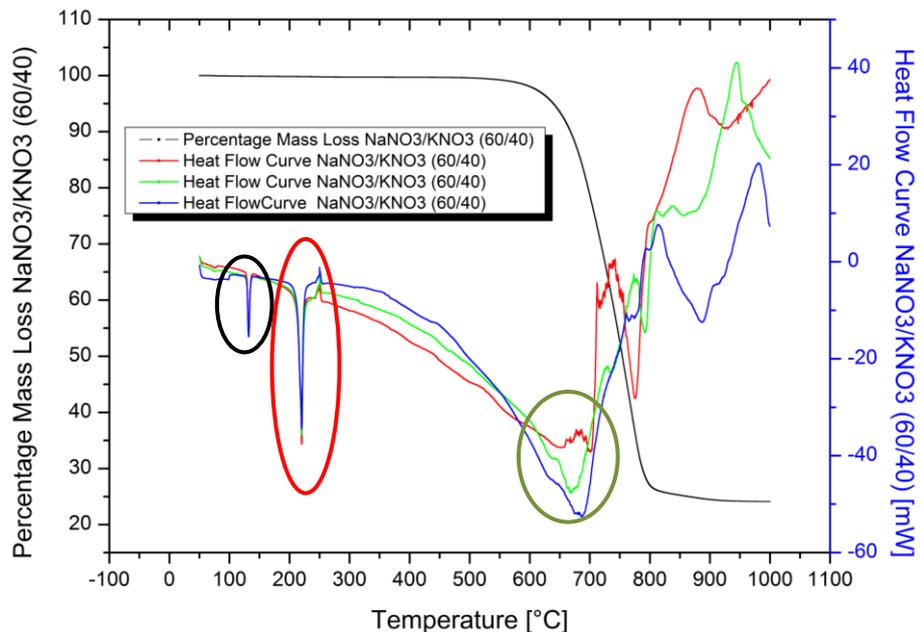
Figure 67: Thermo-gravimetric analysis of binary nitrate mixtures (60 wt. % NaNO₃ & 40 wt. % KNO₃) where percentage mass loss (left x-axis) and heat flow (right x-axis) are plotted against temperature.

The DSC trace showed a peak at 131°C with no mass loss which was the allotropic transformation of KNO_3, prior to the melting of the salt which occurred at 221°C as expected [115]. The heat flow was stable and smooth until 600°C, whereupon, it started to fluctuate (green circle) and the heat flow suddenly rose around 700°C. Combined with mass loss it could be argued that above 550°C the nitrate started to decompose into nitrite. The equilibrium would largely favour nitrite production resulting in mass loss due to the production of oxygen gas from 550°C to 650°C before the gradient of decomposition reached its maximum. Beyond that point the nitrite further decomposed into its final products.

5.5 Rheological Analysis of Binary Nitrate Salt

The rheology of this nitrate salt blend revealed that the viscosity was not affect by an increased shear rate indicating that the salt behaved like a Newtonian fluid as displayed on Figure 69. Furthermore at low revolution, shear thinning was observed such that measurements were always carried out above a shear rate of 100 s^{-1}. This was also reported by Jo et al, 2012 at 300°C with an average value of 3.27 mPa.s between 100 to 1000 s^{-1} which agreed well with the gathered data (Fig. 68 & 69).
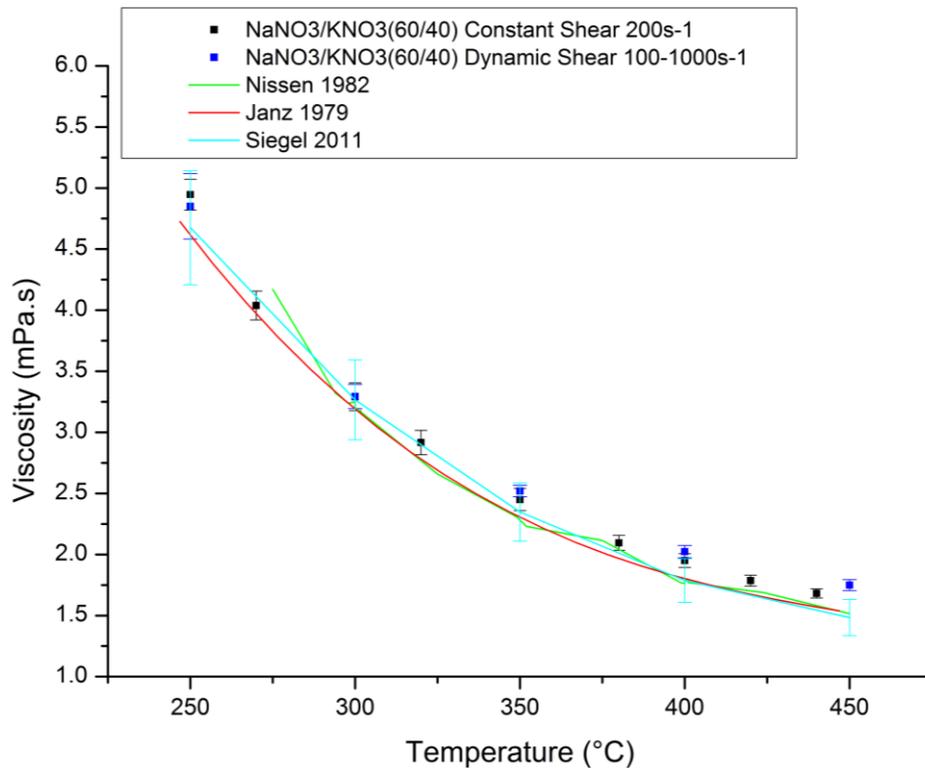
Figure 68: Viscosity measurement with increased temperature of binary nitrate salt mixture (60 wt. % NaNO$_3$ & 40 wt. % KNO$_3$) [116-118].

At constant shear rate of 200 s^{-1}, the results were still within range of the dynamic data although they were more accurate with lower standard of deviation (<2.0%). Siegel et, al 2011 used a shear rate of 100 s^{-1} but the collected data displayed large deviation of ±10.0% whilst Nissen et, al 1982 measured the data using a harmonic oscillator which would probably not have had the accuracy of current equipment although it matched data from Janz et al, 1979 [116-118]. The trend in data agreed well with the few journals exploring this type of research.
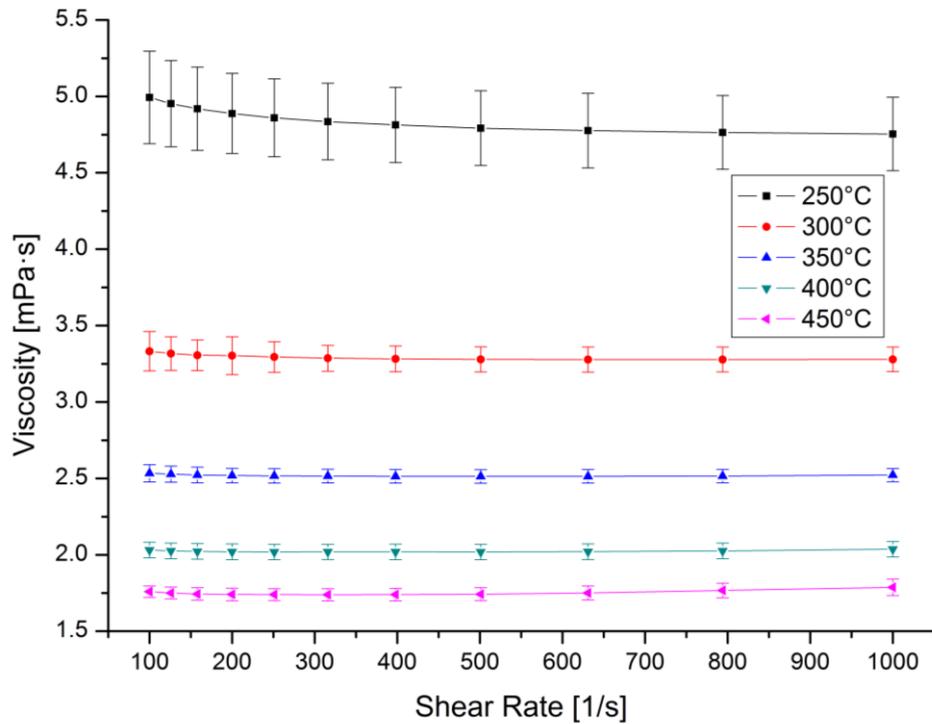
Figure 69: Shear rate plotted against viscosity of the eutectic nitrate salt (60 wt. % NaNO$_3$ & 40 wt. % KNO$_3$) at different temperatures.

5.6   Summary of Nitrate Salt Characterisation

With little collated data on the thermal characteristics of this nitrate salt mix, the main objective was to ensure the specific heat capacity (1.4 J/[g*°C] at 260°C to 1.44 J/[g*°C] at 440°C), enthalpy (H$_f$: 97.06J/g, H$_c$: 96.76J/g), temperature of change (T$_m$: 221.32°C, T$_c$: 216.84°C) and viscosity were accurately measured for the screening process.

The next step was to measure the Cp of various mixtures containing nano-particles changing their concentration to analyze if this had any impact on the results.

Chapter 6 Results & Discussion: Salt Characterisation with Additives

This chapter discuss the results obtained in the screening process of nano-particle additives in eutectic mixture of nitrates (60 wt% $NaNO_3$ & 40 wt% KNO_3).

6.1   Zinc Oxide additive (ZnO)
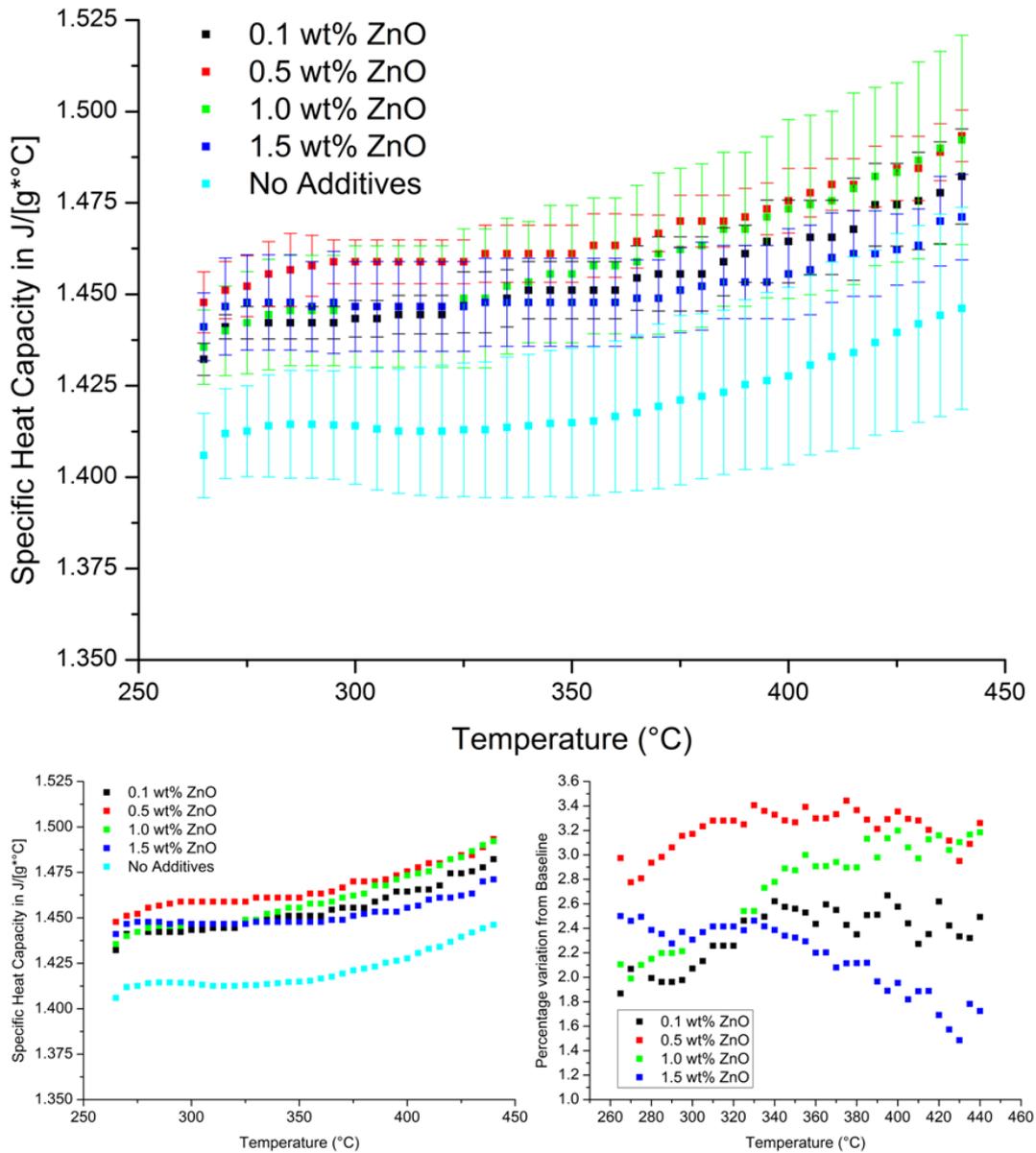
Figure 70: Top diagram shows how the addition of various concentrations of ZnO nano-particles to a nitrate blend (60 wt. % NaNO$_3$ & 40 wt. % KNO$_3$) affected the Cp. Bottom left graph is a duplicate of the top but without the error bars, whilst the bottom right display the percentage variation of the mean compared to the salt without additives (cyan).

The addition of ZnO nano-particles displayed significant increase in specific heat capacity for a concentration of 0.5 wt%. This equated to an enhancement of around 3.2%. The rest of the data (0.1, 1.0 & 1.5 wt %) had

intertwined error bars with the sample containing no additives which could imply that the increase is caused by variance of the results rather than by the effect of the actual additive (ZnO). Whilst the latter looked large, the maximum variance in data was below 2.0%. Furthermore there seemed to be no relationship between concentration of nano-particles and increase in specific heat capacity.
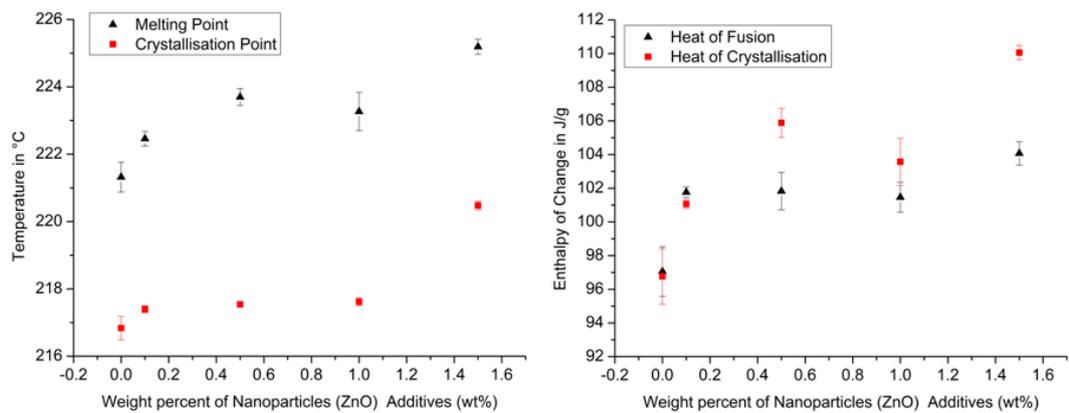
Figure 71: Left hand side diagram showed the variation in melting and crystallisation point with diverse concentration of ZnO nano-particles (0.0 wt%, 0.1 wt%, 0.5 wt%, 1.0 wt% and 1.5 wt%) whilst right hand side diagram demonstrated how the enthalpy of melting or freezing was affected by the nano-additives.

The addition of nano-particles affected both the melting and crystallisation point causing the latter to increase which was also the case of the enthalpy of change. The effect of overcooling was not reduced by the addition of these nano-particles, however the amount of energy between the enthalpy of change was on occasion found to be different between fusion and crystallisation. This could be due to slight differences in the integration of the peaks during measurements. Alternatively, slight misplacement of the pans could have affected these results.

6.2   Titanium Dioxide additive (TiO₂)
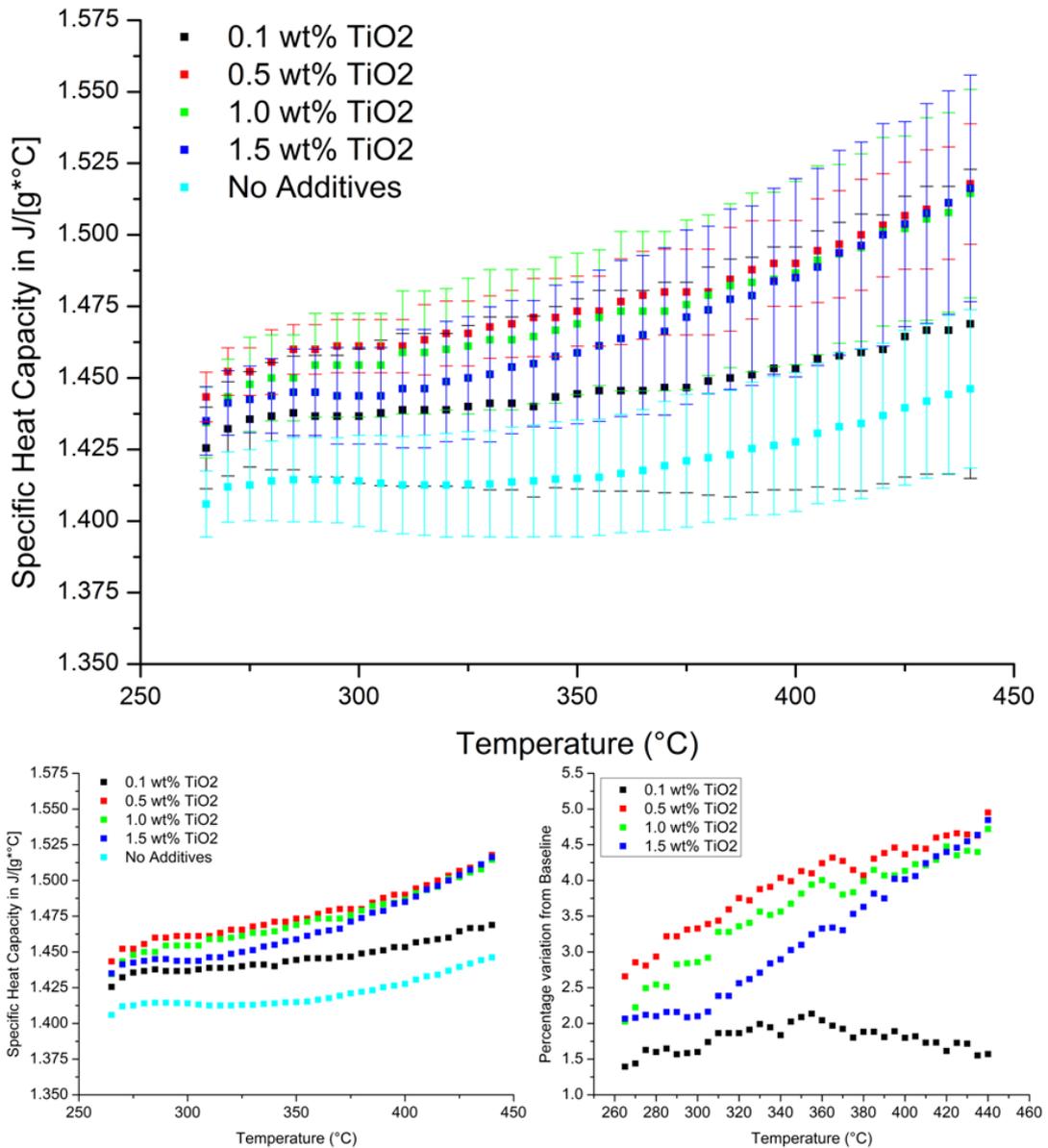
Figure 72: Top diagram shows how the additions of various concentrations of TiO₂ nano-particles to a nitrate blend (60 wt. % NaNO₃ & 40 wt. % KNO₃) affected the Cp. Bottom left graph is a duplicate of the top but without the error bars, whilst the bottom right display the percentage variation of the mean compared to the salt without additives (cyan).

The behaviour of TiO₂ nano-particles was rather strange as the specific heat capacity was increased by a similar amount for 0.5 wt%, 1.0 wt% and 1.5 wt% of nano-particles all achieving a maximum of around 4.70 % increase

compared to salt with no additives (Fig. 72). Only 0.1 wt% showed very slight increase in Cp which was irrelevant if the standard deviation is taken into account as there are large variations in data (Black error bars). The variation of the rest of the results tended to indicated that all three concentrations significantly impacted the mixture and its ability to store heat (Fig. 72).
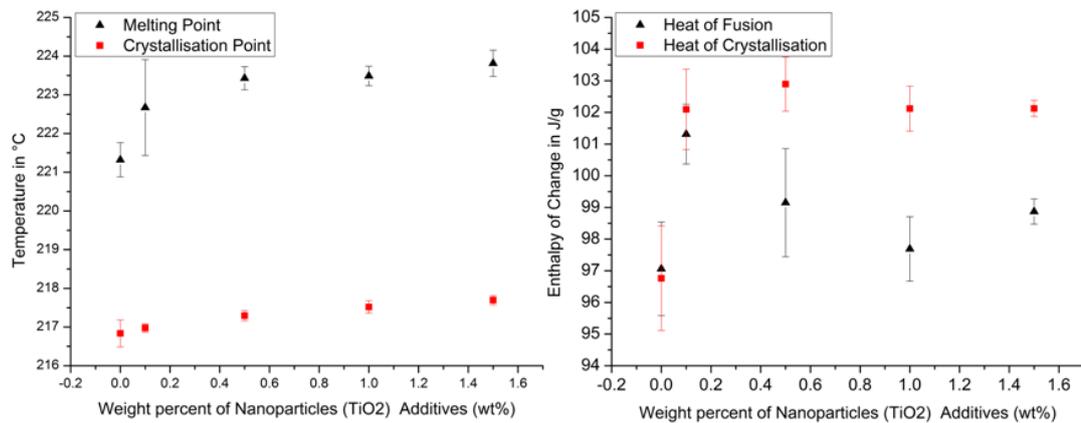
Figure 73: Left hand side diagram showed the variation in melting and crystallisation point with different concentration of TiO$_2$ nano-particles (0.0 wt%, 0.1 wt%, 0.5 wt%, 1.0 wt% and 1.5 wt%) whilst right hand side diagram demonstrated how the enthalpy of melting or freezing was affected by the nano-additives.

The melting point seemed to be altered by the nano-particles rising from 221.2°C to around 223°C, however very little change was seen in the crystallisation regardless of the concentration added. The enthalpy of crystallisation was again higher than that of fusion for 0.5 wt%, 1.0 wt% and 1.5 wt% which could also be due to experimental error. The nano-particle additive might also be responsible for this difference in enthalpy if the mixture was unstable.

6.3 Copper additive (Cu)
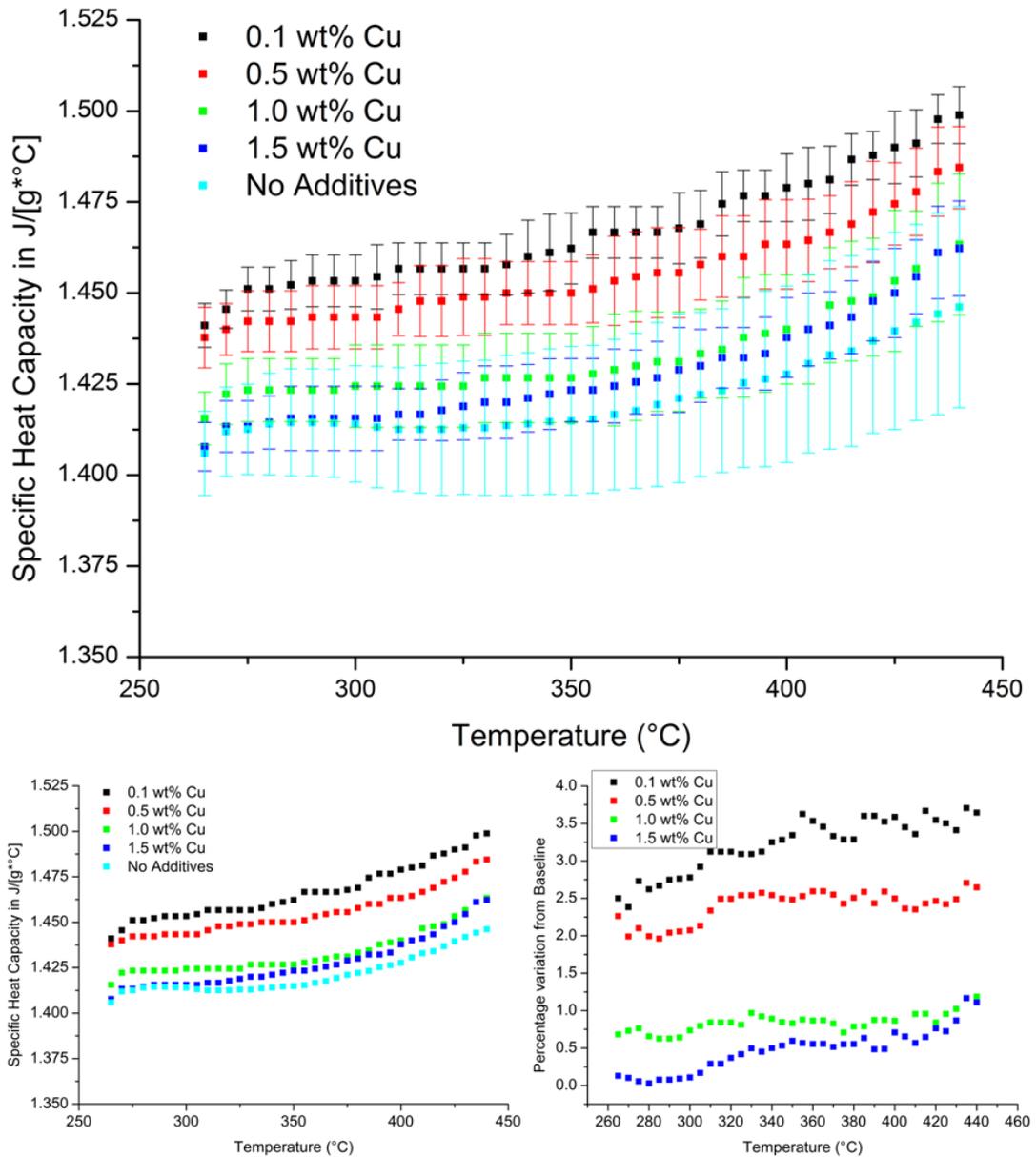
Figure 74: Top diagram shows how the additions of various concentrations of Cu nano-particles to a nitrate mix (60 wt. % NaNO₃ & 40 wt. % KNO₃) affected the Cp. Bottom left graph is a duplicate of the top but without the error bars, whilst the bottom right display the percentage variation of the mean compared to the salt without additives (cyan).

The utilization of copper nano-particles was interesting as the latter appeared to be dependent on the concentration of additives present in the blend. As the concentration of nano-particles decreased from 1.5 wt% to 0.1

wt%, the maximum mean percentage variation rose from 1.0 % to 3.6 % (Fig. 74). In term of the significance of the results both 1.0 wt% and 1.5 wt% had intertwined error bars with the pure salt (no additives) which would imply that the obtained increase could potentially be due to error. This is not the case for 0.1 wt% and 0.5 wt%.
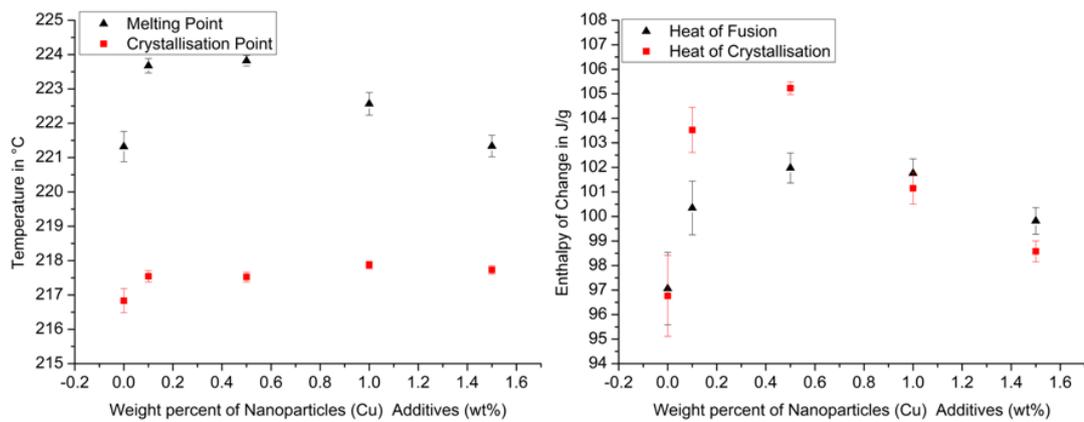
Figure 75: Left hand side diagram showed the variation in melting and crystallisation point with varied concentration of Cu nano-particles (0.0 wt%, 0.1 wt%, 0.5 wt%, 1.0 wt% and 1.5 wt%) whilst right hand side diagram demonstrated how the enthalpy of melting or freezing was affected by the nano-additives.

As described before the melting point slightly increase with 0.1 wt% Cu and then gradually decrease from 0.5 wt% to 1.5 wt% to reach a value similar to that of the pure binary mixture. The crystallisation temperature was however similar with little variance seen. As for the enthalpy of fusion, there also seemed to be very little variation in between the different concentration of nano-particles utilized but the overall trend was an increase in thermal energy needed to melt the sample, although that increase was slight.

6.4   Silicon dioxide additive (SiO$_2$)
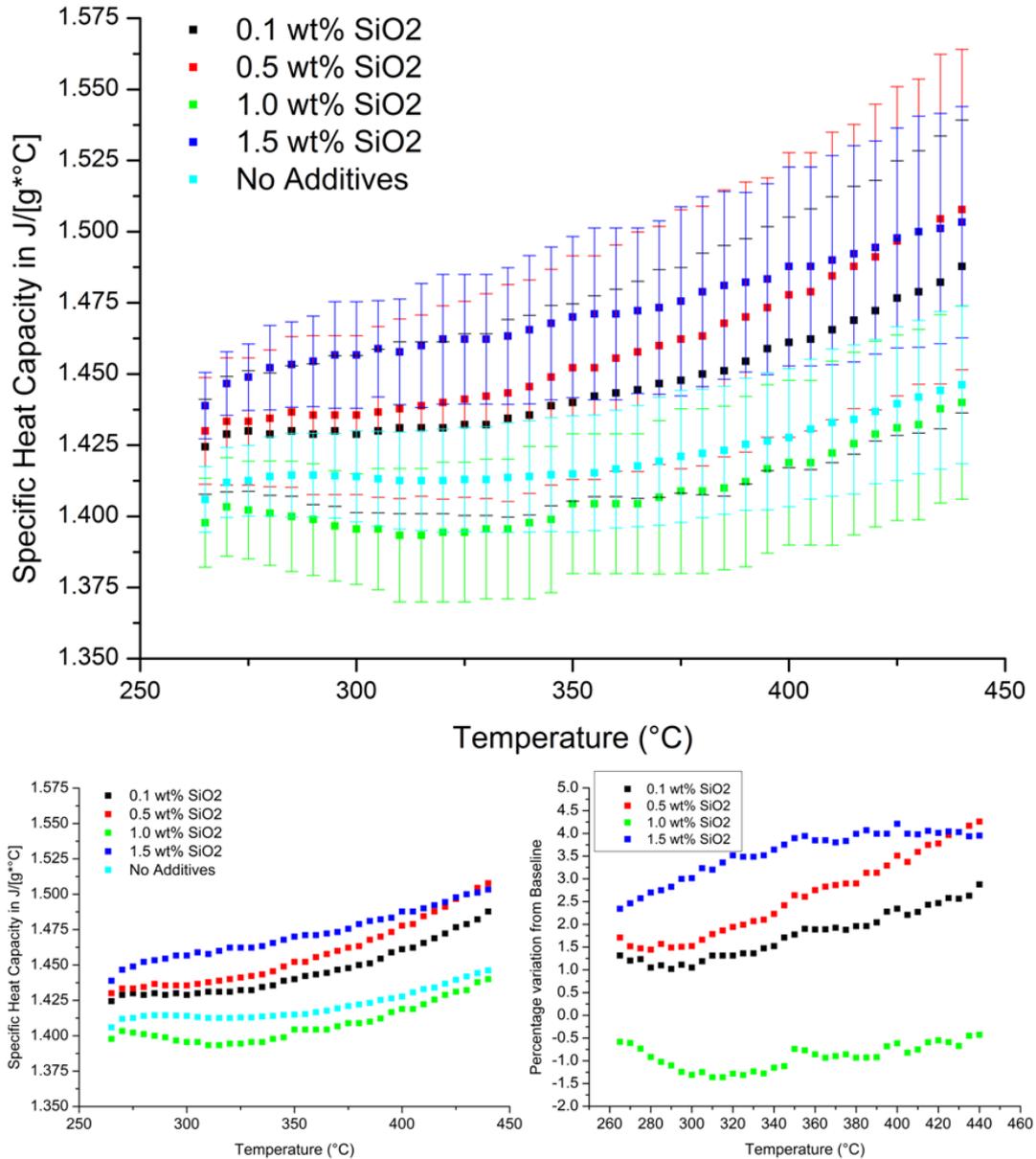
Figure 76: Top diagram shows how the additions of various concentrations of SiO$_2$ nano-particles to a nitrate blend (60 wt. % NaNO$_3$ & 40 wt. % KNO$_3$) affected the Cp. Bottom left graph is a duplicate of the top but without the error bars, whilst the bottom right display the percentage variation of the mean compared to the salt without additives (cyan).

The results gathered for the use of silicon dioxide nano-particles displayed a maximum increase of around 4.0 % for 1.5 wt% and 0.5 wt% additives. However the large variation in the obtained data could indicate that the

mixture was unstable which could also explain the negative enhancement seen for 1.0 wt %. There seemed to be no clear relationship between percentage additive and Cp change.
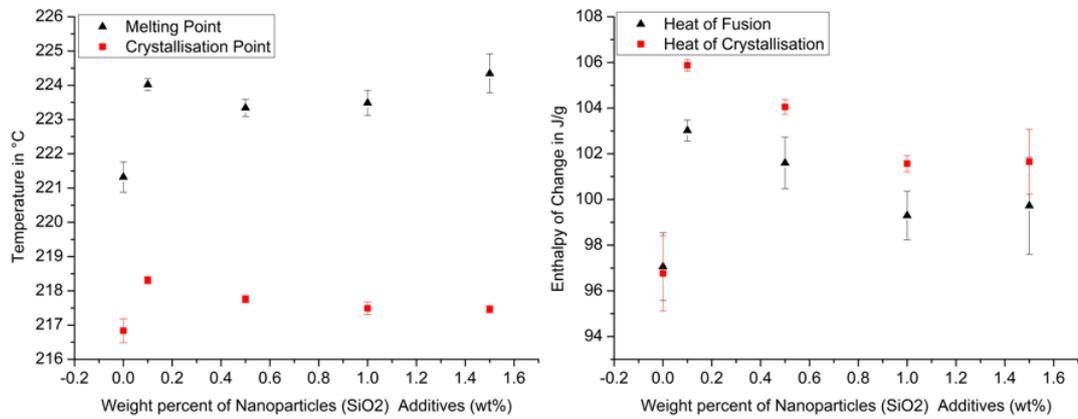
Figure 77: Left hand side diagram showed the variation in melting and crystallisation point with varied concentration of SiO$_2$ nano-particles (0.0 wt%, 0.1 wt%, 0.5 wt%, 1.0 wt% and 1.5 wt%) whilst right hand side diagram demonstrated how the enthalpy of melting or freezing was affected by the nano-additives.

Both melting and crystallisation point as well as enthalpy of change were higher for the mixture containing SiO$_2$.

6.5   Copper Oxide additive (CuO)
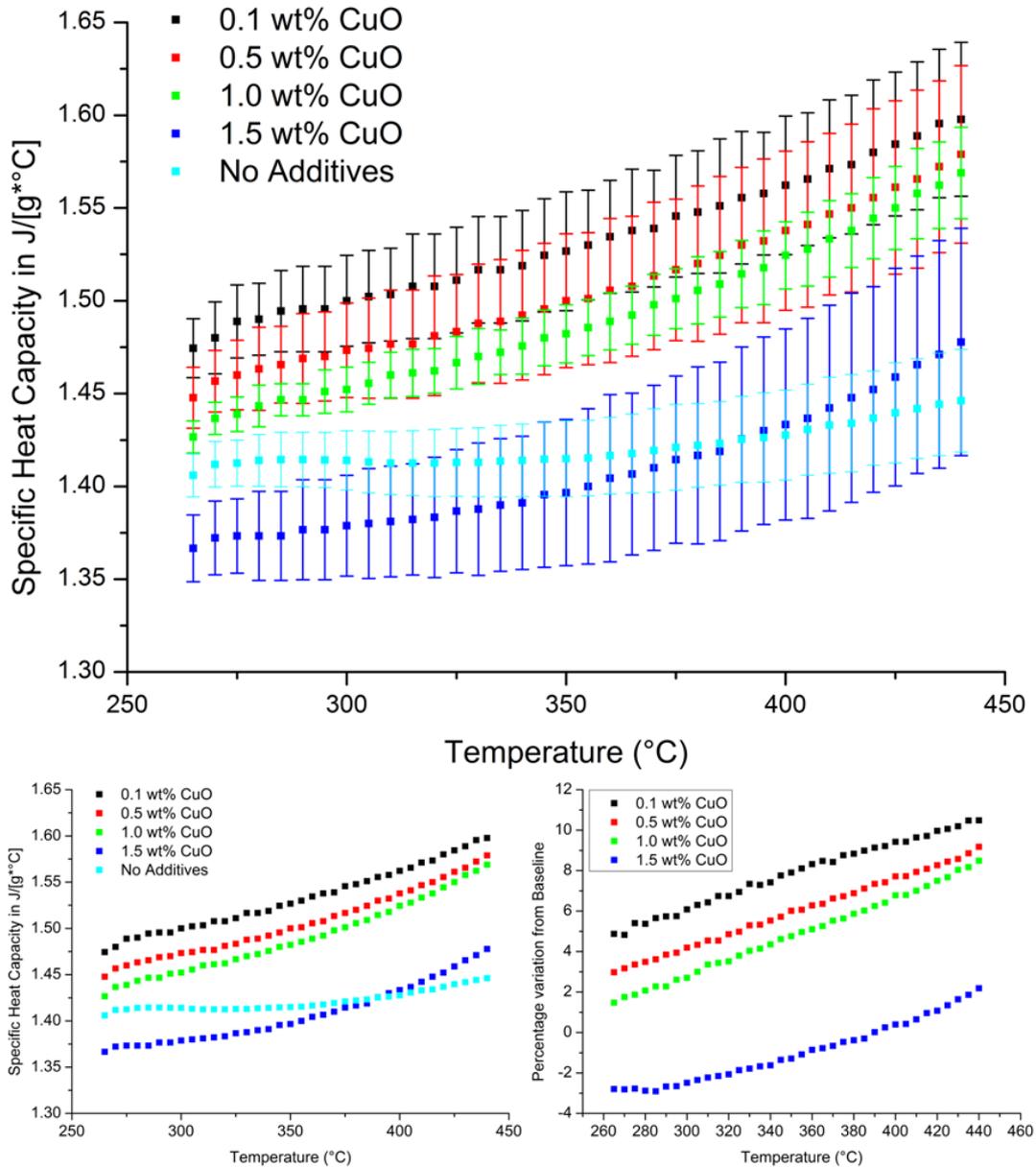
Figure 78: Top diagram shows how the additions of various concentrations of CuO nano-particles to a nitrate mix (60 wt. % NaNO₃ & 40 wt. % KNO₃) affected the Cp. Bottom left graph is a duplicate of the top but without the error bars, whilst the bottom right display the percentage variation of the mean compared to the salt without additives (cyan).

The use of copper oxide nano-particles displayed similar trend to copper such that the enhancement was dependent on the concentration of additives present. However the percentage increase was much larger with a maximum

increase of 10.5 % with 0.1 wt% CuO, 9.2 % with 0.5 wt % CuO and finally 8.5 % with 1.0 wt % CuO. The use of 1.5 wt % CuO caused a large decrease in the Cp and the maximum end up been 2.1 %. The variation of the data (<3.0%) clearly demonstrated no intertwined error bar for the first three concentrations, which validated the beneficial effect of this particular additives.
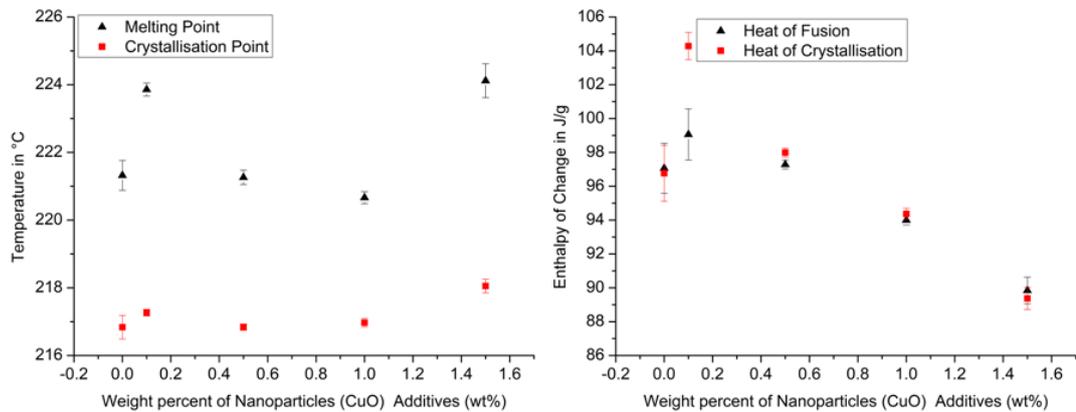
Figure 79: Left hand side diagram showed the variation in melting and crystallisation point with diverse concentration of CuO nano-particles (0.0 wt%, 0.1 wt%, 0.5 wt%, 1.0 wt% and 1.5 wt%) whilst right hand side diagram demonstrated how the enthalpy of melting or freezing was affected by the nano-additives.

The melting point was increased with 0.1 wt % and 1.5 wt % of CuO whilst the crystallisation point showed only slight increase for 1.5 wt%. The enthalpy values were the same for both crystallisation and fusion which was to be expected except that of 0.1 wt % CuO which displayed differing values.

6.6 Summary & Further Discussion

6.6.1 Summary

The aim of this screening process was to investigate how the addition of various nano-particles affected a eutectic mixture of nitrate (60 wt% $NaNO_3$ & 40 wt% KNO_3) and which concentration resulted in the highest Cp enhancement.

The results demonstrated that the addition of nano-particles had in most cases a beneficiary effect toward the specific heat capacity (Table 6). This was unlike published data by Chieruzzi, et al, 2013 which displayed negative enhancement when using TiO_2 and SiO_2 nano-particles (0.5, 1.0 & 1.5 wt.%) [119]. Dubba, et al, 2013 on the other hand displayed positive enhancement of SiO_2 of 10% to 28% depending on the size of the nano-particles. Of the screening process, 0.1 wt% copper oxide displayed the largest increase (Table 6).

The melting and crystallisation point as well as the enthalpy of change (fusion/solidification) tended to increase whilst the actual onset of melting decrease similarly to what is stated by Chieruzzi, et al, 2013 [119] (Table 7). Whilst this may seem contradictory, the change of phase is defined by three stages. The onset of melting is interpreted as the temperature at which the sample started to collapse on itself such that the salt started to adhere to the side of the platinum crucible. At this point in time a semi-liquid phase is created whereupon not all of the salt is at liquid state. The melting point was therefore defined as the high temperature at which the salt was fully melted.

Table 6: Mean percentage enhancement of Cp at 440°C for different type and concentration of nano-particles

	Nano-particles concentration wt.%	Specific Heat Capacity in J/[g°C] in liquid phase at 440°C	Percentage Enhancement at 440°C
Base Salt	0	1.446	-
Base Salt + ZnO	0.1	1.482	2.49
	0.5	1.493	3.26
	1	1.492	3.18
	1.5	1.471	1.72
Base Salt + TiO$_2$	0.1	1.468	1.57
	0.5	1.517	4.95
	1	1.514	4.72
	1.5	1.516	4.84
Base Salt + Cu	0.1	1.498	3.64
	0.5	1.484	2.64
	1	1.463	1.18
	1.5	1.462	1.10
Base Salt + SiO$_2$	0.1	1.487	2.87
	0.5	1.507	4.26
	1	1.440	-0.42
	1.5	1.503	3.95
Base Salt + CuO	0.1	1.597	10.48
	0.5	1.578	9.17
	1	1.568	8.48
	1.5	1.477	2.18

In theory the melting range of a pure sample is very low and only spanned for a couple of degrees Celsius. In this case, however the salt without additive was already a binary mixture of salt (NaNO$_3$ = T$_m$ 308.01°C + KNO$_3$ = T$_m$ 336.03°C with ratio 60/40) which increase the entropy thereby lowering the melting point to 221.32°C. Through the same train of thought, any nano-particles addition to the binary salt mixture can be regarded as impurities increasing furthermore the level of entropy. This should in theory lead to a lower onset of melting and a broader peak during the melting process.

Indeed Table 7 illustrated this, with the majority of onset been lower than that of the binary mixture.

Table 7: Onset of Melting

	Nano-particles concentration wt.%	Onset of Melting	St.dev	Percentage Difference with onset of Pure salt
Base Salt	0	215.031	0.34	-
Base Salt + ZnO	0.1	213.908	0.18	-0.52
	0.5	212.507	0.41	-1.17
	1	212.922	0.59	-0.98
	1.5	218.224	0.24	1.49
Base Salt + TiO$_2$	0.1	212.901	1.69	-0.99
	0.5	212.106	0.55	-1.36
	1	212.554	0.20	-1.15
	1.5	213.143	0.19	-0.88
Base Salt + Cu	0.1	212.773	0.59	-1.05
	0.5	211.951	0.09	-1.43
	1	213.427	0.20	-0.75
	1.5	214.270	0.29	-0.35
Base Salt + SiO$_2$	0.1	214.829	0.10	-0.09
	0.5	213.242	0.11	-0.83
	1	213.257	0.12	-0.83
	1.5	212.779	1.06	-1.05
Base Salt + CuO	0.1	212.377	0.35	-1.23
	0.5	214.729	0.15	-0.14
	1	215.024	0.16	0.00
	1.5	213.819	0.22	-0.56

Regarding the broader peaks, Figure 80, demonstrated the difference between the binary salt mixtures without additives which displayed a higher peak, with a narrow melting range compared to the addition of 1.5 wt% copper oxides. The latter decrease the onset of melting and its peaks but increase the melting range (Fig. 80).
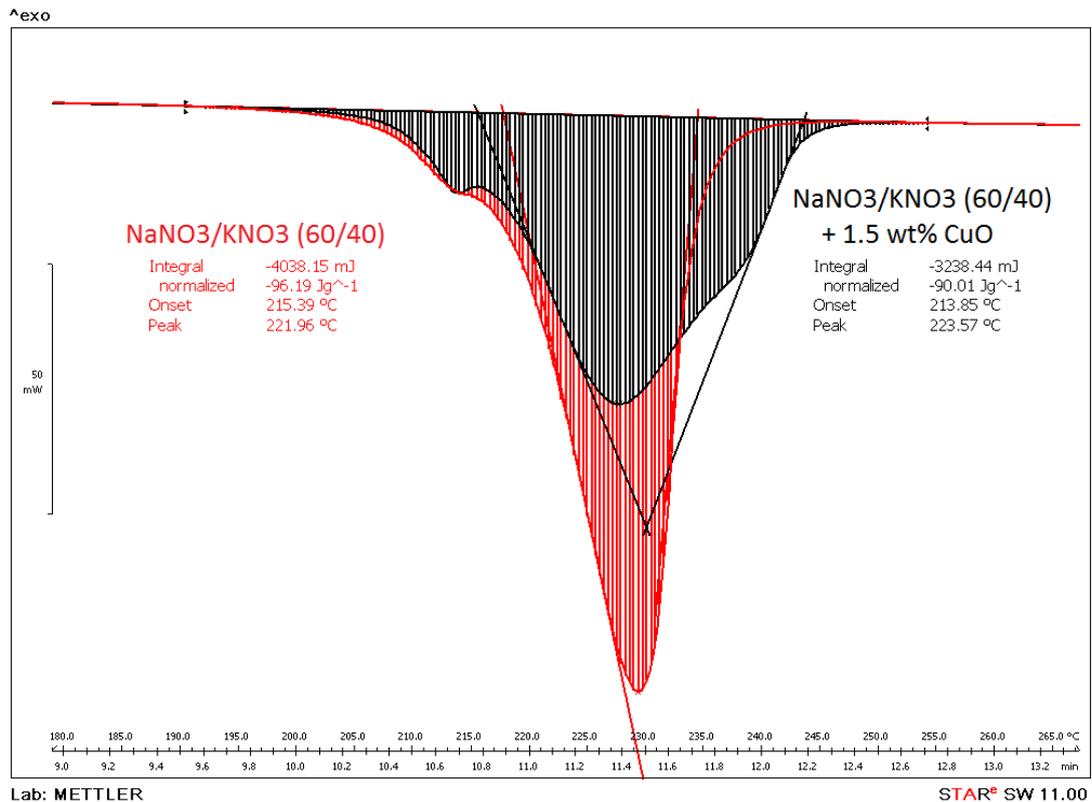
Figure 80: Illustration of the difference in shape and size of the peaks when nano-particle (1.5 wt% CuO) was present or absent.

6.6.2 Discussion

The addition of nano-particles to ionic fluids such as inorganic salt clearly affected the thermo-physical characteristics of the fluid. The presence of nano-sized solid particles will influence both the thermal conductivity and specific heat capacity of the molten salt. With large surface area to volume ratio, the nano-particle will display thermo-physical properties different from bulk. It is known that nano-particles display higher surface energy compared to bulk [91]. This is due to an increased degree of freedom in atoms found at the edges of nano-particles which display lower vibrational energy compared to atoms located away from the edges. As heat capacity is linked to the structure of the nano-particle, its vibrational and configurational entropy, decreasing the size of nano-particles is going to lead to a rise in the

amount of exposed atoms. Whilst this has been showed to promote an increase in specific heat capacity, many factors such as shape, purity and density to name but a few might also affect this thermal properties [92]. Described as a potential mode for the enhancement of Cp in Chapter 2.8, it is unlikely to be one of the main mechanism that could explain this abnormal rise. With values below that of molten salt, the increase in Cp cannot be explained by this mode alone as this solid structure would have to display extremely high Cp to cause a 10.0% rise with a 0.1 weight percent fraction of CuO added. Furthermore theoretical description of Cp through the Einstein or Debye heat capacity model demonstrate that a plateau is reached at high temperature whereupon the value does no increase and stays constant. Whilst Einstein model assumes a single vibration frequency in solid, Debye regards it as a continuous elastic solid meaning that the calculation of temperature in each model differs [120]. However at high temperature, the correlation of both model is similar.
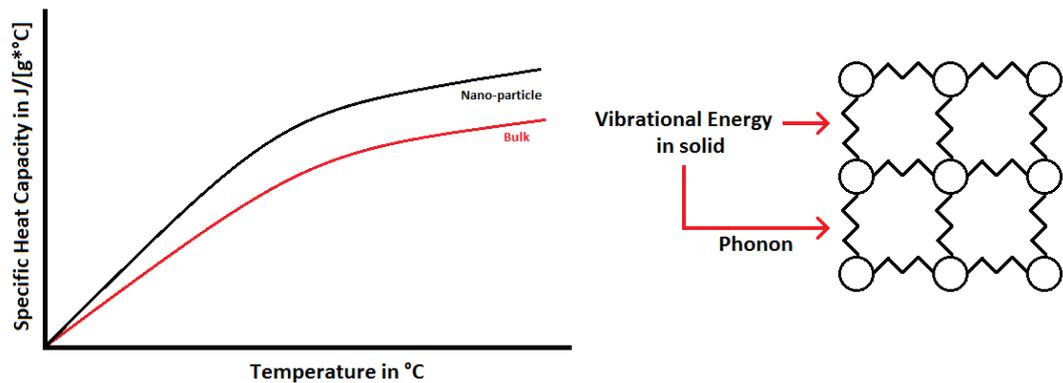
Figure 81: Schematic of heat capacity of Bulk material vs. Nano-particle on the left and on the right a representation of a solid lattice of atoms where the vibrational energy between atoms is responsible for the heat capacity storage.

Stored through vibrational frequency between atoms, the latter is directly correlated to temperature. At zero degree Kelvin no energy can theoretically be stored. As temperature increase, frequency of vibration between atoms increase up to a point where maximum value is reached.

The next potential mode of energy storage was identified to be the interfacial resistance (Mode 2: Chapter 2.8, Fig. 82) taking place between the solid and liquid. Indeed at this point, the transfer of energy is disrupted due to a change in electronic and vibrational properties as energy carrier such as phonon or electron try to cross this boundary. It is unlikely that this Mode is responsible for specific heat capacity although it might play a role in the enhancement of Cp by providing storage through the difference in vibrational energy between that of the solid nano-particle and the liquid layer.

Furthermore the liquid present at this boundary is constrained, displaying a semi-solid behaviour as the atoms surrounding the nano-particle are packed forming a layered interface (Mode 3: Chapter 2.8, Fig. 82). Oh et al, 2005 showed that liquid aluminium atoms formed a layered structure at the interface with alumina [98].
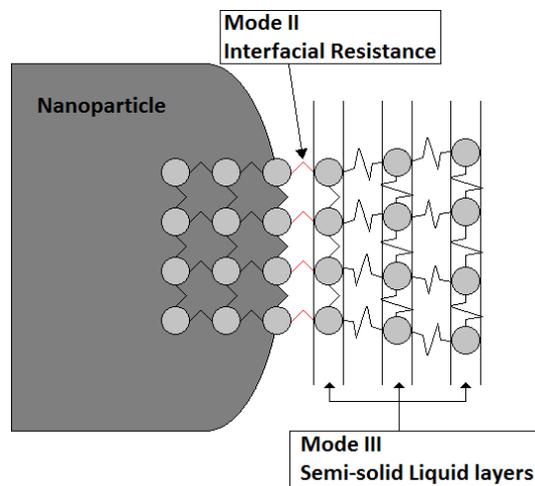
Figure 82: Schematic diagram of Mode II & III

Similarly it has long been identified that these compressed liquid layers might play an important role in the thermal conductivity as the layered atoms around the nano-particle display properties akin to that of solid [121-123].

To account for the increase in specific heat capacity, one would have to postulate that the property of these compressed layers are higher than that of bulk solid by partially accounting for the enthalpy of fusion as these layers would be located in between two phases (Semi-Solid) due to the loosely packed atoms [124]. Therefore the calculation of specific heat capacity needs to take into account the mass fraction of nano-particles as well as the specific heat capacity of the compressed liquid layers.

Following on the same train of thought, the volume of compressed liquid layers will be influenced by the shape and size of the nano-particles. As surface area of contact seems to be of importance, a small tetrahedron nano-particle (10 nm in size) should provide higher increase in Cp compared to a spherical structure of the same dimension. Similarly, decreasing the size will enhance the available surface area of contact.

However agglomeration will negatively impact enhancement by reducing the total volume. This will be dependent of the methodology of dispersion used as it might affect surface properties of the nano-particle and how they interact.

6.7   Powder vs. Liquid Dispersion

Unlike low temperature fluid, where the use of surfactant and alteration of pH are common variables changed to increase the stability of the suspension over time, nano-particles dispersion into inorganic salt cannot be easily modified once introduced in its liquid phase. This implied that dispersion has to be done before melting ever occurred. Two methods of dispersions were thought of:

- Liquid dispersion where the salt is dissolved into distilled water and the nano-particles added. This was followed by sonication, evaporation and removal of hydrates through melting of sample (>250°C). This method of dispersion has been widely used in several research papers [14-16, 90, 119]. One of the first published paper displaying this method was Shin & Banerjee, 2011 [90].
- Powder dispersion entailed the use of a mill to grind and mix the salt and nano-particles together. This technique was used for all of the previously showed specific heat capacity work.

Here it was demonstrated that regardless of the method used the specific heat capacity was almost the same (Fig. 84). This was good news, as the scalability of the powder dispersion was more practical and economically viable compare to the liquid method.

Further characterisation into the method of production showed that the melting, crystallisation and enthalpy of change were significantly increased when the liquid dispersion method was used compared to the milling method (Fig. 85).
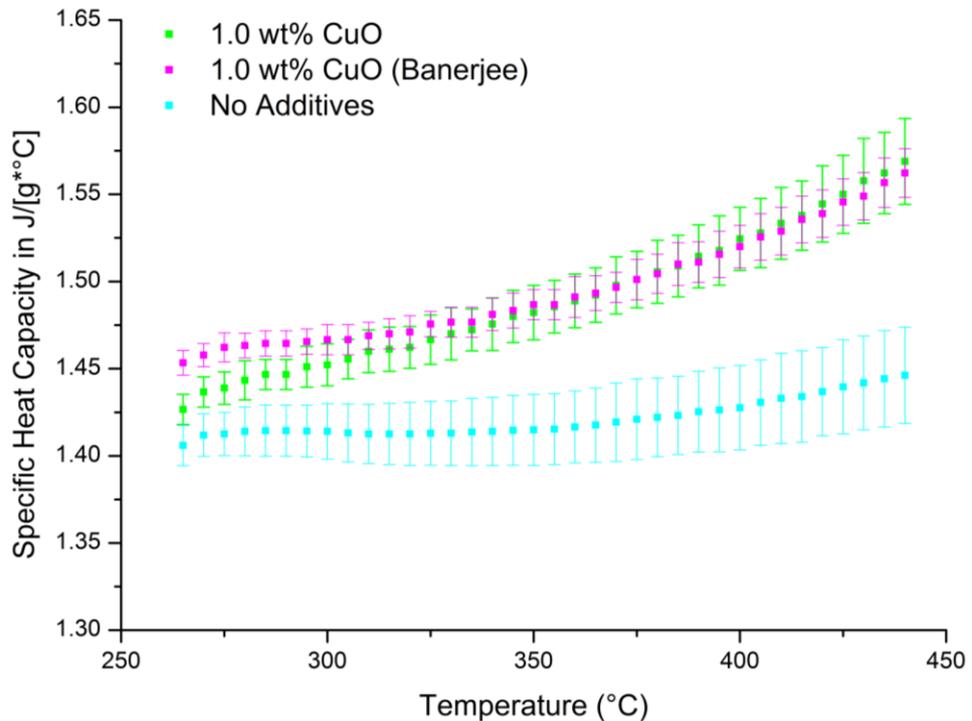
Figure 83: Variation in Cp depending on the method used to produce the sample. The bracketed Banerjee name referred to the liquid dispersion whilst the other (Green) was mixed using powder dispersion.

The liquid method displayed the advantage, through sonication, of allowing the homogenous dispersion of the nano-particles and promoted any aggregates that might have formed to be broken through this process. However the evaporation of water and eventual re-crystallisation might on the contrary lead to the formation of aggregate as the volume of water dropped and the salt crystal formed.

The physical method on the other hand would cause the nano-particles to adhere on the salt surface. The grinding of the potassium and sodium nitrate prior to the introduction of nano-particles would increase the surface area allowing a greater spread of the latter. The only downsides of this method

would be the loss of a fraction of nano-particles that adhered to the ball bearing used as well as the potential contamination.
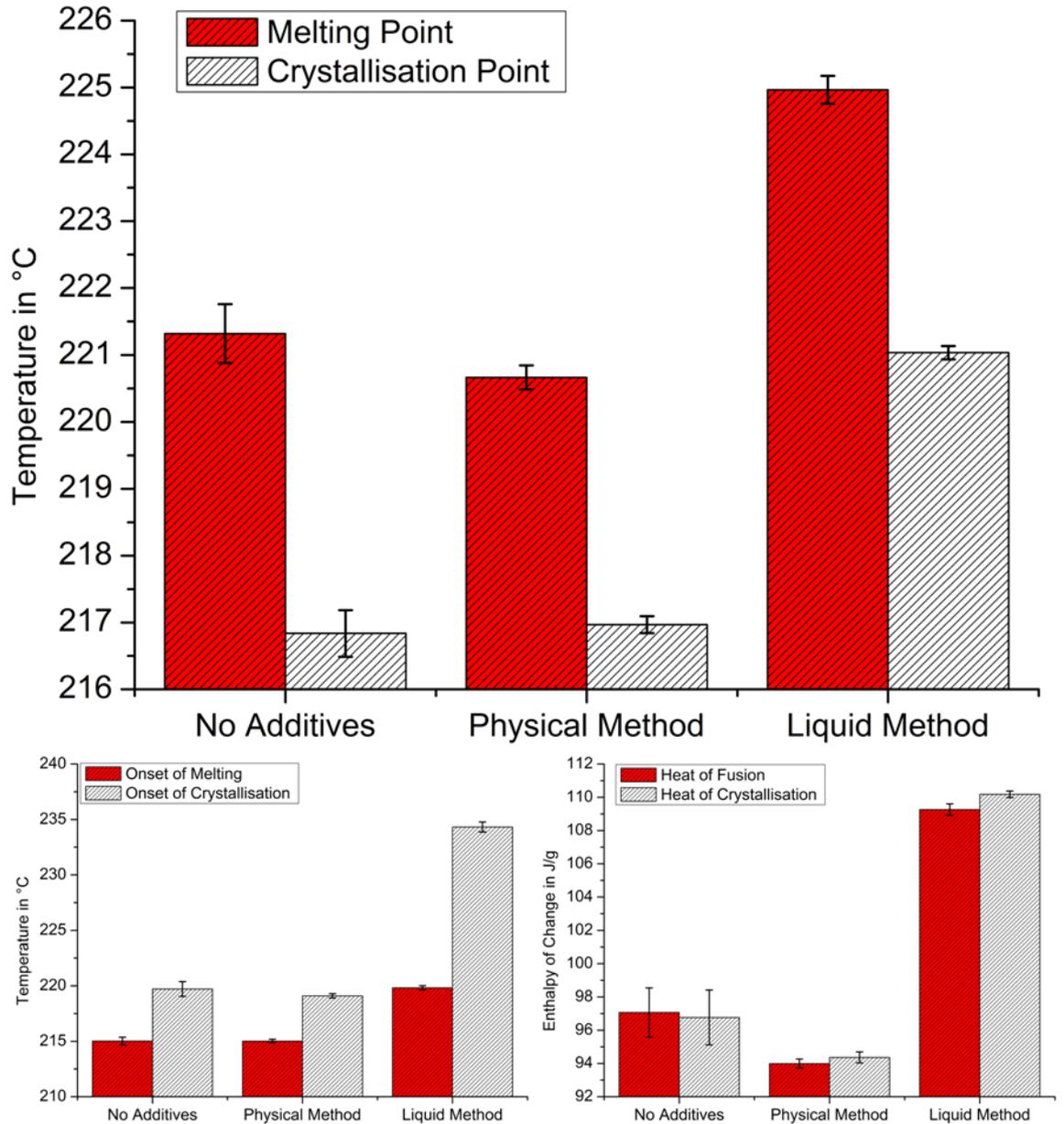
Figure 84: Effect of different dispersion method on the melting/crystallisation and enthalpy of change of 1.0 wt% CuO additives compared to binary nitrate salt (60 wt. % NaNO$_3$ & 40 wt. % KNO$_3$)

6.8   Scanning Electron Microscopy Analysis

SEM analysis of un-melted powdered nano-particles and nitrate mix (60 wt. % $NaNO_3$ & 40 wt. % KNO_3) revealed that the nano-particles adhered and aggregated (Fig. 85) to the salt surface. This was probably caused by a build up of electrostatic charges during the ball milling phase as well as Van der Waal forces promoting adsorption.   It can be seen that without nano-particles, the salt crystal display a smooth surface, which was unlike what the bottom picture of Figure 85 showed, due to the presence of copper-oxide. Although the crystals are of different size and shape, the pictures clearly left no doubt of the interaction between these compounds.
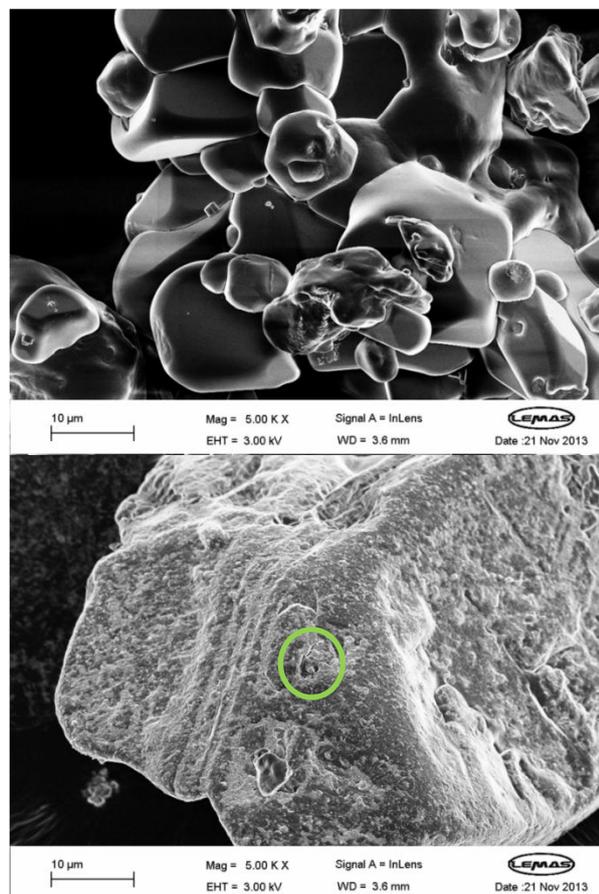
Figure 85: Top-picture: SEM image of non-melted salt crystals containing no additives. Bottom-picture: SEM image of non-melted salt crystal covered with nano-particles (CuO).

1 µm

Mag = 50.00 K X

Signal A = InLens

EHT = 3.00 kV

WD = 3.6 mm

Date :21 Nov 2013
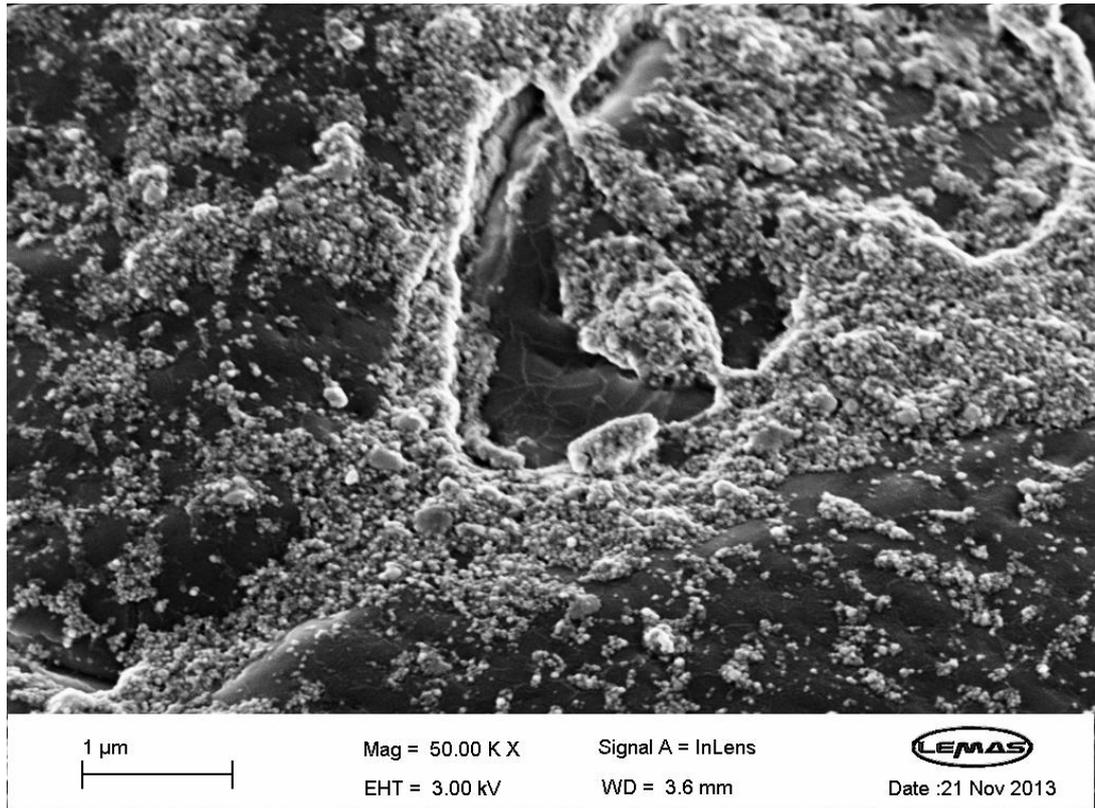
Figure 86: Scaled up version the bottom picture in Figure 99 (green circle showed the area focused on).

The nano-particles visibly altered the crystal formation of the binary nitrate mixture (Fig. 87 & 88). As written previously, the formation of 'nano-structures' stated in Dubba et, al. 2013 and Tiznobaik & Shin. 2013 could be due to the formation of semi-solid layers around the nano-particles [15, 93]. Due to their large surface area to volume ratio, the behaviour of nano-particles differ substantially from bulk and papers have showed that increasing this ratio led to a blue shift in infrared spectroscopy due to the rise in the amount of exposed surface atoms [91, 92]. Whilst the nano-particles itself would not cause the enhancement of specific heat capacity, its interaction with molten salt liquid and particularly the formation of nano-layers might be the main mechanism responsible for this rise.
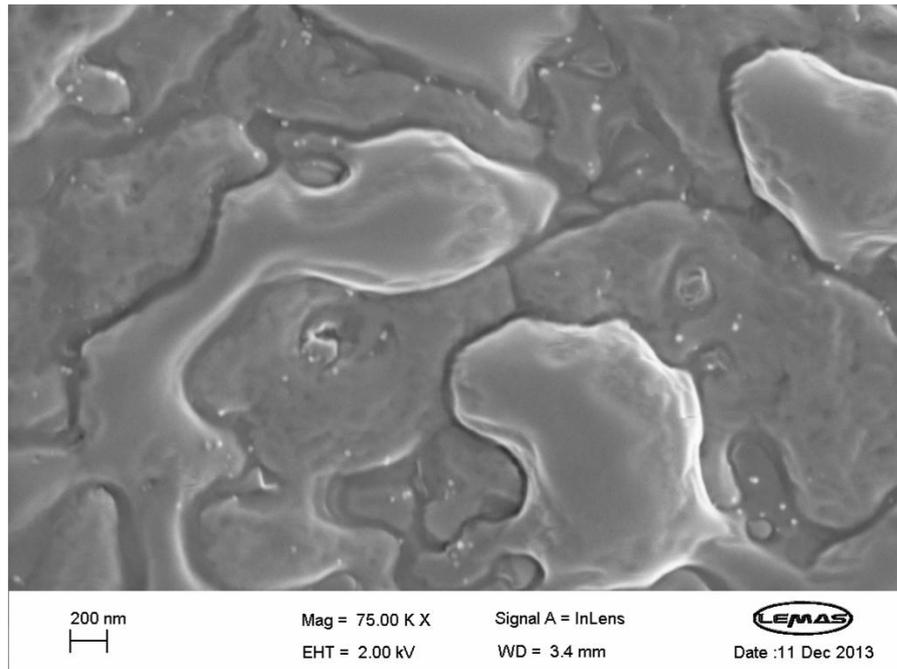
Figure 87: Melted binary nitrate mixture (60 wt. % NaNO₃& 40 wt. % KNO₃) containing no nano-particle additive.
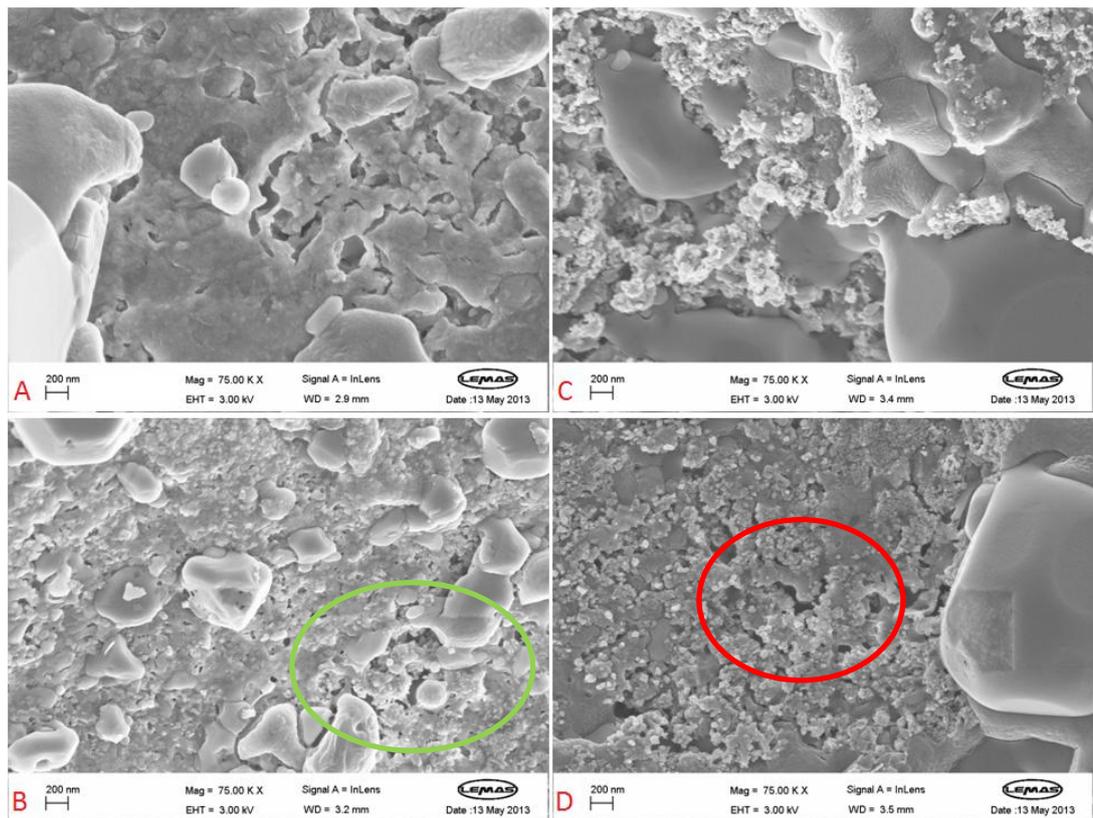
Figure 88: Melted binary nitrate mixture (60 wt. % NaNO₃& 40 wt. % KNO₃) containing varied concentration of CuO nano-particle additive (A = 0.1 wt% CuO, B = 0.5 wt% CuO, C = 1.0 wt% CuO & D = 1.5 wt% CuO)

| 100 nm | Mag = 150.00 K X | Signal A = InLens | LEMAS |
| | EHT = 3.00 kV | WD = 3.2 mm | Date :13 May 2013 |
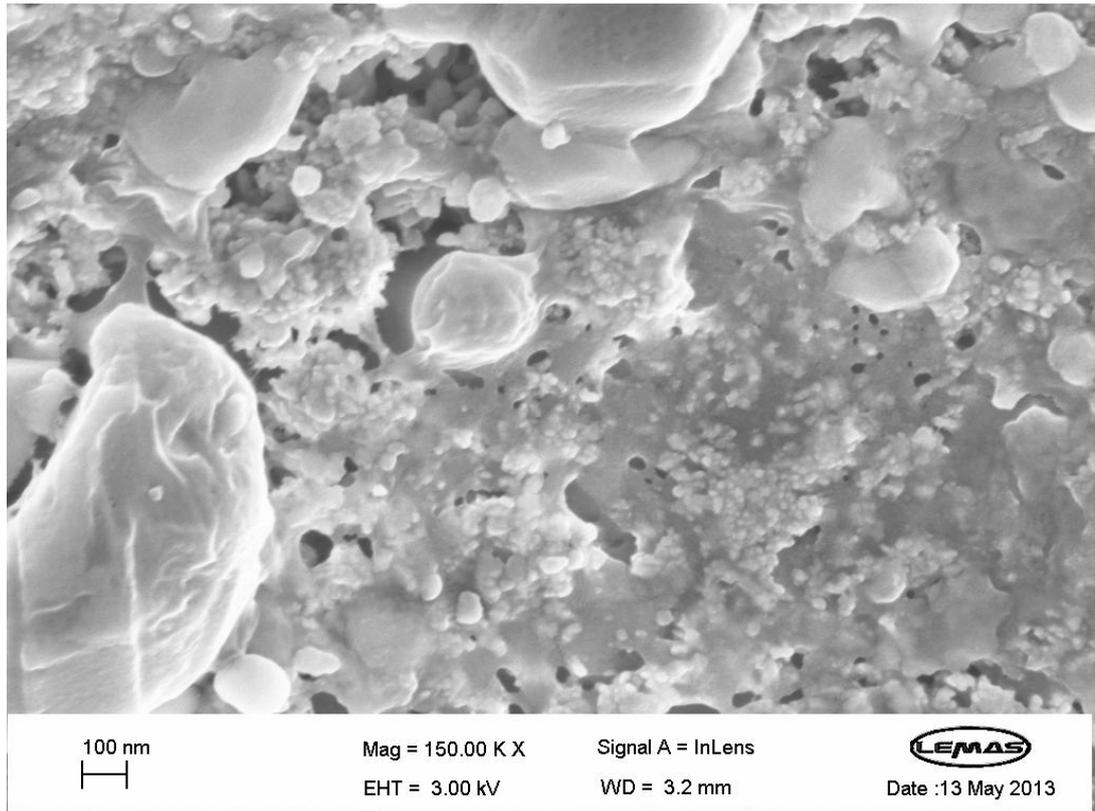
Figure 89: Scaled up version the bottom picture in Figure 102 (green circle showed the area focused on).

| 100 nm | Mag = 200.00 K X | Signal A = InLens | LEMAS |
| | EHT = 3.00 kV | WD = 3.5 mm | Date :13 May 2013 |
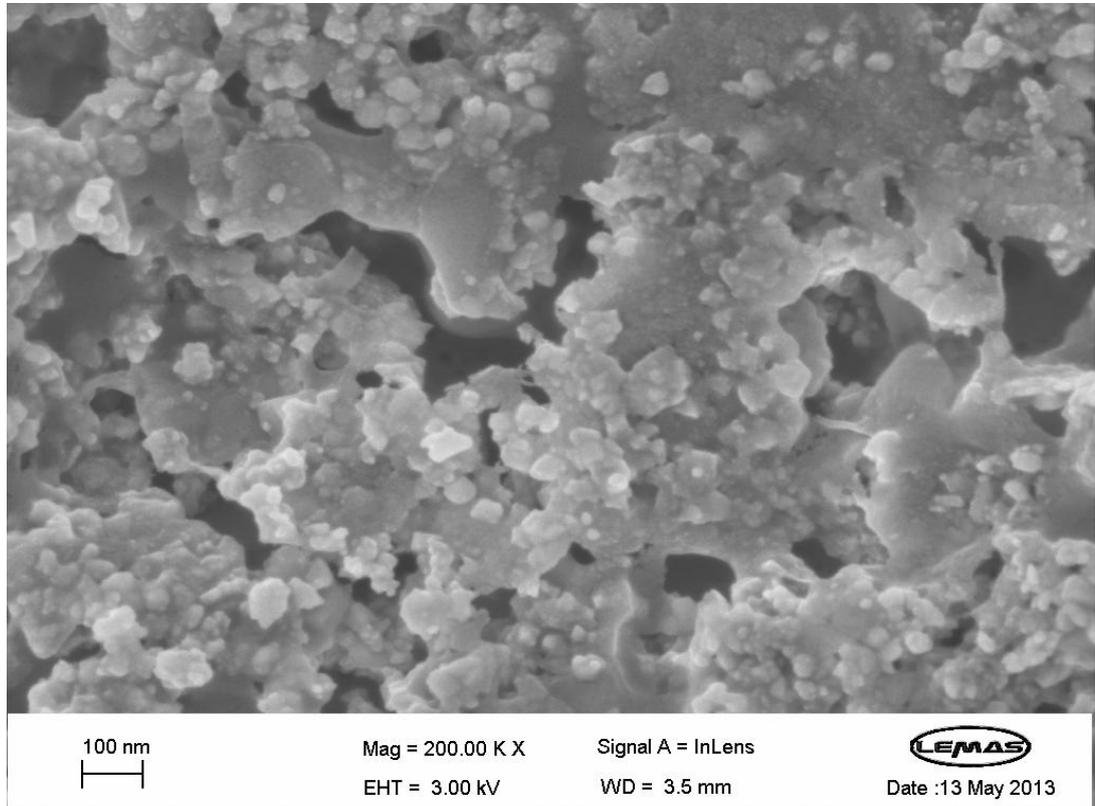
Figure 90: Scaled up version the bottom picture in Figure 102 (red circle showed the area focused on).

The heterogeneous distribution of nano-particles in these SEM images (Fig. 90) might point toward the need for better dispersion as any aggregation will affect the specific heat capacity enhancement by reducing the total volume area of the salt nano-layers.

The dispersion methodology has been showed to alter the amount of enhancement obtained from the addition of nano-particles [124]. This could imply that surface chemistry might play an important role in the aggregation process and also in its interaction with the surrounding liquid. The calculation of Cp needs to take into account these types of interaction in order to successfully model the enhancement obtained from the addition nano-particles as current models fail to do so [119].

6.9   Rheological Analysis of 0.1 wt% CuO additives
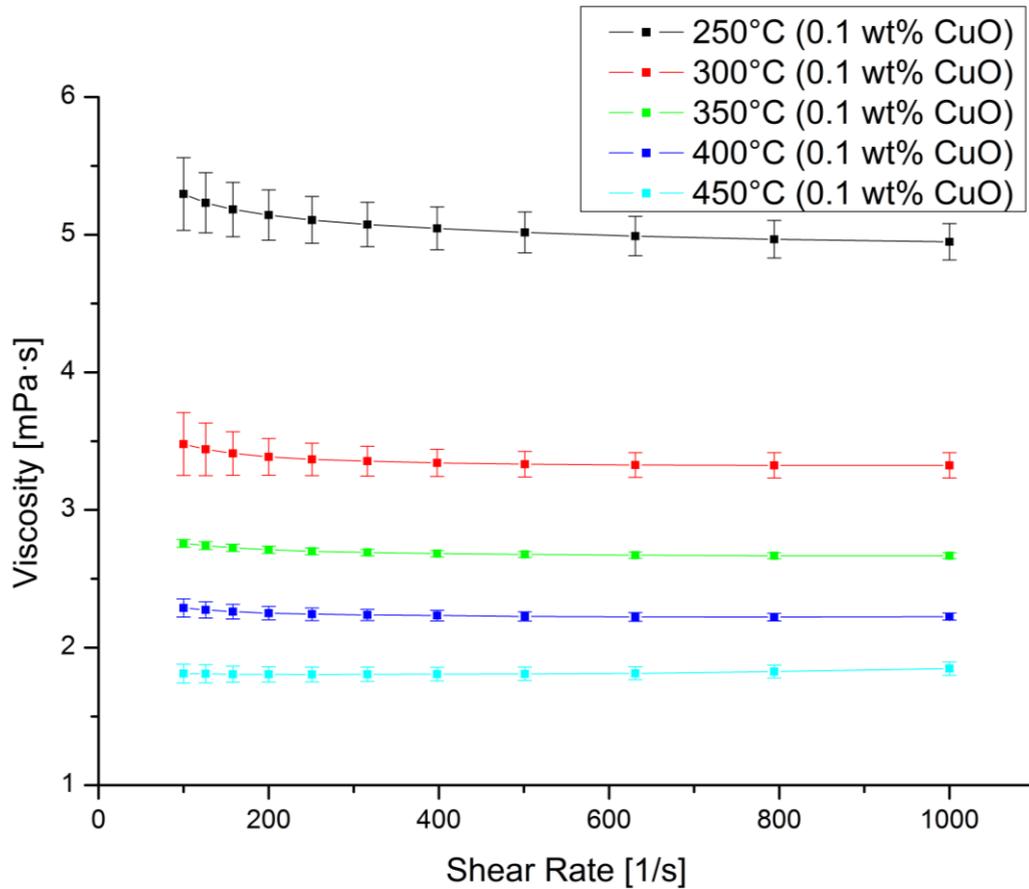
Figure 91: Viscosity profile of binary nitrate mixture (60 wt. % NaNO$_3$ & 40 wt. % KNO$_3$) containing 0.1 wt% Copper Oxide against increasing shear rate.

The use of 0.1 wt% Copper oxide nano-particles in the binary salt displayed a Newtonian fluid behaviour above 100 s^{-1} as it was expected. The mean viscosity increased with temperature when the additive was present which agreed with data obtained Jo et al. 2012 who tested the viscosity of a binary nitrate composition with and without 1.0 wt% SiO$_2$ and found an increase at 300°C and 400°C of 63% and 79% respectively [125].
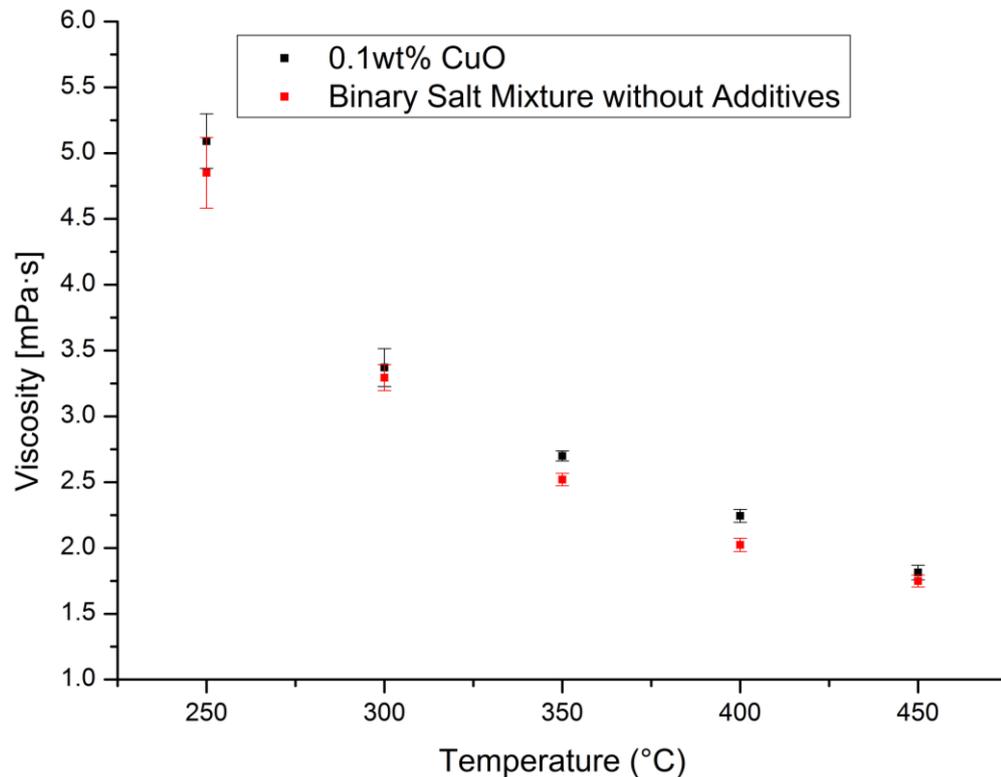
Figure 92: Average viscosity taken from 100 - 1000 s^{-1} of binary nitrate mixture (60 wt. % NaNO$_3$ & 40 wt. % KNO$_3$) containing 0.1 wt% Copper Oxide against temperature.

Unlike Jo et al. 2012, no shear thinning effect was observed with increased temperature when the additive was present although increasing the concentration of nano-particles might lead to this effect [125].

The effect of nano-particles addition on the rheological behaviour of the fluids depends on factors such as: particle shape, size, loading, temperature, shear rate and base liquid. The presence of solid particles promote the formation of vortex structure near the surface of the particle and leads to the production of a rotational movement [126]. This will give rise to an expenditure of energy which cause a relaxation of the particle velocity thereby increasing its viscosity. The latter will also be affected by the shape (sphere, plate or rods) of the nano-particles with aspheric particle displaying

much higher viscosity than their spherical counterpart at the same concentration [127]. Furthermore the shear rate used to perform the tests will affect particle-particle interaction as the latter will grow weaker and brake down with rising shear rate leading to shear thinning. At constant shear, it is of general consensus among literatures that, as the particle concentration increases, the viscosity of the fluid rises [128]. The percentage enhancement of viscosity is still dependent on factors such as shape, size, temperature, base fluid and shear used.

In the experimental setup, the base fluid, molten salt, demonstrated a Newtonian behaviour between 100 s^{-1} and 1000 s^{-1}. At these rotational speed and with the low concentration of nano-particles present, it is not surprising to see a Newtonian behaviour as the fast rotational force applied on the fluid would lead to dispersion of nano-particles breaking the formation of aggregate if any were present to begin with. The use of a larger concentration of nano-particle (1.0 to 5.0 wt.%) and a low shear rate to begin with 1.0 s^{-1} might cause the formation of aggregate leading to a rise in viscosity slowly decreasing with increased shear force.
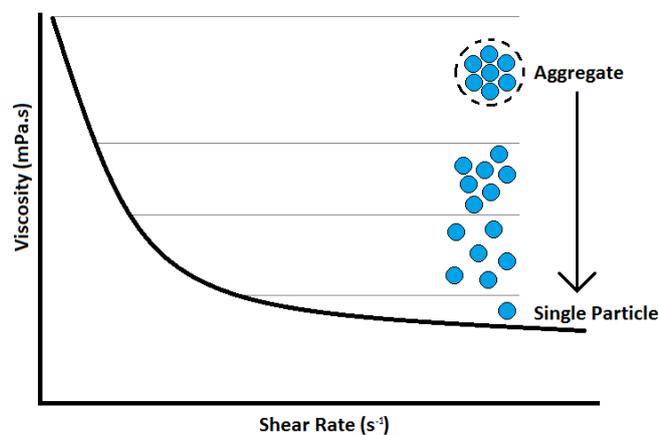
Figure 93: Effect of shear rate on viscosity [126, 127, 129]

These perturbations in fluid flow are considered by the Einstein's theory formulated in 1906, for spherical particles with low volume fraction. With many systems and experimental setup produced, different mathematical models have been created trying to fit the obtained data with theoretical values [128, 130].

6.10 Further Discussion & Summary

Understanding the effect of nano-particles in molten salt is important in the development of stable nano-fluid formulation capable of storing and transferring large quantities of thermal energy. Flowing through a circular piping system, the molten salt would display a turbulent behaviour. The latter would allow for a better more efficient transfer of heat within the system due to the production of 'eddies'. The type of heat transfer can be calculated through the Prandtl number (Pr).

Written as;

$$Pr = \mu C_p / k$$

where μ is the dynamic viscosity (N.s.m^{-2}), Cp is the specific heat capacity (J/[g*K]) and k is the thermal conductivity (W/[m*K]). This equation evaluate which mode of energy transfer is dominant. It follows that, Pr > 1 imply that the main mode of heat transfer is dictated by convection whilst Pr < 1 means that thermal conduction dominates. Using Dittus Boelter equation to model a simple turbulent flow inside circular pipe, the heat transfer coefficient can be derived from the following equation where:

$$Nu = 0.023 \ Re^{0.8} * Pr^{1/3}$$

$$hd/k = 0.023 \ (jd/\mu)^{0.8} * (\mu C_p/k)^{1/3}$$

h = Heat transfer coefficient (W/[m^2*K])

d = Diameter of pipe (m)

k = Thermal conductivity (W/[m*K])

j = Mass flux (kg/[s*m^{-2}])

μ = Viscosity ($[N*s]/m^2$)

Cp = Specific heat capacity (J/[g*K])

Rearranging in term of heat transfer coefficient:

$$h = 0.023 \, [\, j^{0.8} * Cp^{1/3} * k^{2/3} * \mu^{-0.47} * d^{-0.2} \,]$$

It can be seen from the above equation that enhancing the specific heat capacity and/or thermal conductivity would have a positive effect on the heat transfer coefficient. However the addition of nano-particle would lead to increase viscosity which would be damaging to the heat transfer coefficient as would an increase in the diameter of the piping system.

Whilst much research is still needed to be done before this technology is implemented, the interaction between nano-particles and molten salt fluid cannot be denied and their effect on heat transfer coefficient is positive [131]. This should lead to a lower cost of electricity production in concentrated solar power plant allowing it to further compete against non-renewable energy sources.

This research has highlighted that repeated basic characterisation of binary nitrate salt mixture has not been carried out in the literature. Indeed basic specific heat capacity varies hugely which is probably due to the equipment and technique used as demonstrated in the preliminary results obtained in Chapter 3. The theory behind the improvement seen when utilizing nano-particles might be due to the formation of nano-layers as molten salt ions 'coat' their surface. The latter would also affect other thermal characteristic such as onset & point of melting/crystallisation as well as rheological measurements.

Chapter 7 Results & Discussion: Stability Rigs

This chapter looks at the effects of physical mixing on the thermal characteristics of the liquid salt when tested with additives and without additives to monitor how this affected the dispersion of 0.1 wt% Copper Oxide.

7.1 Static Rig with Binary Nitrate Salt – No Additives – Negative Control

Results obtained showed that there was a defined difference in Cp between the sample produced in the lab and the salt taken from the rig. The latter displayed higher values which could be caused by impurities found in the container. Indeed the molten salt is corrosive by nature and would start to attack the stainless steel. Whilst this may be a very slow process, it might affect the data gathered as the salts produced in the lab were not in contact with steel under liquid form.
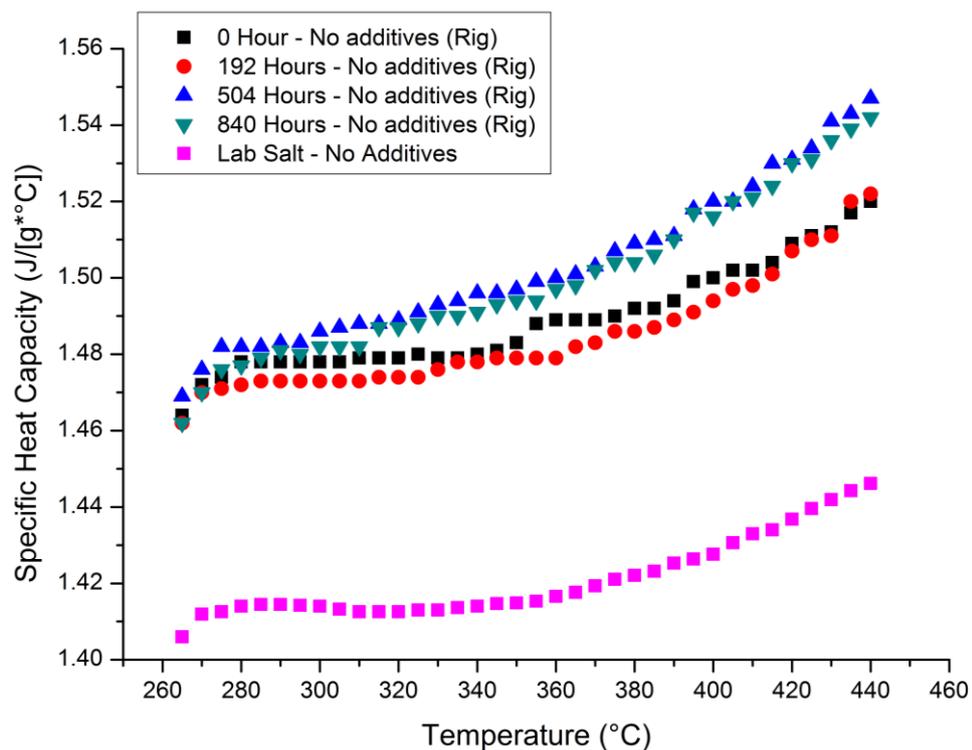
Figure 94: Difference in specific heat capacity between sample produce in the lab and directly tested on the DSC compared to sample obtained from the rig after different length of time (Standard Deviation <2.0%).

Evaluation of the melting point and enthalpy of fusion between the two revealed that both were substantially higher which would tend to confirm the

slight change in the composition of the salt. Whilst the actual melting point and enthalpy of fusion remained the same over 800 hours, the reaction of the binary salt mixture with the stainless steel container might have led to this rise.
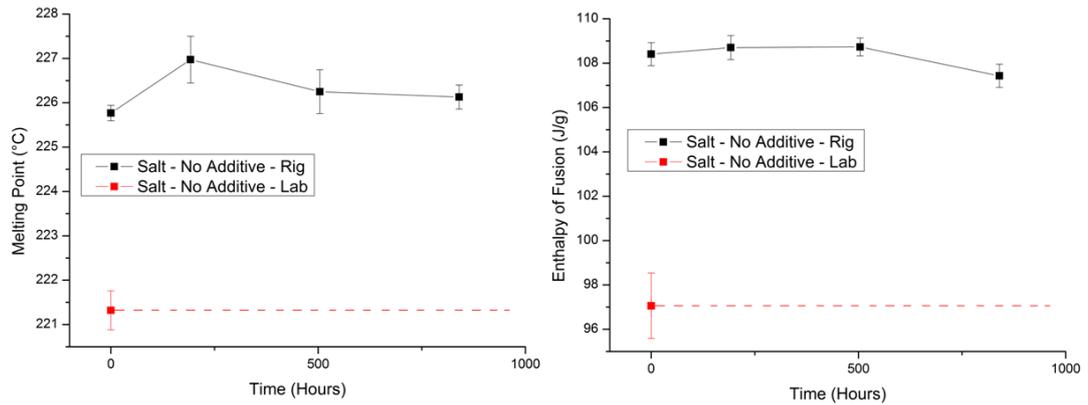
Figure 95: Difference in melting point and enthalpy of fusion between sample taken from the rig and salt produced in the lab for binary nitrate mixture containing no additives.

Figure 96: Photographs of samples removed from the rigs at different times.

The molten nitrate salt would have started to corrode the 316 stainless steel container as soon as the liquid phase was reached. Although the temperature was only 300°C, the equilibrium would favour the production of nitride and oxygen. The latter could have reacted with the 316 stainless steel metallic surface (Fe-16Cr-10Ni-2Mo) forming oxide which would push this further to the nitrite production although this would be a slow process [132]. It is important to mention that the 0 hour signified the start of the measurement but did not imply that the salt started to melt at that time. The salt had spent at least 24 hours in molten state prior to starting the measurement to ensure that the rigs were functioning correctly. Another simpler explanation could be a slight change in the ratio of sodium to potassium nitrate as kilograms of mixture were produced but this would seems unlikely as the quantities used were large and therefore easier to measure.

Visual inspection of the sample removed showed a white crystal structure, which was similar to all of them, although the photographs taken seem to display slight variations. This was due to the change in exposure as the pictures were taken and the presence or absence of flash.

7.2 Static Rig with Binary Nitrate salt – 0.1 wt% CuO – Positive Control

The addition of CuO led to a drop in specific heat capacity below that of the average measured for salt without additives. This was difficult to comprehend and explain. Melting point was similar whilst the enthalpy of fusion was slightly lower. Finally visual inspection revealed that CuO nano-particles would settle at the bottom of the tank if no dispersion method was provided. The rate at which this occurred was not directly determined but would need to be addressed if nano-particles were used in CSP application.
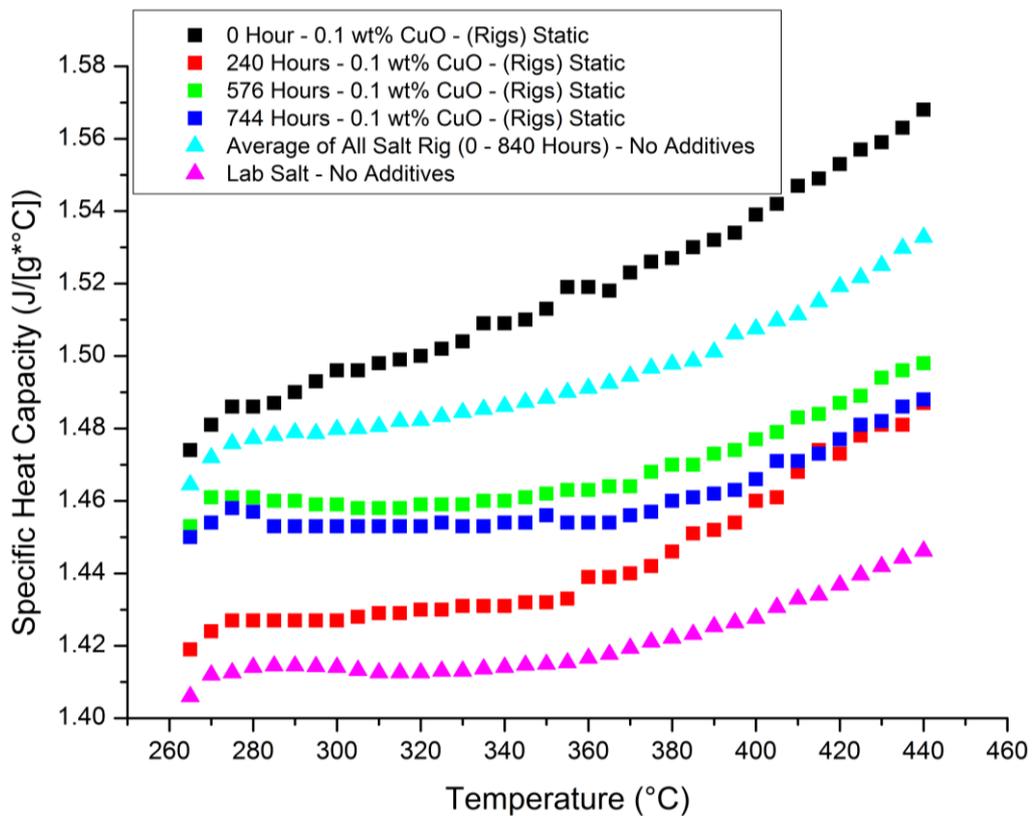
Figure 97: Variation of specific heat capacity of static binary nitrate salt mixture containing 0.1 wt% CuO nano-particles against averages of both static of salt taken from rigs between 0 – 840 hours and salt produced in the lab (Standard Deviation <2.0%).
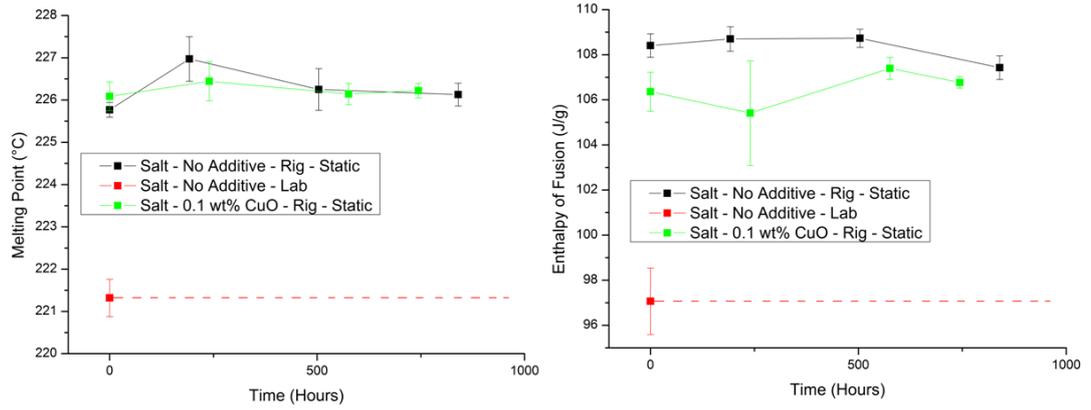
Figure 98: Melting point and enthalpy of fusion comparison between the presence and absence of CuO with salt taken from the rig and salt made in the lab.

Figure 99: Photographs of static samples with & without 0.1 wt% CuO removed from the rigs at different times compared to pure binary nitrate salt. Red circle showed accumulation of nano-particles at the tip of the sample.

7.3 Bubbling Rig with Binary Nitrate Salt – 0.1 wt% CuO

The results showed that heat capacity seemed to drop with time. The melting point and enthalpy of fusion did not vary with time and the latter were similar to the static salt mixture containing no additives.
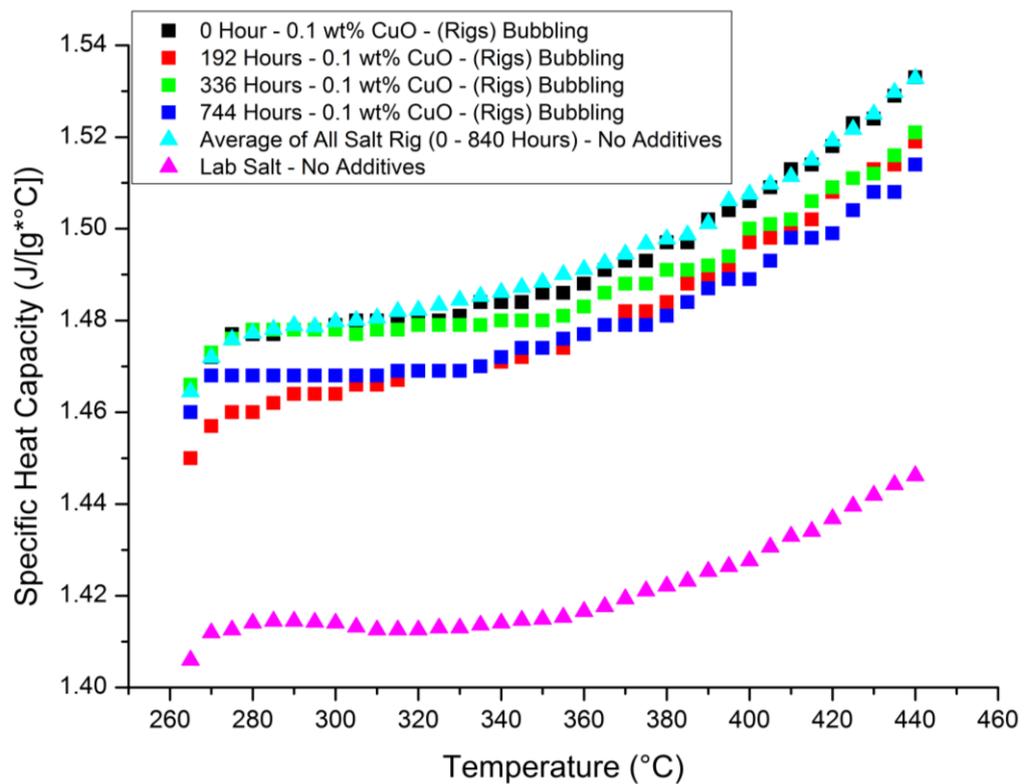
Figure 100: Variation of specific heat capacity of static binary nitrate salt mixture containing 0.1 wt% CuO nano-particles against averages of both static of salt taken from rigs between 0 – 840 hours and salt produced in the lab (Standard Deviation <2.0%).

Visual examination of the sample showed that the compressed air was stopped on two occasions which was highlighted by the sample colour turning white instead of grey due to the settling of nano-particles at the bottom of the tank (Red circles, Fig. 102). The amount of bubbles used as well as the way in which the system used to disperse the nano-particles would affect the efficiency of dispersion.
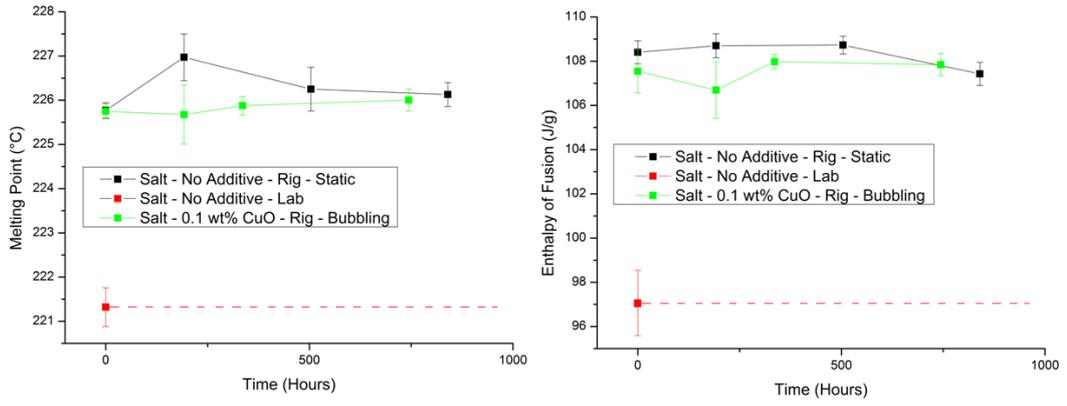
Figure 101: Melting point and enthalpy of fusion comparison between the presence and absence of CuO with salt taken from the rig and salt made in the lab.

Figure 102: Photographs comparing the static sample without additives (Left, 0 hours) to the bubbling rig samples (Right, 0 – 744 hours) removed at different time.

7.4 Dynamic Rig with Binary Nitrate Salt – 0.1 wt% CuO

This type of dispersion had a negative impact on the specific heat capacity, which was far more pronounced than bubbling. The latter increased with time, coming close to the value obtained for specific heat capacity of pure salt produced in the lab.
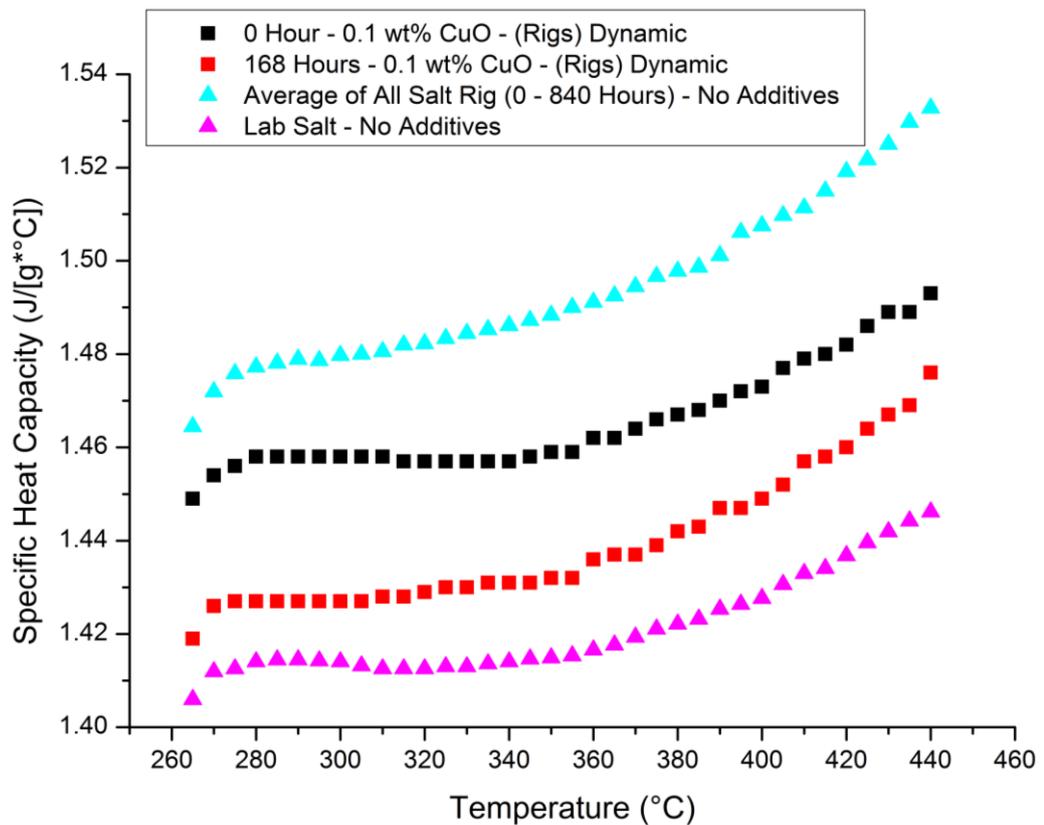
Figure 103: Variation of specific heat capacity of static binary nitrate salt mixture containing 0.1 wt% CuO nano-particles against averages of both static of salt taken from rigs between 0 – 840 hours and salt produced in the lab (Standard Deviation <2.0%).

Only two samples were collected due to a failure of the piston preventing the collection of further samples. No real differences were measured in both the enthalpy of fusion and the melting point.
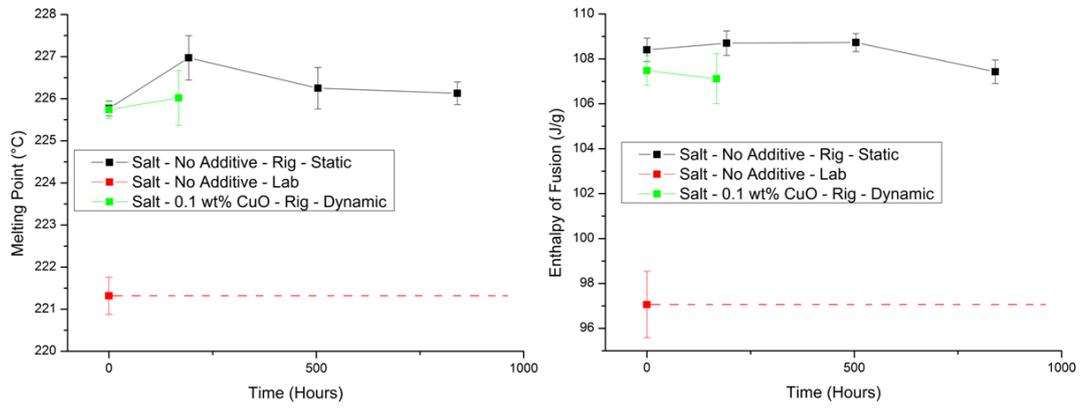
Figure 104: Melting point and enthalpy of fusion comparison between the presence and absence of CuO with salt taken from the rig and salt made in the lab.

Figure 105: Photographs comparing the static sample without additives (Left, 0 hours) to the dynamic rig samples (Right, 0 & 168 hours) removed at different time.

7.5 Stirring Rig (400 rpm) with Binary Nitrate Salt – 0.1 wt% CuO

The mean specific heat capacity displayed a rise after 576 & 744 Hours when stirring at 400 rpm whilst below 240 hours; the specific heat capacity was similar to that of the average value of rig salt containing no additive.
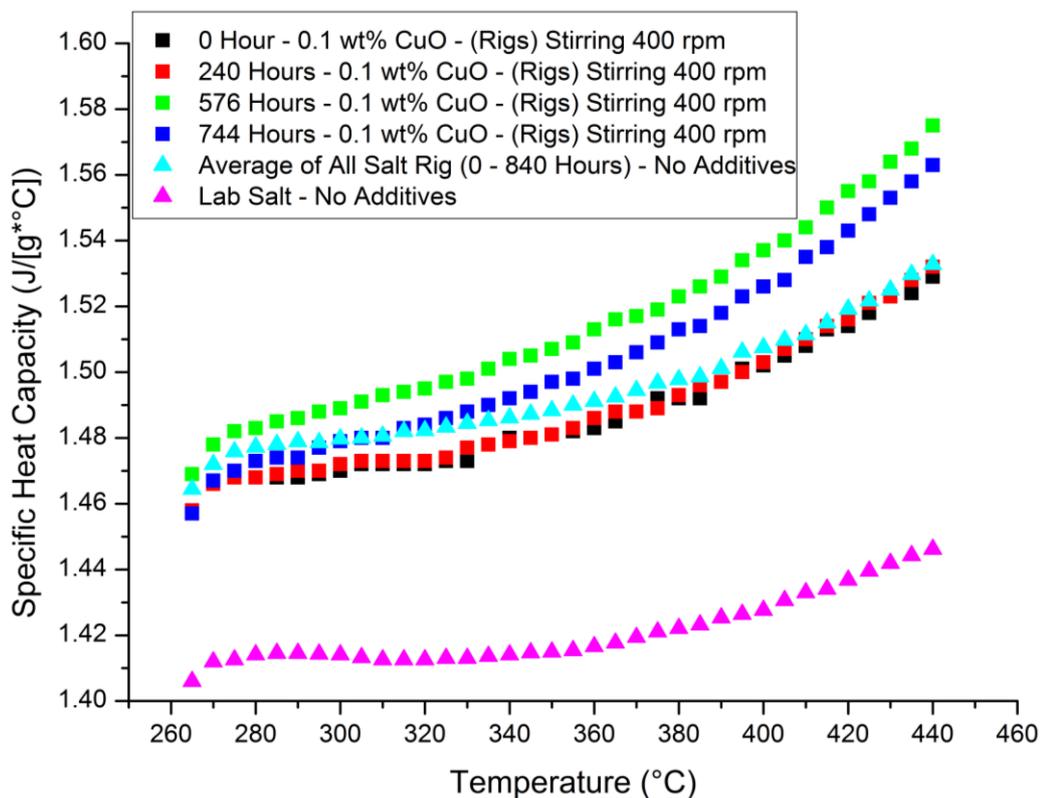
Figure 106: Variation of specific heat capacity of static binary nitrate salt mixture containing 0.1 wt% CuO nano-particles against averages of both static of salt taken from rigs between 0 – 840 hours and salt produced in the lab (Standard Deviation <2.0%).

No differences were showed in the melting point; however the enthalpy of fusion was significantly lowered consistently through the duration of the tests. Finally visual analysis showed that the use of stirring kept the colouration of the salt similar which could be an indication of dispersion.
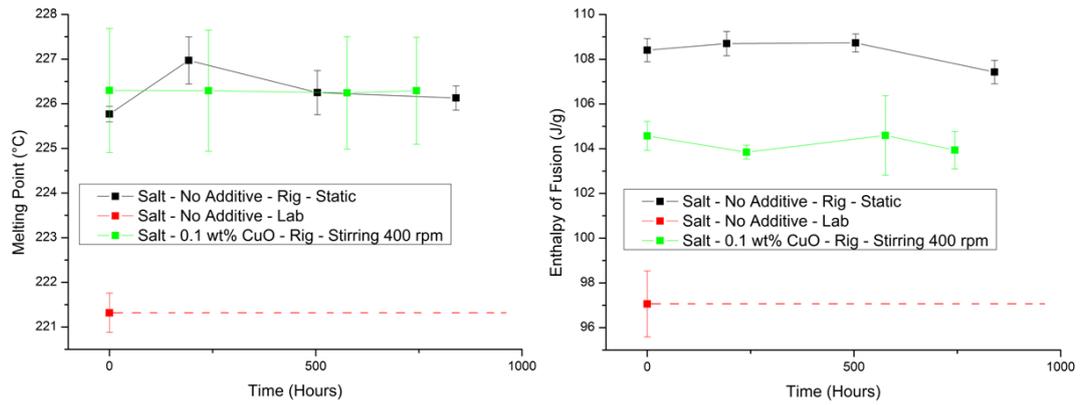
Figure 107: Melting point and enthalpy of fusion comparison between the presence and absence of CuO with salt taken from the rig and salt made in the lab.

Figure 108: Photographs comparing the static sample without additives (Left, 0 hours) to the stirring (400 rpm) rig samples (Right, 0 – 744 hours) removed at different time.

7.6 Further Discussion and Summary

The addition of nano-particles to binary mixture of nitrate salt revealed that settling was a challenge to overcome in order to profit from their beneficial effect particularly on the specific heat capacity. Providing that this enhancement was due to the production of these nano-layers, variables such as size distribution of the nano-particles, percentage ratio of additives, surface chemistry of nano-particle & shape, type of container used, salt ratio & type, temperature, viscosity and probably many others factors will affect their behaviour. As it was demonstrated previously, the optimum ratio is different from one type of nano-particle to the next. The use of physical dispersion provided a mean to re-suspend the copper oxide nano-particles. However the type of dispersion used altered the specific heat capacity measurement such that both bubbling and dynamic impacted negatively on the mixture whilst only stirring provided an increase in the mean Cp values which differed greatly from results observed in the lab. The type of turbulence used might have reduced/disturbed the production of these nano-layers around the copper oxide nano-particles leading to a decrease in Cp. Alternatively the method of dispersion which was different as large scale production was needed, might have altered the surface chemistry of the nano-particle significantly such that the results obtained were altered.

The general trend in the melting point and enthalpy of fusion seemed to be a slight decrease in the value tested compared to the static pure salt value. The only exception was for the stirring enthalpy of fusion which was altered significantly whilst the melting point was similar although the standard deviation was greater.

Chapter 8 Conclusion and Future Work

The aim of this thesis was to try to understand how the thermal behaviour of binary nitrate mixture of salt was altered by the addition of nano-particles.

The specific objectives were as followed:

I. Define the thermal characteristics of potassium and sodium nitrate as well as the eutectic nitrate mixture of the latter two (60 wt% $NaNO_3$ + 40 wt% KNO_3)

II. Screen how the addition of nano-particles affect the specific heat capacity of the salt mixture

III. Evaluate whether the methodology of dispersion affect the value obtained for specific heat capacity and how melting, onset and crystallisation react to such change

IV. Characterise the rheology of the selected additive

V. Analyse the behaviour of the selected nano-particle (0.1 wt% CuO) on salt before and after melting has occurred using SEM

VI. Test whether physical dispersion affects the thermal properties of the salt over time.

(I) Sodium and potassium nitrate displayed melting point of 308.01°C and 336.03°C respectively with enthalpy of fusion of 172.84 J/g for $NaNO_3$ and 95.55 J/g for KNO_3. The specific heat capacity was found to be 1.30 J/[g*°C] for KNO_3 at 350°C whilst $NaNO_3$ was 1.50 J/[g*°C]. The combination of these two salts (60 wt% $NaNO_3$ & 40 wt% KNO_3) led to the production of a

eutectic mixture which had a melting point of 221°C as expected with enthalpy of fusion of 97.06 J/g. The calculation of Cp closely matched the actual measured values with values of 1.415 J/[g*°C] against the 1.42 J/[g*°C] calculated. This eutectic salt was showed to be stable up to 550°C and rheological measurement revealed a Newtonian behaviour above shear rate of 100 s^{-1}. The viscosity dropped with increasing temperature from 4.75 mPa.s at 250°C to 1.75 mPa.s at 450°C which seemed to follow the literature value obtained.

(II) The addition of nano-particles to molten salt had an overall positive effect on the specific heat capacity raising the mean value of the salt. Consequently the onset melting temperature dropped and the range of the melting increased as well as the enthalpy of fusion. The onset and peak of crystallisation were also both affect by the nano-particle addition causing an increase in both values.

(III) The evaluation of the methodology revealed no difference in the heat capacity values between the techniques used to prepare the samples. This was important to know as this technique could be scaled up to industrial level.

(IV) The rheology of the salt with nano-particle additive showed a slight increase in viscosity as the nano-particles disturbed the flow lines.

(V) SEM images of 0.1 wt% CuO revealed that the interaction between the salt surface before and after melting were present. It also showed

heterogeneous distribution of nano-particles which could have a major impact on the specific heat capacity of salt due to a reduction of the nano-layers total volume through aggregation. Furthermore it revealed the importance attached to nano-particles production, as the surface chemistry as well as shape of the nano-particles is going to be affected by the production process. This will also impact dispersion.

(VI) The behaviour of salt in the rigs was different from the tests carried out in the DSC. The melting, crystallisation and enthalpy of change varied between the two when only pure salt was used. A number of reasons were enumerated for this change, but the exact cause of the change was not defined.

The tests also revealed the settling challenge encountered when using nano-particles and showed that the type of physical dispersion used to re-suspend the nano-particles could affect the specific heat capacity either negatively or positively. The enhancement seen during the screening test (10% increase using 0.1 wt% CuO) was not repeated in the rig tests.

The research carried out led to more question been raised than answered and highlighted how the need for further research in the following area:

- Effect of nano-particles production process and salt mixing method on the specific heat capacity of salt
- Investigation on the stability of nano-particles with varying temperature
- Testing how physical dispersion of different concentration of nano-particles affects the specific heat capacity

- Modelling of ionic interaction of molten salt ions with nano-particles

Industrial application of salt in concentrated solar power plant is still hindered by the lack of knowledge and fundamental understanding of the behaviour of nano-particles in liquid molten salt. Tackling each of the above issues might provide a way toward the application of this technology which would reduce the cost of electricity production allowing it to compete with non-renewable technology in the production of electricity.

List of References

1.   Manzano-Agugliaro, F., et al., *Scientific production of renewable energies worldwide: An overview.* Renewable & Sustainable Energy Reviews, 2013. **18**: p. 134-143.

2.   Kadiri, M., et al., *A review of the potential water quality impacts of tidal renewable energy systems.* Renewable & Sustainable Energy Reviews, 2012. **16**(1): p. 329-341.

3.   IEA, *International Energy Outlook 2011*. 2011, International Energy Agency: http://www.eia.gov/forecasts/ieo/pdf/0484(2011).pdf.

4.   IEA. *Key World Energy STATISTICS*. 2012; Available from: http://www.iea.org/publications/freepublications/publication/kwes.pdf.

5.   Dincer, I. and M.A. Rosen, *Energy, environment and sustainable development.* Applied Energy, 1999. **64**(1-4): p. 427-440.

6.   Thirugnanasambandam, M., S. Iniyan, and R. Goic, *A review of solar thermal technologies.* Renewable & Sustainable Energy Reviews, 2010. **14**(1): p. 312-322.

7.   Kalogirou, S.A., *Solar thermal collectors and applications.* Progress in Energy and Combustion Science, 2004. **30**(3): p. 231-295.

8.   IRENA, *Concentrating Solar Power*. 2012, International Renewable Energy Agency (IRENA).

9.   IRENA, *Concentrated Solar Power*. 2013, International Renewable Energy Agency (IRENA).

10.   Dell, R.M. and D.A.J. Rand, *Energy storage - a key technology for global energy sustainability.* Journal of Power Sources, 2001. **100**(1-2): p. 2-17.

11.   IEA, *Solar Energy Perspectives*. 2011, International Energy Agency.

12.   Kenisarin, M.M., *High-temperature phase change materials for thermal energy storage.* Renewable & Sustainable Energy Reviews, 2010. **14**(3): p. 955-970.

13.   Shin, D. and D. Banerjee, *Effects of silica nanoparticles on enhancing the specific heat capacity of carbonate salt eutectic (work in progress).* INTERNATIONAL JOURNAL OF STRUCTURAL CHANGES IN SOLIDS, 2010. **2**(2): p. 25-31.

14.   Tiznobaik, H. and D. Shin, *Enhanced specific heat capacity of high-temperature molten salt-based nanofluids.* International Journal of Heat and Mass Transfer, 2013. **57**(2): p. 542-548.

15.   Dudda, B. and D. Shin, *Effect of nanoparticle dispersion on specific heat capacity of a binary nitrate salt eutectic for concentrated solar power applications.* International Journal of Thermal Sciences, 2013. **69**(0): p. 37-42.

16.   Lu, M.C. and C.H. Huang, *Specific heat capacity of molten salt-based alumina nanofluid.* Nanoscale Research Letters, 2013. **8**.

17.   DOE, U.S., *SunShot Vision Study : February 2012*. 2012, U.S. DEPARTMENT OF ENERGY.

18. NEEDS, *Final report on technical data, costs, and life cycle inventories of solar thermal power plants*, in *NEEDS*. 2008, New Energy Externalities Developments for Sustainability (NEEDS).

19. Price, H., et al., *Advances in parabolic trough solar power technology.* Journal of Solar Energy Engineering-Transactions of the Asme, 2002. **124**(2): p. 109-125.

20. Yaghoubi, M., F. Ahmadi, and M. Bandehee, *Analysis of Heat Losses of Absorber Tubes of Parabolic through Collector of Shiraz (Iran) Solar Power Plant.* Journal of Clean Energy Technologies, 2013. **1**(1): p. 5.

21. Mills, D.R. and G.L. Morrison, *Compact linear Fresnel reflector solar thermal powerplants.* Solar Energy, 2000. **68**(3): p. 263-283.

22. Mills, D.R., G.L. Morrison, and P. Le Liever. *MULTI-TOWER LINE FOCUS FRESNEL ARRAYS.* in *International Solar Energy Conference.* 2003. Mauna Kea Resort, Hawaii Island, Hawaii, USA: ASME.

23. Mills, D., *Advances in solar thermal electricity technology.* Solar Energy, 2004. **76**(1-3): p. 19-31.

24. Lovegrove, K., et al., *Concentrating Solar Power in India [Report commissioned by the Australian Government and prepared by IT Power].* 2011, Australian Government: Department of Climate Change and energy Efficiency

25. Mancini, T., et al., *Dish-Stirling systems: An overview of development and status.* Journal of Solar Energy Engineering-Transactions of the Asme, 2003. **125**(2): p. 135-151.

26. Kongtragool, B. and S. Wongwises, *A review of solar-powered Stirling engines and low temperature differential Stirling engines.* Renewable & Sustainable Energy Reviews, 2003. **7**(2): p. 131-154.

27. IEA, *Technology Roadmap: Concentrating Solar Power.* 2010, International Energy Agency.

28. Zhang, H.L., et al., *Concentrated solar power plants: Review and design methodology.* Renewable & Sustainable Energy Reviews, 2013. **22**: p. 466-481.

29. Pavlovic, T.M., et al., *A review of concentrating solar power plants in the world and their potential use in Serbia.* Renewable & Sustainable Energy Reviews, 2012. **16**(6): p. 3891-3902.

30. Schramek, P. and D.R. Mills, *Multi-tower solar array.* Solar Energy, 2003. **75**(3): p. 249-260.

31. Py, X., Y. Azoumah, and R. Olives, *Concentrated solar power: Current technologies, major innovative issues and applicability to West African countries.* Renewable & Sustainable Energy Reviews, 2013. **18**: p. 306-315.

32. Sengupta, M., et al., *INTRODUCING NREL'S BEST PRACTICES HANDBOOK FOR COLLECTION AND USE OF SOLAR RESOURCE DATA FOR CSP*, in *IV Conferencia Latino Americana de Energía Solar.* 2010: Cusco, Peru.

33. Powell, K.M. and T.F. Edgar, *Modeling and control of a solar thermal power plant with thermal energy storage.* Chemical Engineering Science, 2012. **71**: p. 138-145.

34. Medrano, M., et al., *State of the art on high-temperature thermal energy storage for power generation. Part 2-Case studies.* Renewable & Sustainable Energy Reviews, 2010. **14**(1): p. 56-72.

35. Steinmann, W.D. and M. Eck, *Buffer storage for direct steam generation.* Solar Energy, 2006. **80**(10): p. 1277-1282.

36. Pacheco, J.E., S.K. Showalter, and W.J. Kolb, *Development of a molten-salt thermocline thermal storage system for parabolic trough plants.* Journal of Solar Energy Engineering-Transactions of the Asme, 2002. **124**(2): p. 153-159.

37. Fang, M. and G.M. Chen, *Effects of different multiple PCMs on the performance of a latent thermal energy storage system.* Applied Thermal Engineering, 2007. **27**(5-6): p. 994-1000.

38. Bauer, T., D. Laing, and R. Tamme, *Overview of PCMs for concentrated solar power in the temperature range 200 to 350 °C.* Advances in Science and Technology, 2010. **74**: p. 272-277.

39. Laing, D., et al., *Solid media thermal storage for parabolic trough power plants.* Solar Energy, 2006. **80**(10): p. 1283-1289.

40. Laing, D., et al., *High-Temperature Solid-Media Thermal Energy Storage for Solar Thermal Power Plants.* Proceedings of the Ieee, 2012. **100**(2): p. 516-524.

41. Laing, D., et al., *Test Results of Concrete Thermal Energy Storage for Parabolic Trough Power Plants.* Journal of Solar Energy Engineering-Transactions of the Asme, 2009. **131**(4).

42. Kuravi, S., et al., *Thermal energy storage technologies and systems for concentrating solar power plants.* Progress in Energy and Combustion Science, 2013. **39**(4): p. 285-319.

43. Levy, M., et al., *SOLAR-ENERGY STORAGE VIA A CLOSED-LOOP CHEMICAL HEAT PIPE.* Solar Energy, 1993. **50**(2): p. 179-189.

44. Lovegrove, K., et al., *Developing ammonia based thermochemical energy storage for dish power plants.* Solar Energy, 2004. **76**(1-3): p. 331-337.

45. Kanamori, M., H. Matsuda, and M. Hasatani, *Heat storing/releasing characteristics of the chemical heat storing unit of electricity using Ca(OH)(2)/CaO reaction.* Kagaku Kogaku Ronbunshu, 1996. **22**(2): p. 257-263.

46. Schaube, F., A. Worner, and R. Tamme, *High Temperature Thermochemical Heat Storage for Concentrated Solar Power Using Gas-Solid Reactions.* Journal of Solar Energy Engineering-Transactions of the Asme, 2011. **133**(3).

47. Abhat, A., *LOW-TEMPERATURE LATENT-HEAT THERMAL-ENERGY STORAGE - HEAT-STORAGE MATERIALS.* Solar Energy, 1983. **30**(4): p. 313-332.

48. Farid, M.M., et al., *A review on phase change energy storage: materials and applications.* Energy Conversion and Management, 2004. **45**(9-10): p. 1597-1615.

49. Shiina, Y. and T. Inagaki, *Study on the efficiency of effective thermal conductivities on melting characteristics of latent heat storage capsules.* International Journal of Heat and Mass Transfer, 2005. **48**(2): p. 373-383.

50. Nomura, T., N. Okinaka, and T. Akiyama, *Technology of Latent Heat Storage for High Temperature Application: A Review.* Isij International, 2010. **50**(9): p. 1229-1239.

51. Zhang, X.X., et al., *Expansion space and thermal stability of microencapsulated n-octadecane.* Journal of Applied Polymer Science, 2005. **97**(1): p. 390-396.

52. Fang, Y.T., et al., *Preparation and characterization of novel nanoencapsulated phase change materials.* Energy Conversion and Management, 2008. **49**(12): p. 3704-3707.

53. Fang, Y.T., et al., *Preparation of nanoencapsulated phase change material as latent functionally thermal fluid.* Journal of Physics D-Applied Physics, 2009. **42**(3).

54. Tamme, R., et al., *Latent heat storage above 120 degrees C for applications in the industrial process heat sector and solar power generation.* International Journal of Energy Research, 2008. **32**(3): p. 264-271.

55. Wu, J.F., et al., *Molten salts/ceramic-foam matrix composites by melt infiltration method as energy storage material.* Journal of Wuhan University of Technology-Materials Science Edition, 2009. **24**(4): p. 651-653.

56. Kodama, T., et al., *Ni/ceramic/molten-salt composite catalyst with high-temperature thermal storage for use in solar reforming processes.* Energy, 2004. **29**(5-6): p. 895-903.

57. Kodama, T., et al., *Molten-Salt Tubular Absorber/Reformer (MoSTAR) Project: The Thermal Storage Media of Na2CO3-MgO Composite Materials.* Journal of Solar Energy Engineering-Transactions of the Asme, 2009. **131**(4).

58. Mondieig, D., et al., *Protection of temperature sensitive biomedical products using molecular alloys as phase change material.* Transfusion and Apheresis Science, 2003. **28**(2): p. 143-148.

59. Dincer, I. and S. Dost, *A perspective on thermal energy storage systems for solar energy applications.* International Journal of Energy Research, 1996. **20**(6): p. 547-557.

60. Hasnain, S.M., *Review on sustainable thermal energy storage technologies, part I: Heat storage materials and techniques.* Energy Conversion and Management, 1998. **39**(11): p. 1127-1138.

61. Dincer, I., S. Dost, and X.G. Li, *Performance analyses of sensible heat storage systems for thermal applications.* International Journal of Energy Research, 1997. **21**(12): p. 1157-1171.

62. Choi, S.U.S. and J.A. Eastman, *Enhancing Thermal Conductivity of Fluids with Nano-particles*, in *International Mechanical Engineering Congress & Exposition*. 1995: San Francisco, USA.

63. Lee, S., et al., *Measuring thermal conductivity of fluids containing oxide nanoparticles.* Journal of Heat Transfer-Transactions of the Asme, 1999. **121**(2): p. 280-289.

64. Das, S.K., et al., *Temperature dependence of thermal conductivity enhancement for nanofluids.* Journal of Heat Transfer-Transactions of the Asme, 2003. **125**(4): p. 567-574.

65. Patel, H.E., et al., *Thermal conductivities of naked and monolayer protected metal nanoparticle based nanofluids: Manifestation of*

anomalous enhancement and chemical effects. Applied Physics Letters, 2003. **83**(14): p. 2931-2933.

66. Wen, D.S. and Y.L. Ding, *Experimental investigation into convective heat transfer of nanofluids at the entrance region under laminar flow conditions.* International Journal of Heat and Mass Transfer, 2004. **47**(24): p. 5181-5188.

67. Wen, D.S. and Y.L. Ding, *Formulation of nanofluids for natural convective heat transfer applications.* International Journal of Heat and Fluid Flow, 2005. **26**(6): p. 855-864.

68. Xie, H.Q., et al., *Dependence of the thermal conductivity of nanoparticle-fluid mixture on the base fluid.* Journal of Materials Science Letters, 2002. **21**(19): p. 1469-1471.

69. Zhang, X., H. Gu, and M. Fujii, *Effective thermal conductivity and thermal diffusivity of nanofluids containing spherical and cylindrical nanoparticles.* Experimental Thermal and Fluid Science, 2007. **31**(6): p. 593-599.

70. Eastman, J.A., et al., *Anomalously increased effective thermal conductivities of ethylene glycol-based nanofluids containing copper nanoparticles.* Applied Physics Letters, 2001. **78**(6): p. 718-720.

71. He, Y.R., et al., *Heat transfer and flow behaviour of aqueous suspensions of TiO2 nanoparticles (nanofluids) flowing upward through a vertical pipe.* International Journal of Heat and Mass Transfer, 2007. **50**(11-12): p. 2272-2281.

72. Ding, Y.L., et al., *Heat transfer of aqueous suspensions of carbon nanotubes (CNT nanofluids).* International Journal of Heat and Mass Transfer, 2006. **49**(1-2): p. 240-250.

73. Ding, Y.L., et al., *Heat Transfer Intensification Using Nanofluids.* Kona-Powder and Particle, 2007. **25**: p. 23-38.

74. Xie, H.Q., et al., *Thermal conductivity enhancement of suspensions containing nanosized alumina particles.* Journal of Applied Physics, 2002. **91**(7): p. 4568-4572.

75. Keblinski, P., R. Prasher, and J. Eapen, *Thermal conductance of nanofluids: is the controversy over?* Journal of Nanoparticle Research, 2008. **10**(7): p. 1089-1097.

76. Buongiorno, J., et al., *A benchmark study on the thermal conductivity of nanofluids.* Journal of Applied Physics, 2009. **106**(9).

77. Trisaksri, V. and S. Wongwises, *Critical review of heat transfer characteristics of nanofluids.* Renewable & Sustainable Energy Reviews, 2007. **11**(3): p. 512-523.

78. Yu, W. and H. Xie, *A Review on Nanofluids: Preparation, Stability Mechanisms, and Applications.* Journal of Nanomaterials, 2012.

79. Yang, X. and Z.-h. Liu, *A Kind of Nanofluid Consisting of Surface-Functionalized Nanoparticles.* Nanoscale Research Letters, 2010. **5**(8): p. 1324-1328.

80. Prasher, R., P.E. Phelan, and P. Bhattacharya, *Effect of aggregation kinetics on the thermal conductivity of nanoscale colloidal solutions (nanofluid).* Nano Letters, 2006. **6**(7): p. 1529-1534.

81. Lee, D., J.W. Kim, and B.G. Kim, *A new parameter to control heat transport in nanofluids: Surface charge state of the particle in suspension.* Journal of Physical Chemistry B, 2006. **110**(9): p. 4323-4328.

82. Das, S.K., S.U.S. Choi, and H.E. Patel, *Heat transfer in Nanofluids - A review.* Heat Transfer Engineering, 2006. **27**(10): p. 3-19.

83. Xuan, Y.M. and Q. Li, *Heat transfer enhancement of nanofluids.* International Journal of Heat and Fluid Flow, 2000. **21**(1): p. 58-64.

84. Bolmatov, D., V.V. Brazhkin, and K. Trachenko, *The phonon theory of liquid thermodynamics.* Sci. Rep., 2012. **2**.

85. Zhou, S.-Q. and R. Ni, *Measurement of the specific heat capacity of water-based Al(2)O(3) nanofluid.* Applied Physics Letters, 2008. **92**(9).

86. Pantzali, M.N., et al., *Effect of nanofluids on the performance of a miniature plate heat exchanger with modulated surface.* International Journal of Heat and Fluid Flow, 2009. **30**(4): p. 691-699.

87. Pak, B.C. and Y.I. Cho, *Hydrodynamic and heat transfer study of dispersed fluids with submicron metallic oxide particles.* Experimental Heat Transfer, 1998. **11**(2): p. 151-170.

88. Saeedinia, M., M.A. Akhavan-Behabadi, and P. Razi, *Thermal and rheological characteristics of CuO-Base oil nanofluid flow inside a circular tube.* International Communications in Heat and Mass Transfer, 2012. **39**(1): p. 152-159.

89. Nelson, C., I., *CHARACTERIZATION OF THERMO-PHYSICAL PROPERTIES AND FORCED CONVECTIVE HEAT TRANSFER OF POLY-ALPHA-OLEFIN (PAO) NANOFLUIDS.* 2007, Texas A&M University: Texas, USA. p. 81.

90. Shin, D.H. and D. Banerjee, *Enhanced Specific Heat of Silica Nanofluid.* Journal of Heat Transfer-Transactions of the Asme, 2011. **133**(2).

91. Wang, L., et al., *Enhancement of molar heat capacity of nanostructured Al2O3.* Journal of Nanoparticle Research, 2001. **3**(5-6): p. 483-487.

92. Tan, Z.C., L. Wang, and Q. Shi, *Study of heat capacity enhancement in some nanostructured materials.* Pure and Applied Chemistry, 2009. **81**(10): p. 1871-1880.

93. Tiznobaik, H. and D. Shin, *Experimental validation of enhanced heat capacity of ionic liquid-based nanomaterial.* Applied Physics Letters, 2013. **102**(17).

94. Shin, D. and D. Banerjee, *Enhancement of specific heat capacity of high-temperature silica-nanofluids synthesized in alkali chloride salt eutectics for solar thermal-energy storage applications.* International Journal of Heat and Mass Transfer, 2011. **54**(5-6): p. 1064-1070.

95. Wang, B.X., L.P. Zhou, and X.F. Peng, *Surface and size effects on the specific heat capacity of nanoparticles.* International Journal of Thermophysics, 2006. **27**(1): p. 139-151.

96. Prasher, R., P. Bhattacharya, and P.E. Phelan, *Brownian-motion-based convective-conductive model for the effective thermal conductivity of nanofluids.* Journal of Heat Transfer-Transactions of the Asme, 2006. **128**(6): p. 588-595.

97. Xue, L., et al., *Effect of liquid layering at the liquid–solid interface on thermal transport.* International Journal of Heat and Mass Transfer, 2004. **47**(19–20): p. 4277-4284.

98. Oh, S.H., et al., *Ordered liquid aluminum at the interface with sapphire.* Science, 2005. **310**(5748): p. 661-663.

99. Rheotec. *Introduction to Rheology: Basics*. Available from: http://www.dongjins.com/service/file/Introduction%20to%20rheology.pdf.

100. Schramm, G. *A Practical Approach to Rheology and Rheometry*. 1994; Available from: http://www.asi-team.com/asi%20team/haake/haake%20data/A%20practical%20approach%20to%20rheology%20and%20rhometry.pdf.

101. Kestin, J., M. Sokolov, and W.A. Wakeham, *VISCOSITY OF LIQUID WATER IN RANGE -8-DEGREES-C TO 150-DEGREES-C.* Journal of Physical and Chemical Reference Data, 1978. **7**(3): p. 941-948.

102. Rheotek. *VISCOSITY OIL STANDARDS*. 2014; Available from: http://www.rheotek.com/assets/rheotek/sub_cat_docs/Viscosity%20Oil%20Standards.pdf.

103. Janz, G., *Molten Salts Data as Reference Standards for Density, Surface Tension, Viscosity and Electrical Conductance: KNO3 and NaCl.* Journal of Physical and Chemical Reference Data, 1980. **9**(4): p. 39.

104. Laing, D., et al., *Advanced High Temperature Latent Heat Storage system - Design and Test Results*, in *Effstock 2009*. 2009: Stockholm, Sweden.

105. Bauer, T., et al., *SODIUM NITRATE FOR HIGH TEMPERATURE LATENT HEAT STORAGE*, in *Effstock 2009*. 2009: Stockholm, Sweden.

106. Takahashi, Y., R. Sakamoto, and M. Kamimoto, *HEAT-CAPACITIES AND LATENT HEATS OF LINO3, NANO3, AND KNO3.* International Journal of Thermophysics, 1988. **9**(6): p. 1081-1090.

107. Carling, R.W., *HEAT-CAPACITIES OF NANO3 AND KNO3 FROM 350-K TO 800-K.* Thermochimica Acta, 1983. **60**(3): p. 265-275.

108. Bauer, T., et al., *Material aspects of Solar Salt for sensible heat storage.* Applied Energy, 2013. **111**: p. 1114-1119.

109. Instrument, T. *Sapphire Specific Heat Capacity Literature Values*. 2014; Available from: http://www.tainstruments.co.jp/application/pdf/Thermal_Library/Applications_Notes/TN008.PDF.

110. Bauer, T. *PCM-Graphite Composites for High Temperature Thermal Energy Storage*. 2006; Available from: http://intraweb.stockton.edu/eyos/energy_studies/content/docs/FINAL_PRESENTATIONS/8B-1.pdf.

111. Betts, M., *THE EFFECTS OF NANOPARTICLE AUGMENTATION OF NITRATE THERMAL STORAGE MATERIALS FOR USE IN CONCENTRATING SOLAR POWER APPLICATIONS*, in *Mechanical Engineering*. 2011, Texas A&M University: Texas, USA. p. 91.

112. Steinmann, W.D., D. Laing, and R. Tamme, *Development of PCM Storage for Process Heat and Power Generation.* Journal of Solar Energy Engineering-Transactions of the Asme, 2009. **131**(4).

113. Kearney, D., et al., *Assessment of a molten salt heat transfer fluid in a parabolic trough solar field.* Journal of Solar Energy Engineering-Transactions of the Asme, 2003. **125**(2): p. 170-176.

114. Stern, H.K., *High Temperature Properties and Decomposition of Inorganic Salts*

Part3. Nitrates and Nitrites. Journal of Physical and Chemical Reference Data, 1972. **1**(3): p. 25.

115. Kramer, C.M. and C.J. Wilson, *The phase diagram of NaNO3—KNO3.* Thermochimica Acta, 1980. **42**(3): p. 253-264.

116. Siegel, N.P., et al., *THERMOPHYSICAL PROPERTY MEASUREMENT OF NITRATE SALT HEAT TRANSFER FLUIDS.* Proceedings of the Asme 5th International Conference on Energy Sustainability 2011, Pts a-C. 2012. 439-446.

117. Nissen, A.D., *Thermophysical Properties of the Equimolar Mixture NaNO3-KNO3 from 300 to 600°C.* Journal of Chemical and Engineering Data, 1982. **27**(3): p. 4.

118. Janz, J.G., et al., *Physical Properties Data Compilations Relevant to Energy Storage – II. Molten salts: Data on single and multi-component salt.* 1979, National Bureau of Standards.

119. Chieruzzi, M., et al., *Effect of nanoparticles on heat capacity of nanofluids based on molten salts as PCM for thermal energy storage.* Nanoscale Research Letters, 2013(8): p. 448.

120. Nash, L.K., *Elements of Statistical Thermodynamics, 2nd Edition.* 1972, USA: Dover Publications.

121. Singh, N., *COMPUTATIONAL ANALYSIS OF THERMO-FLUIDIC CHARACTERISTICS OF A CARBON NANO-FIN*, in *Mechanical Engineering.* 2010, Texas: Texas, USA. p. 114.

122. Keblinski, P., J.A. Eastman, and D.G. Cahill, *Nanofluids for thermal transport.* Materials Today, 2005. **8**(6): p. 36-44.

123. Ren, Y., H. Xie, and A. Cai, *Effective thermal conductivity of nanofluids containing spherical nanoparticles.* Journal of Physics D-Applied Physics, 2005. **38**(21): p. 3958-3961.

124. Jo, B. and D. Banerjee, *Enhanced specific heat capacity of molten salt-based nanomaterials: Effects of nanoparticle dispersion and solvent material.* Acta Materialia, 2014. **75**: p. 80-91.

125. Jo, B., et al., *ANOMALOUS RHEOLOGICAL BEHAVIOR OF COMPLEX FLUIDS (NANOFLUIDS).* Proceedings of the Asme International Mechanical Engineering Congress and Exposition, 2011, Vol 6, Pts a and B. 2012, New York: Amer Soc Mechanical Engineers. 223-228.

126. Chen, H., Y. Ding, and C. Tan, *Rheological behaviour of nanofluids.* New Journal of Physics, 2007. **9**.

127. Rao, Y., *Nanofluids: Stability, phase diagram, rheology and applications.* Particuology, 2010. **8**(6): p. 549-555.

128. Mishra, P.C., et al., *A brief review on viscosity of nanofluids.* International Nano Letters, 2014.

129. Rudyak, V., *Viscosity of Nanofluids—Why It Is Not Described by the Classical Theories.* Advances in Nanoparticles, 2013. **2**: p. 266-279.

130. Litchfield, D.W. and G. Baird, *THE RHEOLOGY OF HIGH ASPECT RATIO NANOPARTICLE FILLED LIQUIDS.* The British Society of Rheology, 2006: p. 1-60.

131. Andreu-Cabedo, P., et al., *Increment of specific heat capacity of solar salt with SiO2 nanoparticles.* Nanoscale research letters, 2014. **9**(1): p. 582-582.

132. Bradshaw, R.W. and H. Goods, S., *Effect of Temperature on Corrosion of Type 316 SS by Molten NaNO3 – KNO3*, in *ElectroChemistry Society (ECS).* 2000: Toronto, Canada.